Novel Approaches for Improved Performance of Inertial Sensors and Integrated Navigation Systems

Von der Naturwissenschaftlich-Technischen Fakultät der Universität Siegen
zur Erlangung des akademischen Grades

Doktor der Ingenieurwissenschaften
(Dr.-Ing.)

genehmigte Dissertation
Von

M.Sc. Ezzaldeen Edwan

1. Gutachter: Prof. Dr.-Ing. habil. Otmar Loffeld
2. Gutachter: PD Dr.-Ing. habil. Stefan Knedlik
Vorsitzender: Prof. Dr.-Ing. Claus-Peter Fritzen

Tag der mündlichen Prüfung 04.02.2013

Abstract

Navigation is the science and art that answers the questions of knowing where you are at the current moment and where you will be in the next moment. Modern navigation systems are based mainly on satellite and inertial sensors. Inertial sensor systems are becoming very popular in navigation systems because they are self contained sensors. The goal of this research is to develop novel approaches for improving the performance of inertial sensor systems and their integration algorithms with external sensors such as global positioning system (GPS) and magnetometers. The standalone inertial navigation system (INS) is dependent on the inertial measurement unit (IMU). An IMU is traditionally composed of three orthogonal gyroscopes and three orthogonal accelerometers.

In the inertial sensors side, we focus on the use of distributed accelerometers for inferring the angular motion from the angular information contained in their measurements. There exists a variety of reasons for conducting this research. In short, high quality gyros have high cost, high power consumption, large weight and large volume. On the other hand, accelerometers are less costly, easier to manufacture, have less power consumption and less weight than gyros. We developed different fusion approaches for benefiting from the angular information vector (AIV) resulting from the distributed accelerometers to form a gyro-free IMU (GF-IMU) or to aid the GF-IMU by conventional gyros. By improving the performance we mean reducing noise and bias level in the estimated inertial quantity.

In the integrated navigation side, we present different approaches to implement the GPS/INS integration filters and the attitude and heading reference system (AHRS) algorithms. We use direction cosine matrix (DCM) based algorithms which implies estimating the elements of the DCM directly within the filter. The basis for this method is the ground alignment method for attitude and heading determination. The attitude update of the DCM is performed using angle rotation vector. The filter is able to detect the gyro bias vector and follow its variation and hence it fits low-cost sensors as well as high grade sensor. We validated the efficiency of the algorithms using proper simulations and real-time implementations.

Kurzfassung

Navigation ist eine Wissenschaft und Kunst, die auf die Fragen, wo Sie zum gegenwärtigen Zeitpunkt sind und wo Sie im nächsten Moment sein werden, antwortet. Moderne Navigationssysteme basieren hauptsächlich auf Satellitensystemen und Inertialsensoren. Inertialsensoren sind in Navigationssystemen beliebt, da sie in sich geschlossene Sensoren sind. Das Ziel dieser Arbeit ist die Entwicklung neuartiger Konzepte für die Verbesserung der Leistung der Inertialsensoren und zur Sensordatenfusion mit externen Sensoren wie zum Beispiel das Globale Positionsbestimmungssystem (GPS) und Magnetometer. Ein Inertialnavigationssystem (INS) beinhaltet ein Inertiales Meßsystem (IMU). Ein IMU besteht traditionell aus drei orthogonalen Gyroskopen und drei orthogonalen Beschleunigungssensoren.

Bei den Inertialsensoren konzentrieren wir uns auf die Verwendung von verteilten Beschleunigungssensoren zum Ableiten der Rotationsbewegung aus der Winkelinformationen, die in den Messungen enthalten ist. Es gibt eine Reihe von Gründen für die Durchführung dieser Forschung. Kurz gesagt, qualitativ hochwertige Gyroskope sind teuer und haben einen hohen Stromverbrauch sowie großes Gewicht und Volumen. Auf der anderen Seite, sind Beschleunigungssensoren weniger kostspielig, leichter herzustellen, und haben einen geringeren Stromverbrauch sowie ein geringeres Gewicht als Gyroskope. Wir entwickelten verschiedene Fusionsansätze um vom Winkelinformation Vektor (AIV) zu profitieren. Diese Information wird von den verteilten Beschleunigungssensoren geliefert und zu einer Gyroskop-freien IMU (GF-IMU) geführt, die gegebenenfalls mit konventionellen Gyroskopen gestützt werden kann.

Bei der integrierten Navigation präsentieren wir verschiedene Ansätze, um die GPS / INS-Integration-Filter und die “Attitude and Heading Reference System (AHRS)” Algorithmen zu implementieren. Wir verwenden die Richtungskosinusmatrix (DCM) in den Algorithmen. Die Elemente der DCM werden innerhalb des Filters bestimmt. Die Aktualisierung der DCM erfolgt mittels Winkel-Rotationsvektor. Das Filter ist in der Lage, den Gyroskope-offset zu erkennen und seine Abweichung zu verfolgen und somit passt es zu kostengünstigen als auch zu hochwertigen Sensoren. Die Leistungsfähigkeit der Algorithmen wurde unter Verwendung geeigneter Simulationen und Echtzeit- Implementierungen demonstriert.

Table of Contents

List of Figures

List of Tables

Acknowledgements

After many years at the ZESS, I have got quite a list of people who contributed in some way to this dissertation, for which I would like to express thanks. First and foremost is my supervisor Professor Otmar Loffeld, who without his help and support this work would not be possible. I owe my deepest gratitude to the external supervisor Priv.-Doz. Stefan Knedlik who guided our navigation group before leaving to iMAR. He was not only a group leader rather he was a friendly motivating colleague. Without his support and teaching I would not be able to stand on a solid ground and have a smooth start for my PhD program. I am indebted to many of the staff members at ZESS for supporting me during doing research. I am grateful to Mr. Wolf Twelsiek for the technical support he offered in building the hardware for conducting experiments. I am indebted to the members of the navigation group: Junchuan Zhou, Zhen Dai and Cathy Zhang. Our discussions within the group's meetings have led to many useful algorithms and nicely written publications. Their encouragement and attention to me have supported me and helped me with various issues. The secretaries of ZESS Silvia Niet-Wunram, Renate Szabo and Katharina Haut, are always friendly, patient and helpful. The tutors of our graduate program Amaya Medrano Ortiz and Ashraf Samarah deserve many thanks for organizing social activities. Last but not the least; I shall be forever indebted to my wife Hanaa and my children for their everlasting love, patience, support, encouragement, sacrifice, pleasant and calm living and working atmosphere, which have certainly contributed a lot to the successful accomplishment of this dissertation. I dedicate this work to my parents.

List of Abbreviations

Acronym	Definition
ABS	Automatic Breaking System
ARW	Angle Random Walk
AHRS	Attitude and Heading Reference System
AIV	Angular Information Vector
AME	Angular Motion Estimation
CA	Constant Acceleration
CAA	Constant angular acceleration
DCM	Direction Cosine Matrix
DSP	Digital Signal Processing
ECEF	Earth Centered Earth Fixed
ECI	Earth Centered Inertial
EKF	Extended Kalman Filter
ENU	East North Up
FIR	Finite-Duration Impulse Response Filter
FOG	Fiber Optic Gyroscope
GDOP	Geometric Dilution of Precision
GF-IMU	Gyro Free Inertial Measurement Unit
GF-INS	Gyro Free Inertial Navigation System
GNSS	Global Navigation Satellite Systems
GPS	Global Positioning System
GPS/INS	Global Positioning System/ Inertial Navigation System
GSM	Global System for Mobile Communications
IEKF	Iterative Extended Kalman Filter
IMU	Inertial Measurement Unit
INS	Inertial Navigation System
KF	Kalman Filter
LSE	Least Square Error
MEMS	Micro Electromechanical systems
NGIMU	Non Gyroscopic Inertial Measurement Unit
NED	North East Down
PDOP	Position Dilution of Precision

Acronym	Definition
PPM	Parts Per Million
RLG	Ring Laser Gyroscope
RW	Random Walk
RMSE	Root Mean Square Error
SAR	Synthetic Aperture RADAR
SAW	Surface Acoustic Wave
SCKF	Smoothly Constrained Kalman Filter
UKF	Unscented Kalman Filter
USB OTG	USB on-the-go
VRW	Velocity Random Walk
ZUPT	Zero Velocity Update

List of Symbols

Symbol	Definition
$\underline{a}^b$	Acceleration vector expressed in the body frame
$\underline{b}$	Bias vector
$\underline{\alpha}$	Angular velocity change vector
Φ	Geodetic latitude angle
ϑ	Inclination angle of the Earth's magnetic field
τ	Correlation time
$\underline{\omega}_{ib}^b$	Angular velocity vector expressed in the body frame
$\underline{\dot{\omega}}_{ib}^b$	Angular acceleration vector expressed in the body frame
$\underline{\omega}_{nb}^b$	Turn rate of the body frame with respect to the navigation frame expressed in the body frame
d	Separation distance
$\underline{p}^b$	Displacement vector expressed in the body frame
F	State transition matrix
G	Input matrix
$\underline{\hat{x}}_k^-$	Predicted state estimate
$\underline{\hat{x}}_k^+$	Updated state estimate
$\underline{w}_{k-1}$	Process noise vector
P_k^+	Updated state error covariance matrix
P_k^-	Predicted state error covariance matrix
Q	Process noise covariance matrix
M	Cross correlation matrix
M_{ms}	Misalignment and scale factor matrix
K_k	Kalman gain
H	Measurement Jacobian matrix
$\underline{h}_k(\underline{\hat{x}}_k, \underline{v})$	Measurement function of state vector
m_{xx}	Misalignment element is misalignment matrix
Ψ_α	The autocorrelation function
Δt	Sampling time

Symbol	Definition
Δv	Velocity change of accelerometer
$\underline{v}$	Measurement noise vector
$\underline{z}$	Measurement vector
O	Observation matrix
O	Observability matrix
$\underline{r}^b$	Distance from the rotating point to the body center $\underline{o}^b$
$\underline{v}_{or}^b$	Velocity of point $\underline{r}^b$ with respect to the body center expressed in the body frame
$\underline{a}_{io}^b$	Measurable acceleration vector of a fixed point at the body center $\underline{o}^b$
$\underline{a}_{or}^b$	Acceleration of point $\underline{r}^b$ with respect to the body center expressed in the body frame
$\underline{g}^n$	The gravity vector in the local navigation frame $\begin{bmatrix}0 & 0 & g\end{bmatrix}^T$
θ	Pitch Euler angle
ϕ	Roll Euler angle
φ	Yaw Euler angle
$\underline{\psi}$	Euler angles vector
C_b^n	Direction cosine matrix which transforms from the body frame to the navigation frame
E_b^n	Rotation rate transformation matrix
f_x^b, f_y^b, f_z^b	Measured acceleration components expressed in the body frame
$\sigma_x, \sigma_y, \sigma_z$	Angular change components
$\underline{r}^n$	Position expressed in the local navigation frame (NED).
$\underline{v}^n$	Velocity expressed in the NED frame
ω_{ie}^n	Earth's turn rate expressed in the body frame
$\underline{\omega}_{en}^n$	Turn rate of the local navigation frame (transport rate)
$\underline{\omega}_{nb}^n$	Turn rate of the body frame with respect to the local navigation frame.

Chapter 1
Introduction

1.1 Subject of Research

The advances in micro electro mechanical systems (MEMS) technologies reduced the size and the weight of inertial sensors and introduced many novel applications. Inertial sensors are classified into accelerometers and gyroscopes. They have introduced a wide range of navigation, aerospace, industrial, medical, communications, consumer and automotive applications with improved power consumption efficiency and robustness. Inertial navigation is a self-contained navigation technique in which measurements provided by the inertial sensors are processed to track the position and orientation of an object relative to an initial position, orientation and velocity. This dissertation consists of two main parts: the first part is concerned with improving the inertial sensors performance and the second part is concerned with developing new algorithms for the integration of inertial sensors with external sensors. Since we have different contributions, the corresponding literature survey is given in the beginning of the corresponding chapter.

1.1.1 Inertial Sensors Part

In the first part of this dissertation, we focus on approaches of using distributed accelerometers to infer the angular motion and to improve the performance of a standalone inertial navigation system. A conventional inertial measurement unit (IMU) consists of three gyros for measuring the rotational motion and three accelerometers for measuring linear acceleration. In contrast to a conventional IMU, a gyro-free IMU (GF-IMU) uses a configuration of accelerometers only, to measure acceleration and rotational motion of a rigid body in 3D space. In principle, it benefits from an effect known as lever-arm effect. To have this effect the accelerometers must be distributed in distance over the body. In order to distinguish it from a conventional gyro IMU, researchers use other names interchangeably to describe its functionality. The most common used names are a GF-IMU [1-3], nongyroscopic inertial measurement unit (NGIMU) [4, 5], accelerometer based IMU and all-accelerometer IMU [6-8]. There exists a variety of reasons for using distributed accelerometers to estimate the angular velocity vector. Most of the GF-IMU publications list some of the justifications [1, 2, 4-6, 8-14]. In short, the gyroscope has typically the disadvantage of complicate manufacture technique, high cost, high power consumption, large weight, large volume, and limited dynamic range [11]. In addition, low-cost

MEMS gyroscopes have more inherent physical complexities than accelerometers [2]. On the other hand, accelerometers are smaller, less costly, and less power consuming than comparable gyros.

1.1.2 Integrated Navigation Systems Part

In the second part of this dissertation, we focus on new approaches for the integration of inertial sensors with external sensors such as global positioning system (GPS), magnetometers and barometers. The integration of the GPS with a strapdown inertial navigation system has been investigated for several years in different applications. The GPS is a global navigation satellite system that has been widely used in navigation applications in land, air and sea. The main advantage of using the GPS is obtaining absolute positioning information. The GPS position measurement accuracy is limited due to a combination of low signal strength, the limited length of the pseudo-random code, errors in the tracking loops, atmospheric delays and other errors. The inertial navigation system (INS) consists of an IMU configuration and a navigation processor that transforms the accelerometers and gyros readings into position, velocity, and attitude. The INS gives a navigation solution at higher rate as compared to the GPS but it suffers from the sensors accumulated errors caused mainly by sensors biases and noise. The INS error grows unbounded with time because of the accumulation of errors in the inertial sensors measurements. On the other hand, the GPS can provide low frequency navigation information with bounded error over time. Hence, it is commonly used to aid the INS. Due to the complementary nature of the inertial sensors measurements and the GPS measurements, intensive research efforts have been conducted to improve the integrated navigation performance. The integration of INS and GPS gives a position and attitude solution at higher rate with a bounded error due to the correction of INS error. The three categories of architectures used for GPS/INS integrations are loosely-coupled, tightly-coupled, and deeply-coupled. In this dissertation, we derive a total state loosely coupled GPS/INS integration algorithm based on the direction cosine matrix (DCM) as a state space vector to be estimated. Moreover, we develop a DCM based algorithm to estimate the attitude for attitude and heading reference system (AHRS) devices. Though the use of the DCM for attitude estimation is a subject of research, the advantages of using it for GPS/INS integration specifically have not been investigated.

1.2 Main Contributions of this Dissertation

The main contributions of this dissertation are:

- The analysis and development of a GF-IMU using a configuration of twelve fixed accelerometers and adopting a calibration procedure for the GF-IMU.
- Deriving two Kalman filters for angular motion estimation (AME) using the angular information vector (AIV). The first filter uses a direct state model space based on Euler integration. The second filter model is based on dynamic models and it is capable of estimating the bias vector in the AIV due to accelerometers' bias vector.
- Using distributed accelerometers to aid conventional gyros to avoid the drawbacks of both types of sensors and to get the best of both.
- The development of a GF-IMU using fixed and rotating accelerometers configurations and applying this principle to construct a north finding system.
- Developing and analyzing a novel DCM based GPS/INS integration algorithm and a novel DCM based attitude estimation algorithm.

The developed algorithms are verified by simulation results and a set of experimental implementations using low-cost IMUs, GPS and magnetometer triads.

1.3 The Structure of this Dissertation

The dissertation is structured as follows. In Chapter 2 we describe the inertial sensors and list the common models used to describe their errors. In Chapter 3 we describe the GF-IMU configuration of fixed accelerometers and present a calibration procedure for that GF-IMU. In that chapter we also derive a direct three state model for estimating the angular motion based on Euler integration. In Chapter 4 we describe a configuration composed of fixed and rotating accelerometers and we present a fusion approach for fusing the different types of angular information. In Chapter 5 we develop another model for estimating the angular motion based on the dynamic models. In that chapter we also derive the nonlinear constraints on the angular motion and show how to use those constraints in improving the estimation performance in constrained Kalman filtering. In Chapter 6 we derive a DCM based attitude estimation algorithm. In Chapter 7 we derive a DCM based GPS/INS integration algorithm. In Chapter 8 we give a summary for the whole dissertation and list concluding remarks about the results achieved. Moreover, we present ideas for future work.

Chapter 2
Inertial Navigation Sensors and Error Modeling

In this chapter, we introduce the inertial navigation sensors of accelerometers and gyroscopes. We also present the different categories of IMU grades and describe the different common types of inertial sensors. Moreover, we describe the reference frames used in inertial navigation. The quality of the used inertial sensors determines the accuracy of the computed inertial position and attitude.

2.1 Specifications and Grades of the IMUs

2.1.1 IMU Specifications

The important specifications parameters of the IMUs are bias error, scale-factor error, noise, and bias stability. The bias error either in gyroscopes or accelerometers is any nonzero finite measured output under the absence of rotation or acceleration. It consists of two parts: short-term deterministic offset and long-term random drift which is the bias stability. The noise level determines the minimum sensor output that is distinguishable from the background noise of the sensor or noise floor. It is dependent on the sampling frequency (bandwidth) and its density is specified in $(\text{inertial unit}/\sqrt{\text{Hz}})$. Allan variance is a tool used to measure frequency stability of clocks and to identify the stochastic errors existing in inertial sensors. For short averaging times, the Allan variance is dominated by the noise in the sensor. This gyro noise is referred to as angle random walk (ARW) and the accelerometer noise is referred to as velocity random walk (VRW). Bias stability or instability refers to changes in the bias measurement over long time. To find the bias stability, we need to know how the bias changes over time. Bias instability is found from the Allan variance plot of a long sequence of stationary sensor data. As the averaging time increases, the noise output decreases and slopes downward until it reaches a minimum point and begins to increase again and slope upward. Bias stability is defined as the minimum point on the Allan variance curve. The datasheets of IMU products have many other parameters such as range, bandwidth and linearity. Scale factor or sensitivity parameter is the ratio between the measured output and the change in sensed input and its error is the ratio of the output error over the input and is typically expressed as a percentage or parts per million (PPM)[15].

2.1.2 IMU Grades

IMUs are classified into different categories mainly based on specifications parameters and not on technology. A common mistake made by many researchers is the use of the term "MEMS grade" to describe MEMS based IMUs that mainly have poor performance parameters like consumer and automotive grades. MEMS should not be classified as a category because it is a technology and some MEMS based IMUs are already categorized under tactical grade IMUs, as HG1900 from Honeywell. Though it is common to find different categories of IMUs in inertial and integrated navigation literature, it is difficult to find authenticated resources that classify such categories according to performance parameters. We list in Table 2.1 all the available categories with performance parameters classified into five main IMU grades based on [16-18]. Reference [16] is based on a tutorial lecture [19] and a project report [20]. An interesting fact to mention here is that, many of the datasheets of IMU products focus on the gyro performance and not on accelerometer performance to classify the IMU. For example, the velocity random walk value is not given in the brochure of the HG1700 [21] IMU.

Table 2.1 IMU grades

S.	Performance Parameter	Consumer	Automotive	Tactical	Navigation I	Navigation II
Gyros	Bias Stability ($^\circ/h$)	>200	10-200	1-10	0.1-1.0	<0.01
	Scale Factor (PPM)	-	>500	200-500	100-200	5-50
	Noise Floor ARW($^\circ/\sqrt{h}$) ($^\circ/h/\sqrt{Hz}$)	3 180	3 180	0.2-0.5 12-30	0.05-0.2 3-12	0.002-0.005 0.12-0.3
Accelerometers	Bias stability (μg)	2400	1200	200-500	50-100	5-10
	Scale Factor (PPM)	-	>1000	400-1000	100-200	10-20
	Noise Floor VRW($\mu g/\sqrt{Hz}$)	1000	1000	200-400	50	5-10

The “automotive grade” or “consumer grade” categories are terms that describe the quality of inertial sensors because their primary application is in the automotive industry (active suspensions, skid control, etc.) or consumer hardware (camera stabilization, computer mice, etc.). The consumer grade parameters were first introduced by D. Gebre-Egziabher [17] as a fictitious model because it is simply a sensor package that it is two times worse than the automotive grade inertial sensors. This classification has been adopted by many other researchers.

The units of the ARW are ($^\circ/\sqrt{\text{h}}$), ($^\circ/\text{h}/\sqrt{\text{Hz}}$), ($^\circ/\text{sec}/\sqrt{\text{Hz}}$) and ($^\circ/\sqrt{\text{sec}}$) and the conversion factor between them is 1 ($^\circ/\sqrt{\text{h}}$) = 60 ($^\circ/\text{h}/\sqrt{\text{Hz}}$). The units of gyro bias stability are ($^\circ/\text{h}$), (°/sec), (rad/h) and (rad/sec) and the conversion factor between them is 1 ($^\circ/\text{h}$) = 3600 (°/sec). It should be noted that it is not necessary for all parameters of an IMU to lay under one category. For example, the KVH-5000 rate gyro triad has all parameters lie under tactical except the ARW lay under navigation I grade, but in the manufacturer website it is classified as a tactical grade. In both accelerometer and gyro, the scale-factor error will usually not be as large a contributor to total error as bias error is [15].

2.2 Reference Frames

There are different Cartesian coordinate reference frames that can be used to describe the measurements of inertial sensors and their mechanization. Reference frames are important to be defined to facilitate the understanding of the developed algorithms within this dissertation.

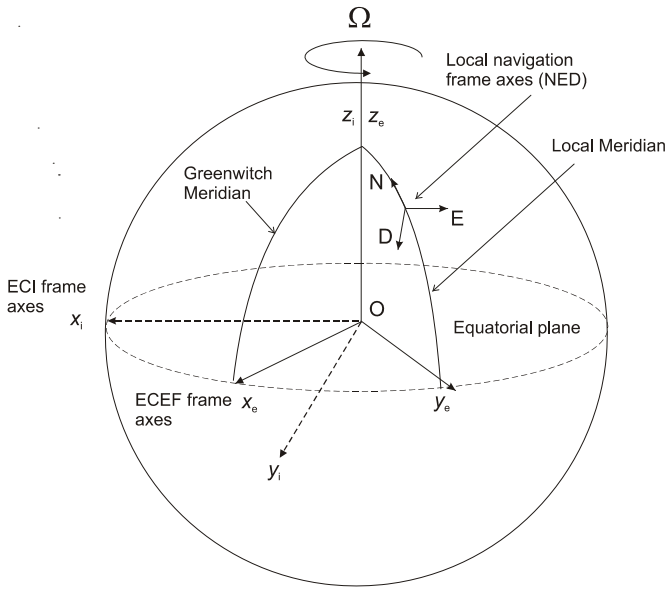

Fig. 2.1 Reference Frames

2.2.1 Earth Centered Inertial Frame (ECI)

It has its origin at the center of the earth and axes which are fixed and non-rotating with respect to fixed stars. Its z axis passes through the earth's axis of rotation and the x axis passes through the equator and is aligned to a fixed point in space, the first point of Aries. The y axis is orthogonal to the other two axes. This frame is important because inertial sensors measure motion of the body frame with respect to the inertial frame. However, it is inconvenient for terrestrial navigation because it does not account for the shape or rotation of the earth.

2.2.2 Earth Centered Earth Fixed Frame (ECEF)

The ECEF is similar to the ECI frame but it rotates at the same speed as the earth so that it remains fixed with respect to a point on the earth's surface, making it more useful for terrestrial navigation. The frame is centered on the earth with the z axis through the axis of rotation, the x axis aligned with the Greenwich Meridian, and the y axis orthogonal to complete the set. Translating coordinates from the ECI frame to the ECEF frame is relatively simple, requiring only one rotation about the z axis as a function of time to account for earth rotation.

2.2.3 Navigation Frame

It is a local geographic frame which has its origin at the location of the navigation system and axes aligned with the directions of local east, north and vertical. This frame can have different variations such as north east down (NED) or east north up (ENU). The turn rate of the navigation frame with respect to ECEF frame is often referred as transport rate.

2.2.4 Body Frame

The body frame has a set of orthogonal axes which is aligned with roll, pitch and yaw axes of the vehicle. The body frame is important to be defined because inertial sensors have measurements expressed in the body frame. The body frame is referenced with a lower case letter "b".

2.3 Inertial Sensors

We present briefly here a survey of the diverse applications of inertial sensors and highlight those with potential to benefit from our novel methods. Nowadays, there are more mobile devices such as smart phones and tablet computers which are equipped with inertial sensors and GPS receivers. Traditionally, the accelerometer is utilized for user interface control through switching from landscape or portrait views of the device's screen, based on the way the device is being held. Those devices are

good candidate to benefit from the novel approaches we developed in this dissertation because they contain the hardware and the software required for algorithms implementation. The hardware includes accelerometers, gyros, GPS receiver and the computer processor and the software includes the programming environment. Moreover, the size and the rectangular cuboid shape of those mobile devices allow them to accommodate for multiple distributed accelerometers. Hence, our developed algorithms can enhance the performance and introduce new applications for mobile devices.

Inertial sensors are deployed for motion detection in remote controllers of entertainment devices. For motion capturing, there exist different approaches such as inertial suits or optical sensing of predefined markers. Movement and pose of human body is captured and analyzed by researchers in sport, medical and character animation applications. Motion capturing is investigated in details in [22]. An old safety application of the MEMS accelerometers in cars is to sense rapid deceleration for airbag deployment. A recent application for MEMS inertial sensors in the stability and control is the Anti-Lock braking system (ABS). For a detailed automotive applications of inertial sensors we refer the reader to [23, 24]. The number of inertial sensors used can reach up to 15 accelerometers and gyros. Those redundant sensors can be used to produce angular information since they are distributed in distance [14].

2.3.1 Accelerometers

The accelerometer measures the proper acceleration which includes the gravity. Since the local gravitational constant, g, is latitude dependant, knowledge of the exact value of g is required to use the accelerometer in navigation. An accelerometer can be broadly classified into mechanical, solid state device and MEMS accelerometers. For a complete survey of accelerometers, we refer the reader to [25]. Micro-machined silicon accelerometers use the same principles as mechanical and solid state sensors. There are two main classes of MEMS accelerometer. The first class consists of mechanical accelerometers that measure the displacement of a supported mass but with MEMS manufacturing techniques. The second class consists of devices which measure the change in frequency of a vibrating element caused by a change of tension, as in surface acoustic wave (SAW) accelerometers. They are small, light and have low power consumption and start-up times. Their main disadvantage is that they are not currently as accurate as accelerometers manufactured using traditional techniques, although the performance of MEMS devices is improving rapidly.

2.3.2 Gyroscopes

Gyroscopes have different operating principles. They are used for measuring or maintaining orientation based on the principles of angular momentum. The mechanical conventional gyroscope measures the orientation and not the turn-rate as do other gyroscopes. Having moving parts causes friction and imbalance. Bearing system is used to reduce friction in the moving parts. Drift over time might result because of friction in the support bearings, external influences, and small imbalances in the spinning wheel. Optical gyroscopes are divided into two main types: the fiber optic gyroscope (FOG) and ring laser gyroscope (RLG). Mechanical and optical gyroscopes are characterized by high-precision tolerances and complicated assembly techniques which increase the manufacturing costs. On the contrary, MEMS sensors built using silicon micro-machining techniques have simpler structure and are relatively cheaper to be manufactured. MEMS gyroscopes make use of the Coriolis force to extract the angular rate. The Coriolis force is a fictitious force exerted on a body when it moves in a rotating reference frame. Vibrating elements are used to measure the Coriolis acceleration. The main categories of MEMS gyroscopes are vibrating wheel, tuning fork, wine glass resonator and Foucault pendulum gyroscopes. For an overview of the technologies of MEMS inertial sensors, we refer the reader to [26].

2.4 Inertial Sensor Error Modeling

In this dissertation, a general sensor output model is used to describe the output of inertial sensors. The main errors are bias, noise, scale factor and misalignment. In a vector form the inertial sensor triad output $\underline{z}$ is related to the reference input $\underline{s}$ as

$$\underline{z} = M_{ms}\underline{s} + \underline{b}_s + \underline{v}_s . \tag{2.1}$$

The matrix M_{ms} is assumed to be a constant matrix and it contains misalignment and scale factor elements. The bias vector $\underline{b}_s$ is modeled as a random process and it includes the deterministic bias and the bias drift. The noise vector is usually assumed to be Gaussian white noise. For a detailed survey of the different models that can be used to model the inertial sensors errors, we refer the reader to [27]. Next, we describe different random models that are often used to model the bias in inertial sensors.

2.4.1 Gauss Markov Process

This process is a random process with correlated time steps. The continuous-time form of the process is given as

$$\dot{b}(t) = -\frac{1}{\tau}b(t) + w(t) \tag{2.2}$$

where $w(t)$ is a noise driving the process and τ the correlation time. The discrete-time form of this process is

$$b_{k+1} = e^{-\frac{\Delta t}{\tau}} b_k + \sigma_b \sqrt{1 - e^{-2\frac{\Delta t}{\tau}}}\, u_k \,. \tag{2.3}$$

Considering a first order linearization for the exponential term, (2.3) can be approximated as

$$b_{k+1} = \left(1 - \frac{\Delta t}{\tau}\right) b_k + \sqrt{\frac{2\Delta t}{\tau}} \sigma_b u_k \tag{2.4}$$

where u_k is a sample from a Gaussian random number generator with a unit variance.

2.4.2 Random Walk Model

A random walk (RW) is a random process with uncorrelated time steps. It can be considered as a special case of a Gauss-Markov process

$$\dot{b}(t) = w(t) \,. \tag{2.5}$$

The discrete-time form is given as

$$b_{k+1} = b_k + w_k \,. \tag{2.6}$$

Considering a small initial value compared with the final value and large number of data samples, the random process can be approximated as

$$b_{k+1} \approx \sum_{i=1}^{i=k} w_i \,. \tag{2.7}$$

The mean of the RW process is computed as

$$E\{b_{k+1}\} \approx E\{\sum_{i=1}^{i=k} w_i\} = \sum_{i=1}^{i=k} E\{w_i\} = 0 \,. \tag{2.8}$$

The variance is computed as

$$E\{(b_{k+1})^2\} \approx E\{\left(\sum_{i=1}^{i=k} w_i\right)^2\} \,. \tag{2.9}$$

Since we have time uncorrelated noise, the variance is simplified to

$$E\{\left(\sum_{i=1}^{i=k} w_i\right)^2\} = \left(\sum_{i=1}^{i=k} E\{w_i\}^2\right) = k\sigma^2 \,. \tag{2.10}$$

Therefore, the RW process is not stationary since its variance is changing linearly with the number of samples.

2.4.3 Random Constant

The random constant process is a random process where bias remains constant so it is not time correlated model [28]. This model has the following continuous-time form

$$\dot{b}(t) = 0 . \tag{2.11}$$

The discrete-time model is given as

$$b_{k+1} = b_k . \tag{2.12}$$

2.5 Summary

In this chapter we briefly introduced the inertial sensor grades, their error models and the navigation frames used for expressing the inertial measurements. This background is essential for understanding the following chapters.

Chapter 3
Angular Motion Estimation Using Distributed Configurations of Fixed Accelerometers

In this chapter, we present an extended Kalman filter (EKF) based solution for the estimation of the angular motion using a GF-IMU built of twelve separate mono-axial accelerometers. Using such a GF-IMU produces an angular information vector, which was abbreviated as the AIV, that consists of 3D angular acceleration terms and six quadratic terms of angular velocities. We consider multiple distributed orthogonal triads of accelerometers that consist of three non-planar distributed triads equally spaced from a central triad as a specific case to solve.

3.1 Literature Survey of Inferring Angular Motion from Accelerometers

Using certain configurations of twelve separate mono-axial accelerometers produces the AIV that consists of a 3D angular acceleration vector and six quadratic terms of angular velocities, as it will be shown later. Unfortunately, the angular velocity vector is not expressed explicitly in the angular information vector. The motivation for this research is that less attention has been given to the sensor fusion of the angular information vector. The approach of using a double integration of the angular acceleration as described in [29] to achieve the orientation has been proven to be theoretically feasible but it has a faster error growth rate compared with a conventional INS. The advantage of only using the angular acceleration vector has a little value compared with the need for a double integrator. Another problem with such an approach is the need to initialize the angular velocity to be able to integrate the angular acceleration. Continuous research efforts have been conducted to benefit from the other components in the angular information vector. Recently, Park [2] aided the angular acceleration vector by three cross quadratic terms of angular velocity using an EKF, but his approach is not using all possible quadratic angular velocity terms as it is possible to get three more quadratic terms. Furthermore, such an approach suffers from an observability problem if one of the angular velocity terms is zero. Parsa [6] obtained the nine element angular information vector using the twelve accelerometers. Parsa's solution used the complete angular information vector but his focus was on the optimal design of the IMU avoiding the use of tri-axial accelerometers and not on the fusion approach, which was in a least square sense. Zappa [30] listed the rules for using twelve separate mono-axial accelerometers to obtain the angular information vector without inhibiting singularity of the

coefficient matrix. Ying Kun [14] used the same configuration of twelve accelerometers which we use in this research to have GF-INS from accelerometers that already exist in automobile's onboard control and safety systems. Again, his focus was not on sensor fusion approach; rather, he used a simple numerical approach, which might result in an imaginary solution. In our new EKF approach we use all of the six quadratic terms of angular velocity as suggested by Zappa [30] for the deterministic case but this time for the stochastic case which is the realistic one and we benefit from the angular acceleration vector at the same time. In other words, we will aid the integrated angular acceleration vector by six quadratic terms of angular velocities using an EKF.

The choice of the EKF for the fusion of the AIV is a trivial choice because we get measurable terms that have nonlinear function of the angular velocity components. The recently developed modifications of the Kalman filter for nonlinear systems, like the unscented Kalman filter (UKF), are also applicable.

3.2 Distributed Accelerometer Triad Definition

Following [31] for the derivation of the lever arm effect, we assume that we have a rigid body with its body center at point $\underline{o}^b = [0 \quad 0 \quad 0]^T$ as shown in Fig. 3.1.

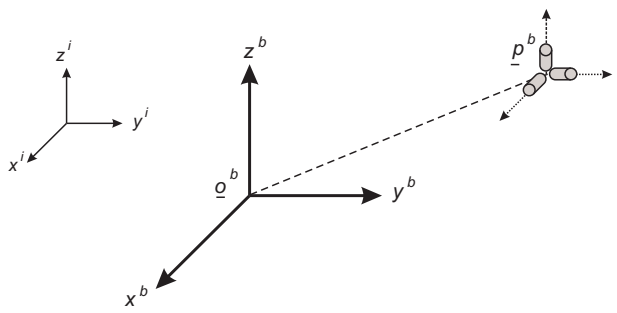

Fig. 3.1 A distributed orthogonal triad of accelerometers

The measurable acceleration of a distributed orthogonal triad of accelerometers fixed at a rigid point that is aligned with the body frame can be expressed as

$$\underline{a}_p^b = \underline{a}_o^b + \underline{g}_o^b - \underline{g}_p^b + \dot{\underline{\omega}}_{ib}^b \times \underline{p}^b + \underline{\omega}_{ib}^b \times \underline{\omega}_{ib}^b \times \underline{p}^b \tag{3.1}$$

where

$\underline{a}_o^b$: The central acceleration vector,

$\underline{p}^b$: Displacement vector from $\underline{o}^b$ to $\underline{p}^b$ equals $\underline{p}^b - \underline{o}^b$,

$\underline{g}_o^b - \underline{g}_p^b$: Local gravity difference vector,

$\underline{\omega}_{ib}^b$: Angular velocity vector,

$\dot{\underline{\omega}}_{ib}^b$: Angular acceleration vector,

$\times$: Cross product operation defined as skew symmetric form

$$\underline{\omega}_{ib}^b = \begin{bmatrix} \omega_x \\ \omega_y \\ \omega_z \end{bmatrix} \quad , \quad \underline{\omega}_{ib}^b \times = \begin{bmatrix} 0 & -\omega_z & \omega_y \\ \omega_z & 0 & -\omega_x \\ -\omega_y & \omega_x & 0 \end{bmatrix}. \tag{3.2}$$

In, (3.1) and (3.2) the superscript *b* denotes that the quantity is expressed in the body frame. The gravitational difference vector can be ignored for relatively small distribution distance and hence (3.1) simplifies to

$$\underline{a}_p^b \approx \underline{a}_o^b + \dot{\underline{\omega}}_{ib}^b \times \underline{p}^b + \underline{\omega}_{ib}^b \times \underline{\omega}_{ib}^b \times \underline{p}^b . \tag{3.3}$$

Since the angular velocity vector is not expressed explicitly in the above equation and in reality the equation is stochastic, extra efforts must be done to extract the angular velocity. One approach is to integrate the angular acceleration to get the angular velocity and to perform another integration to get the attitude. An example of such an approach, where a Kalman filter is used with external GPS observations, is given in [32]. The drawback of such an approach is that attitude and position errors grow quickly because of error growth with integration. In the following equations, we omit the body superscript as all equations in this chapter are given in the body frame. We rewrite equation (3.3) in matrix form as

$$\begin{bmatrix} a_{px} \\ a_{py} \\ a_{pz} \end{bmatrix} = \begin{bmatrix} a_{ox} \\ a_{oy} \\ a_{oz} \end{bmatrix} + \begin{bmatrix} -\omega_y^2 - \omega_z^2 & \omega_x\omega_y - \dot{\omega}_z & \omega_x\omega_z + \dot{\omega}_y \\ \omega_x\omega_y + \dot{\omega}_z & -\omega_z^2 - \omega_x^2 & \omega_y\omega_z - \dot{\omega}_x \\ \omega_x\omega_z - \dot{\omega}_y & \omega_y\omega_z + \dot{\omega}_x & -\omega_x^2 - \omega_y^2 \end{bmatrix} \begin{bmatrix} p_x \\ p_y \\ p_z \end{bmatrix}. \tag{3.4}$$

3.3 The Configuration of Multiple Distributed Accelerometer Triads

We focus on configurations consisting of twelve mono-axial accelerometers that follow the rules listed by Zappa [30]. Without loss of generality, we consider the set of four tri-axial accelerometers shown in Fig. 3.2 as an example configuration that follows Zappa's rules for extracting the AIV without inhibiting singularity of the coefficient matrix.

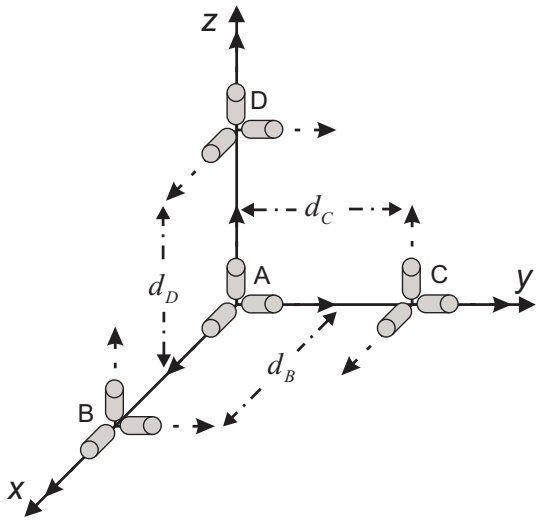

Fig. 3.2 A configuration of multiple distributed tri-axial accelerometers

Mainly, we consider this configuration because a minimum of twelve accelerometers are needed to determine the magnitude of the angular velocity and its direction (algebraic sign can not be determined uniquely as explained in [30]). The most amount of angular motion information, which is in the nine angular terms that we show next in (3.8) - (3.10) can be extracted from this configuration. Moreover, this configuration has according to [12] a low geometric dilution of precision (GDOP) factor for both angular and translational acceleration without the central accelerometer triad. In [8] it is stated that a configuration of twelve accelerometers is the only known minimum number to both navigate and determine gravity in a gravitational field with uniform gradient. Finally yet importantly, it is the most practical configuration because IMUs exist in triads of gyros and accelerometers. This specific configuration was analyzed by Algrain [33] where he derived the following relations

$$\begin{aligned}
\dot{\omega}_x &= \left(a_z^C - a_z^A\right)/2d_C + \left(a_y^A - a_y^D\right)/2d_D \\
\dot{\omega}_y &= \left(a_x^D - a_x^A\right)/2d_D + \left(a_z^A - a_z^B\right)/2d_B \\
\dot{\omega}_z &= \left(a_y^B - a_y^A\right)/2d_B + \left(a_x^A - a_x^C\right)/2d_C
\end{aligned} \tag{3.5}$$

$$\begin{aligned}
\omega_x\omega_y &= \left(a_y^B - a_y^A\right)/2d_B + \left(a_x^C - a_x^A\right)/2d_C \\
\omega_x\omega_z &= \left(a_z^B - a_z^A\right)/2d_B + \left(a_x^D - a_x^A\right)/2d_D \\
\omega_y\omega_z &= \left(a_z^C - a_z^A\right)/2d_C + \left(a_y^D - a_y^A\right)/2d_D
\end{aligned} \tag{3.6}$$

$$\begin{aligned}
\omega_x^2 &= \left(a_x^B - a_x^A\right)/2d_B + \left(a_y^A - a_y^C\right)/2d_C + \left(a_z^A - a_z^D\right)/2d_D \\
\omega_y^2 &= \left(a_y^C - a_y^A\right)/2d_C + \left(a_x^A - a_x^B\right)/2d_B + \left(a_z^A - a_z^D\right)/2d_D \\
\omega_z^2 &= \left(a_z^D - a_z^A\right)/2d_D + \left(a_x^A - a_x^B\right)/2d_B + \left(a_y^A - a_y^C\right)/2d_C
\end{aligned} \quad . \tag{3.7}$$

The notation a_{axis}^{triad} refers to the distributed accelerometer measurement with superscript referring to the triad location and subscript to the axis index. Having a unique distribution distance *d* for every distribute triad to

$$\begin{aligned}
\dot{\omega}_x &= \left(a_z^C - a_z^A - a_y^D + a_y^A\right)/2d \\
\dot{\omega}_y &= \left(a_x^D - a_x^A - a_z^B + a_z^A\right)/2d \\
\dot{\omega}_z &= \left(a_y^B - a_y^A - a_x^C + a_x^A\right)/2d
\end{aligned} \tag{3.8}$$

$$\begin{aligned}
\omega_x\omega_y &= \left(a_y^B - a_y^A + a_x^C - a_x^A\right)/2d \\
\omega_x\omega_z &= \left(a_z^B - a_z^A + a_x^D - a_x^A\right)/2d \\
\omega_y\omega_z &= \left(a_z^C - a_z^A + a_y^D - a_y^A\right)/2d
\end{aligned} \tag{3.9}$$

$$\begin{aligned}
\omega_x^2 &= \left(a_x^B - a_x^A - a_y^C + a_y^A - a_z^D + a_z^A\right)/2d \\
\omega_y^2 &= \left(a_y^C - a_y^A - a_x^B + a_x^A - a_z^D + a_z^A\right)/2d \\
\omega_z^2 &= \left(a_z^D - a_z^A - a_x^B + a_x^A - a_y^C + a_y^A\right)/2d
\end{aligned} \quad . \tag{3.10}$$

All of the previous equations are linear combinations of accelerometers measurements.

3.4 GF-IMU Error Calibration

A model that describes the sensor's output related to the reference value to be measured can approximate the behavior of most of the inertial sensors. A proper model can be established based on the data sheets provided with sensor and using lab's calibration equipments. The calibration issue of a GF-IMU has been addressed in literature before. Park [2] gives a detailed description of calibrating uni-axial accelerometers in a cube configuration GF-IMU. However, in our configuration we recommend calibrating each tri-axial independently for the following reasons:

1. Uni-axial calibration does not take into account the cross-axis sensitivities and hence another calibration for misalignment must be performed.

2. In our derivation, we assumed that all accelerometers are aligned with one frame called the body frame. Therefore, the most convenient way is to find the misalignment of each of the four triads from that common body frame.

The calibration of every accelerometer triad will be done faster because we benefit from the symmetry in the configuration by collecting measurements for the four-accelerometer triads in every flipping position. Accordingly, we suggest calibrating every tri-axial of accelerometers as a whole rather than calibrating every accelerometer independently.

There are two types of errors result in the measurable AIV in the GF-IMU. The first type of error is due to the tri-axial accelerometers' errors and the second type of error is due to errors in distributed triads locations in the geometric configuration. The error model of a tri-axial accelerometer is composed of different sources of error that can be generally classified into four parts: misalignment, scale factor, bias, and noise. We can calibrate for three sorts of errors: scale factor parameters, misalignment of accelerometers and three deterministic bias parameters in a single calibration procedure of each triad. We will find the 9-elements sensitivity matrix whose diagonal elements contain the scale factors and off diagonal elements contain misalignment parameters. Likewise, we will find the three bias elements. In a matrix form the accelerometer triad output is related to the reference specific force as

$$\begin{bmatrix} z_x \\ z_y \\ z_z \end{bmatrix} = \begin{bmatrix} m_{xx} & m_{xy} & m_{xz} \\ m_{yx} & m_{yy} & m_{yz} \\ m_{zx} & m_{zy} & m_{zz} \end{bmatrix} \begin{bmatrix} a_x \\ a_y \\ a_z \end{bmatrix} + \begin{bmatrix} b_{ax} \\ b_{ay} \\ b_{az} \end{bmatrix} + \begin{bmatrix} v_{ax} \\ v_{ay} \\ v_{az} \end{bmatrix}. \tag{3.11}$$

There are many methods to solve for *m* and *b* elements [34, 35]. Following a similar approach to the one given in [35], we rearrange (3.11) into the following form

$$\underline{z} = O\underline{\theta} + \underline{v}_a$$

$$\underline{\theta} = \begin{bmatrix} \underline{m}_1 \\ \underline{m}_2 \\ \underline{m}_3 \\ \underline{b}_a \end{bmatrix},\ \underline{m}_1 = \begin{bmatrix} m_{xx} \\ m_{xy} \\ m_{xz} \end{bmatrix},\ \underline{m}_2 = \begin{bmatrix} m_{yx} \\ m_{yy} \\ m_{yz} \end{bmatrix},\ \underline{m}_3 = \begin{bmatrix} m_{zx} \\ m_{zy} \\ m_{zz} \end{bmatrix},\ \underline{v}_a = \begin{bmatrix} v_{ax} & v_{ay} & v_{az} \end{bmatrix}^T,\ \underline{b}_a = \begin{bmatrix} b_{ax} & b_{ay} & b_{az} \end{bmatrix}^T. \tag{3.12}$$

The observation matrix for every measurement is given by

$$O = \begin{bmatrix} a_x & a_y & a_z & 0 & 0 & 0 & 0 & 0 & 0 & 1 & 0 & 0 \\ 0 & 0 & 0 & a_x & a_y & a_z & 0 & 0 & 0 & 0 & 1 & 0 \\ 0 & 0 & 0 & 0 & 0 & 0 & a_x & a_y & a_z & 0 & 0 & 1 \end{bmatrix}. \tag{3.13}$$

We stack N observations matrices from N observations to form the total measurement vector and the total observation matrix shown next

$$\begin{bmatrix} \underline{z}^1 \\ \vdots \\ \underline{z}^N \end{bmatrix} = \begin{bmatrix} O^1 \\ \vdots \\ O^N \end{bmatrix} \underline{\theta} + \begin{bmatrix} \underline{v}_a^1 \\ \vdots \\ \underline{v}_a^N \end{bmatrix} \quad \underline{z}^t = O^t \underline{\theta} + \underline{v}_a^t . \tag{3.14}$$

To have an observable system, we need a minimum of four measurements with proper values of the specific force values. To extract the m and b elements, we use least square estimation

$$\hat{\underline{\theta}} = (O^{tT} O^t)^{-1} O^{tT} \underline{z}^t . \tag{3.15}$$

For separation distances calibration, a turntable is used to measure the separation distance from every distributed accelerometer triad to the central accelerometer triad. Hence, two options can be done here:
1. Use the form of equations for the AIV that has different separation distances given in (3.5) - (3.7) with computing the corresponding error covariance to be used later in estimation.
2. Instead of using different separation distances, we can adjust it manually for every distributed triad to be unique for all and validate it experimentally. Having a unique separation distance from every distributed tri-axial to the central tri-axial simplifies computations. For this reason, we consider the equally spaced triads configuration in the rest of this dissertation.

3.5 AME Based on Three-State Model EKF

Based on the previously derived AIV (3.8) - (3.10), we can formulate the EKF setup. We are interested in estimating the angular velocity component along each body axis in 3D. In reality, the continuous-time angular velocity vector is replaced with the angular change vector as given next in (3.16) because the computerized implementation is discrete. The angular change is the sampled angular velocity multiplied by the sampling time is given as

$$\underline{x} = \begin{bmatrix} x_1 & x_2 & x_3 \end{bmatrix}^T = \begin{bmatrix} \sigma_x & \sigma_y & \sigma_z \end{bmatrix}^T . \tag{3.16}$$

3.5.1 Initialization

The initial state vector can be set as

$$\hat{\underline{x}}_0^+ = E\{\underline{x}_0\} = \begin{bmatrix} \sigma_{x_0} & \sigma_{y_0} & \sigma_{z_0} \end{bmatrix}^T . \tag{3.17}$$

The initial estimate error covariance is given as

$$P_0^+ = E\{(\underline{x}_0 - \underline{\hat{x}}_0^+)(\underline{x}_0 - \underline{\hat{x}}_0^+)^T\}. \tag{3.18}$$

3.5.2 Prediction

In discrete-time, the actual output of each accelerometer is the velocity change, hence the output of (3.8) is the angular velocity change vector $\underline{\alpha}$. The process model based on Euler integration is

$$\begin{aligned}
\sigma_{x_k} &= \sigma_{x_{k-1}} + \alpha_{x_{k-1}}\Delta t + w_{x_{k-1}} \\
\sigma_{y_k} &= \sigma_{y_{k-1}} + \alpha_{y_{k-1}}\Delta t + w_{y_{k-1}} \\
\sigma_{z_k} &= \sigma_{z_{k-1}} + \alpha_{z_{k-1}}\Delta t + w_{z_{k-1}}
\end{aligned}. \tag{3.19}$$

We define the following vector as the process input

$$\underline{u} = \underline{\alpha}\Delta t = \begin{bmatrix} \alpha_x \Delta t & \alpha_y \Delta t & \alpha_z \Delta t \end{bmatrix}^T. \tag{3.20}$$

Using (3.20), the process given in (3.19) has the linear form of

$$\begin{aligned}
\underline{x}_k &= F_{k-1}\underline{x}_{k-1} + G_{k-1}\underline{u}_{k-1} + \underline{w}_{k-1} \\
F_{k-1} &= G_{k-1} = I_{3x3}
\end{aligned}. \tag{3.21}$$

We assume the uncertainty in the process is mainly due to the uncertainty in the angular velocity change. In this work, we consider the error of each accelerometer as white Gaussian noise for simplicity. For an accelerometer error accounting for the a remaining bias, we developed a solution utilizing the dynamic models to estimate the bias parameters in the nine angular information terms given in [36]. In that solution, the bias parameters and the angular acceleration vector are appended to the state vector to form a 15-state model. For that process update, we used the Wiener process or simply the nearly constant acceleration model. When using such a model all the bias parameters in the AIV become observable under a condition that the angular acceleration has a nonzero magnitude. The three-state model has the advantage of simple calculations because only three states need to be estimated. Moreover, there is no need to make an assumption about the dynamics of the motion and hence such a solution fits most scenarios. Each accelerometer discrete-time measurement is composed of true value plus a white noise component given as

$$a_{meas} = a_{true} + w_{acc} / \sqrt{\Delta t}. \tag{3.22}$$

The white noise w_{acc} has the unit of $\mathrm{g}/\sqrt{\mathrm{Hz}}$, where g is the gravity, or its equivalent derivatives. The discrete-time white noise depends on the square root of the sampling time $\sqrt{\Delta t}$. The measured velocity change of each accelerometer is expressed as

$$\Delta v_{meas} = \Delta v_{true} + w_{acc}\sqrt{\Delta t} \ . \tag{3.23}$$

The variance R_a of each accelerometer measurement of velocity change is

$$R_a = E\left\{(\Delta v_{meas} - \Delta v_{true})^2\right\} = E\left\{w_{acc}^2\right\}\Delta t \ . \tag{3.24}$$

All accelerometers are modeled with a common upper bound of the noise variance, as it would be in reality. The error corrupting the angular acceleration vector given in (3.8) is inherited from the accelerometers' errors, as it is a linear combination of accelerometers. This combination results in a correlated process noise and its covariance is computed as

$$Q_{k-1} = (\Delta t)^2 \left(\frac{R_a}{d^2}\right) \begin{bmatrix} 1 & \frac{-1}{4} & \frac{-1}{4} \\ \frac{-1}{4} & 1 & \frac{-1}{4} \\ \frac{-1}{4} & \frac{-1}{4} & 1 \end{bmatrix} . \tag{3.25}$$

The predicted or a priori estimation error covariance is updated as

$$P_k^- = F_{k-1} P_{k-1}^+ F_{k-1}^T + Q_{k-1} \ . \tag{3.26}$$

The predicted or a priori state estimate is updated as

$$\hat{\underline{x}}_k^- = F_{k-1}\hat{\underline{x}}_{k-1}^+ + G_{k-1}\underline{u}_{k-1} \ . \tag{3.27}$$

3.5.3 Measurement Update

We plug the measured velocity changes of accelerometers in the six quadratic terms in (3.9) and (3.10) and multiply the resulting sum by the sampling time to derive the measurement of the state vector. Considering the existence of a white Gaussian noise in each accelerometer measurement, the observation inherits also a white Gaussian noise $\underline{v}$ vector

$$\underline{y}_k = \underline{h}_k(\underline{x}, \underline{v}) = \left[x_1x_2 \quad x_1x_3 \quad x_2x_3 \quad x_1^2 \quad x_2^2 \quad x_3^2 \right]_k^T + \left[v_1 \quad .. \quad v_6 \right]_k^T . \tag{3.28}$$

The Jacobian of the measurement vector is computed as

$$H_k = \left.\frac{\partial \underline{h}_k(\underline{x},\underline{v})}{\partial \underline{x}}\right|_{x=\hat{x}_k^-} = \begin{bmatrix} x_2 & x_1 & 0 \\ x_3 & 0 & x_1 \\ 0 & x_3 & x_2 \\ 2x_1 & 0 & 0 \\ 0 & 2x_2 & 0 \\ 0 & 0 & 2x_3 \end{bmatrix}_{x=\hat{x}_k^-} . \tag{3.29}$$

The measurement is correlated and its covariance is computed as

$$R_k = (\Delta t)^2 (\frac{R_a}{d^2}) \begin{bmatrix} 1 & \frac{1}{4} & \frac{1}{4} & 0 & 0 & \frac{-1}{2} \\ \frac{1}{4} & 1 & \frac{1}{4} & 0 & \frac{-1}{2} & 0 \\ \frac{1}{4} & \frac{1}{4} & 1 & -\frac{1}{2} & 0 & 0 \\ 0 & 0 & \frac{-1}{2} & \frac{3}{2} & \frac{-1}{2} & \frac{-1}{2} \\ 0 & \frac{-1}{2} & 0 & \frac{-1}{2} & \frac{3}{2} & \frac{-1}{2} \\ \frac{-1}{2} & 0 & 0 & \frac{-1}{2} & \frac{-1}{2} & \frac{3}{2} \end{bmatrix} . \tag{3.30}$$

The process noise is correlated with the measurement noise and its cross covariance is computed as

$$E\left\{\underline{w}_k \underline{v}_j^T\right\} = M_k \delta_{k-j+1} \text{ , } M_k = (\Delta t)^2 (\frac{R_a}{d^2}) \begin{bmatrix} \frac{-1}{4} & \frac{1}{4} & 0 & 0 & \frac{-1}{2} & \frac{1}{2} \\ \frac{1}{4} & 0 & \frac{-1}{4} & \frac{1}{2} & 0 & \frac{-1}{2} \\ 0 & \frac{-1}{4} & \frac{1}{4} & \frac{-1}{2} & \frac{1}{2} & 0 \end{bmatrix} . \tag{3.31}$$

The Kalman gain is updated considering a cross covariance to have a better performance as shown in the literature covering the Kalman filtering, e.g., [37] as

$$K_k = (P_k^- H_k^T + M_k)(H_k P_k^- H_k^T + H_k M_k + M_k^T H_k^T + R_k)^{-1} . \tag{3.32}$$

The corrected or a posteriori estimation error covariance is updated as

$$P_k^+ = P_k^- - K_k (H_k P_k^- + M_k^T) . \tag{3.33}$$

The corrected or a posteriori state estimate is updated as

$$\underline{\hat{x}}_k^+ = \underline{\hat{x}}_k^- + K_k (\underline{y}_k - \underline{h}_k(\underline{\hat{x}}_k^-, \underline{0})) . \tag{3.34}$$

3.6 Three-State Model Simulation Results

3.6.1 The Trajectory profile

In simulations, we consider the trajectory of stabilizing an object subject to parasitic vibrations in one dimension [38] combined with a constant angular rotation in the other dimension and no motion in the third dimension. The mathematical description of this angular motion is given as

$$\underline{\omega}(t) = [\omega_x \quad 0 \quad \omega_z \sin(2\pi ft)]^T, \ \underline{\sigma}_k = \Delta t \underline{\omega}(t_k) . \tag{3.35}$$

The sampling time Δt is chosen to be 0.01 s and the frequency of vibration f is set to 0.1 Hz. The magnitudes of angular velocity components are set to $\omega_x = 3.29$ rad/s and $\omega_z = 0.658$ rad/s . The total simulation time is 20 s and the separation distance is set to 0.1 m. We seeded white noise error of $50\mu \text{ g}/\sqrt{\text{Hz}}$ (VRW) in each accelerometer measurement. The numerical values of simulation parameters are tabulated in Table 3.1.

Table 3.1 Numerical values of the simulation parameters for three-state model

Parameter (Unit)	ω_x (rad/s)	ω_z (rad/s)	f (Hz)	Δt (s)	$w_{acc.}$ ($\text{g}/\sqrt{\text{Hz}}$)	d (m)	T (s)
Value	3.29	0.658	0.1	0.01	50μ	0.1	20

Fig. 3.3 shows a plot of the angular change profile.

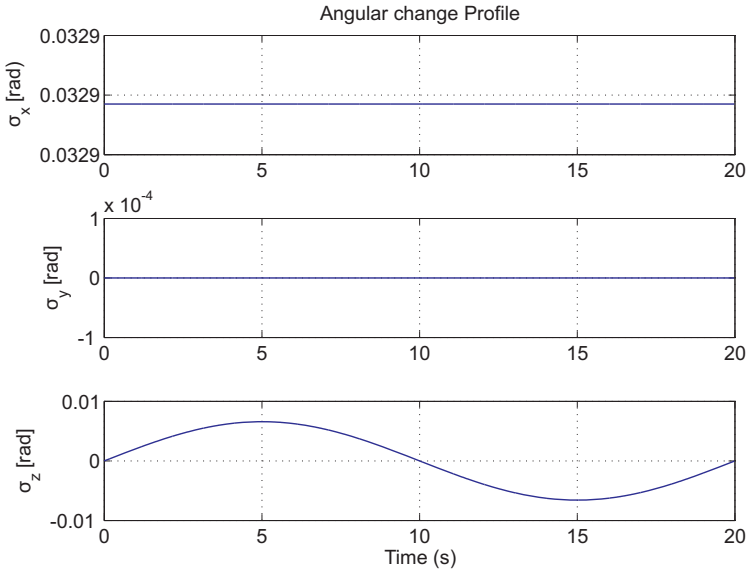

Fig. 3.3 Angular change profile

We plotted the estimation errors for the trajectory as shown in Fig. 3.4.

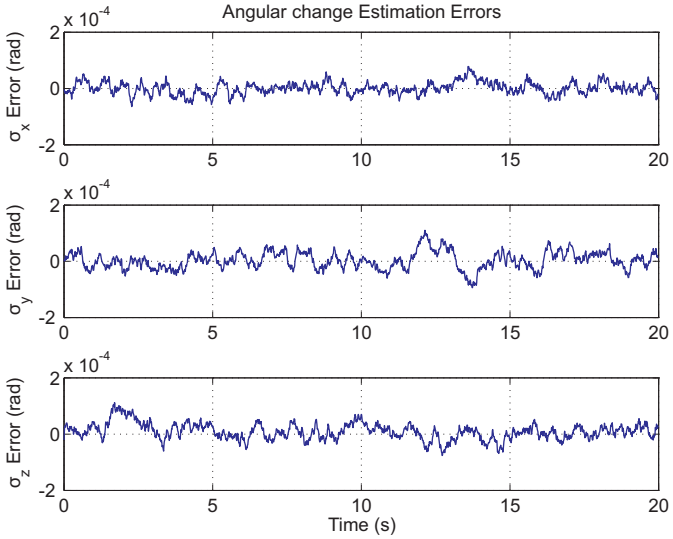

Fig. 3.4 Angular change estimation errors

3.6.2 Effect of Non-calibrated Bias

To test the effect of non-calibrated bias, we added a random a constant bias generated from a Gaussian distribution with one standard deviation of $50\,\mu g$ to each noisy accelerometer measurements. We repeated the same setup as before and created a plot of the estimation errors shown in Fig. 3.5.

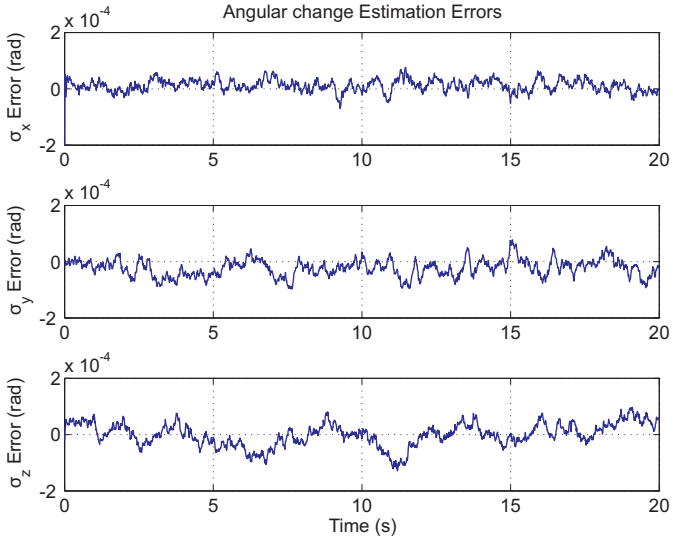

Fig. 3.5 Angular change estimation errors with bias in accelerometers

One important note here: at relatively high sampling rate (e.g., 0.01 s or more) the magnitude of the error due to white noise is about 10 times the magnitude of error due to remaining bias for a tactical grade accelerometer. Consequently, for this sampling rate, the noise error dominates the bias error in this accelerometer and for this scenario the EKF model works without big difference from the one without bias. Hence, the use of a white noise error model can be justified considering that the Kalman filter will tolerate such a small remaining bias error.

3.6.3 Effect of Improper Initialization

Here, we investigated the effect of improper initialization on the filter performance. We simulated the previously described setup under initialization errors. The initialization error is set to be equal 0.01 rad in each of three angular change components. In general, a proper sign initialization is important to avoid convergence to the opposite sign. The filter converges to the reference angular change profile because of the availability of measurements of quadratic angular change as shown in Fig. 3.6

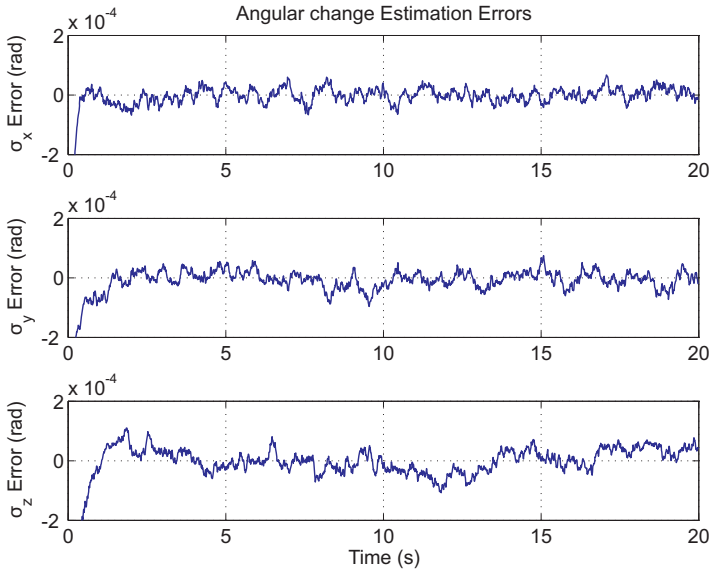

Fig. 3.6 Angular change estimation errors for improper initialization

3.7 Three-State Model Experimental Results

We built a GF-IMU using off-the-shelf components of accelerometers and processing board.

3.7.1 The Used Hardware

We use the Beagleboard as the main processing board to collect and to process data from sensors. Beagleboard, as defined by its manufacturer, is a low-cost, fan-less single board computer. It is based on an OMAP3530 application processor featuring an ARM® Cortex™-A8 running at up to 720MHz and delivering over 1,200 Dhrystone MIPS of performance via superscalar operation with highly accurate branch prediction and 256KB of L2 cache. The Beagleboard has a high-speed USB 2.0 on-the-go (OTG) port that can be utilized to provide power to the board or to deliver highly flexible expansion. By utilizing standard interfaces, the Beagleboard is highly extensible to add many features and interfaces. Among the different available ports, the I2C interface is selected to ease the reading process. The board is designed specifically to address the open source community which reduces the development costs. Some popular open source Linux distributions supported by Beagleboard are Debian, Ubuntu, Angstrom and Mamona. For implementation, we selected the Angstrom Linux which was installed on the SD/MMC card which boots from NAND memory.

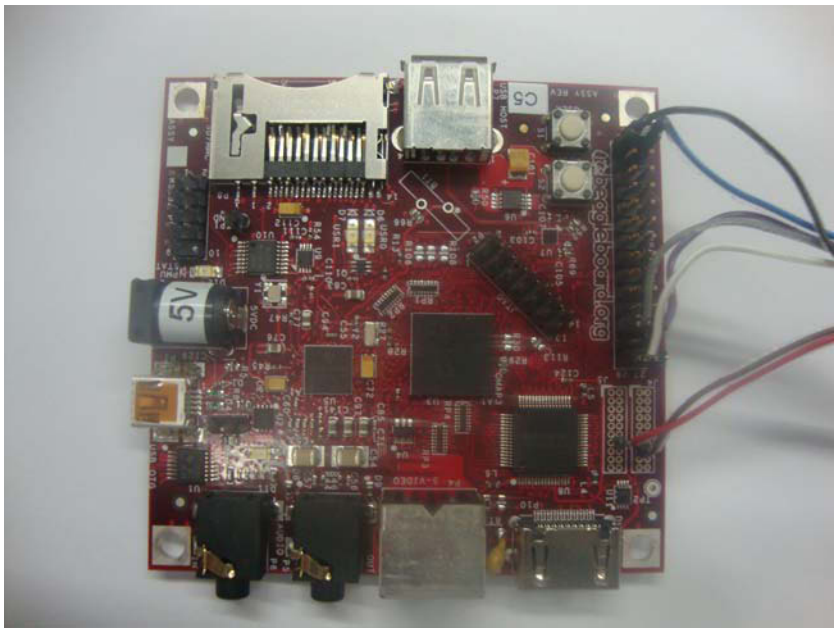

Fig. 3.7 The Beagleboard with wire connections

We use four ADXL345 accelerometer triads from Analog Devices [39]. The accelerometers are mounted on sliding platforms to allow for easy change of spacing distance. The separation distance is set to 66 cm. The sampling time is set to 0.01 s. The specifications of the used accelerometers are listed in Table 3.2 and it belongs to the consumer grade accelerometers.

Table 3.2 Specifications of the used ADXL345 accelerometers

Parameter (unit)	Value
Accelerometer noise ($m/s^2/\sqrt{Hz}$)	0.002
Accelerometer bias stability (m/s^2)	0.02
Accelerometer range (g)	$\pm 2,\ \pm 4,\ \pm 8,\ \pm 16$
Update rate Δt (s)	0.01

For comparison, we used the ITG-3200 gyro triad that has noise specifications of $0.03\ °/s/\sqrt{Hz}$ and bias specifications of $\pm 40\ °/s$ as initial bias and $\pm 40\ °/s$ as bias over temperature variation.

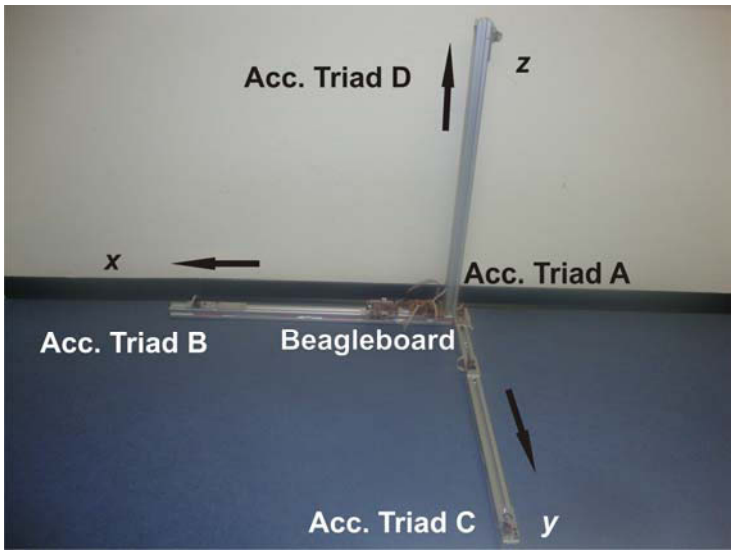

Fig. 3.8 The realized GF-IMU structure

3.7.2 Calibration Results

Accelerometer triads should be calibrated for scale factor, misalignment and bias parameters according to the procedure described in section (3.4). From the different sets of experimental data collected for different small misalignments we find that, the calibration procedure works very well regardless of the unit of the accelerometer output or orientation. However, for getting excellent result, the triad frame misalignment from the main body frame should not be large. A good indication or test that the calibration is successfully performed is having identical calibrated measurements in all triads in static position regardless of the orientation. Before calibrating the accelerometer triads we have different orientations as shown in Fig. 3.9 and after calibration parameters are applied all accelerometers have a unique orientation as shown in Fig. 3.10. Instead of using 4-positions for calibration, we used 6-

positions to achieve better calibration results. It is clear from Fig. 3.10 that the calibration is performed successfully as we see identical accelerometer outputs after calibration for the six positions symbolized P1-P6.

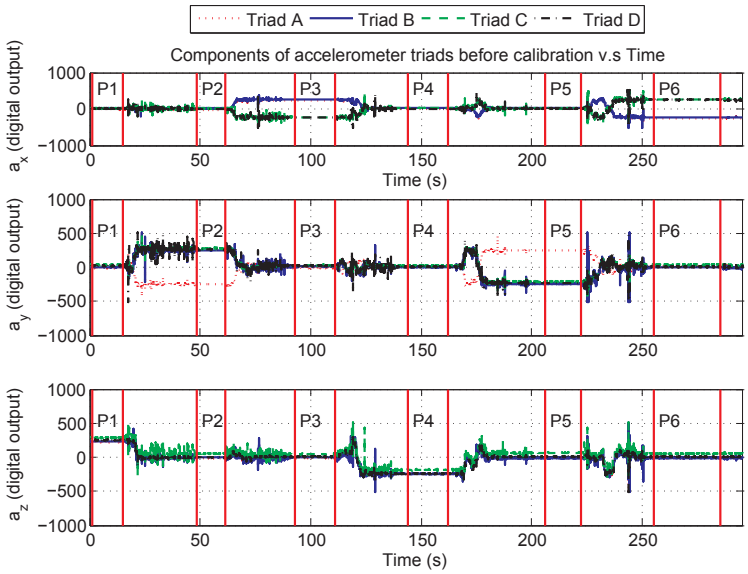

Fig. 3.9 Components of 6-positions calibration data

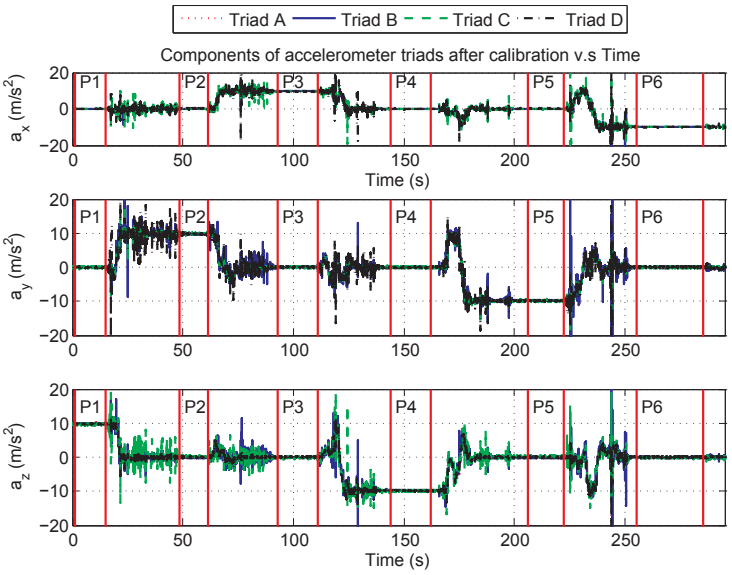

Fig. 3.10 Components of 6-positions calibration data (after calibration)

3.7.3 Free-Hand Motion Results

We generated a trajectory profile by holding with hands the structure shown in Fig. 3.8 and moving it in arbitrary different directions. In Fig. 3.11 - Fig. 3.13, we plotted the estimated angular velocity and the gyro measured components for comparison. The gyro triad bias is calibrated by capturing the bias in static moments.

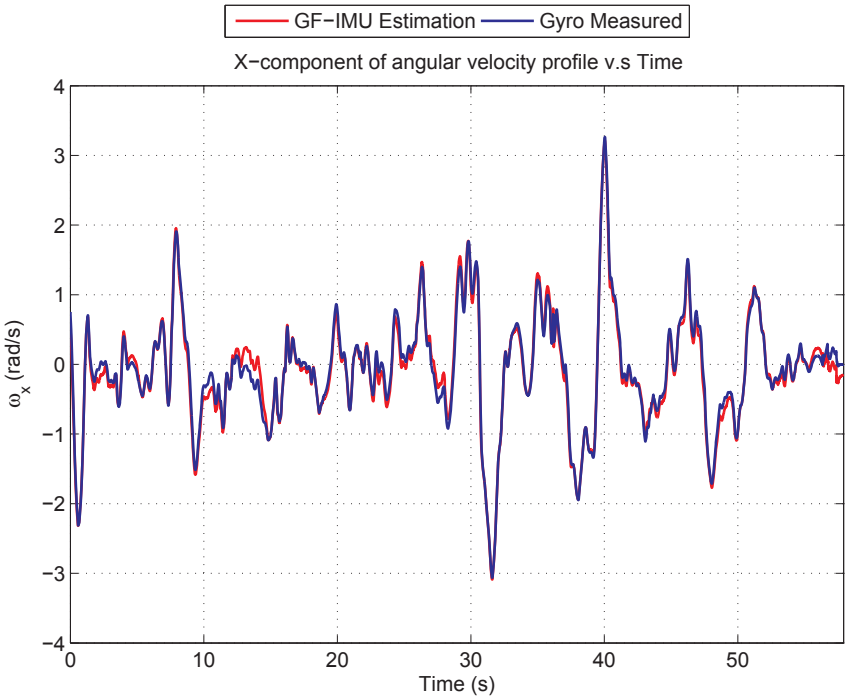

Fig. 3.11 X-component of estimated and gyro measured angular velocity (free-hand motion)

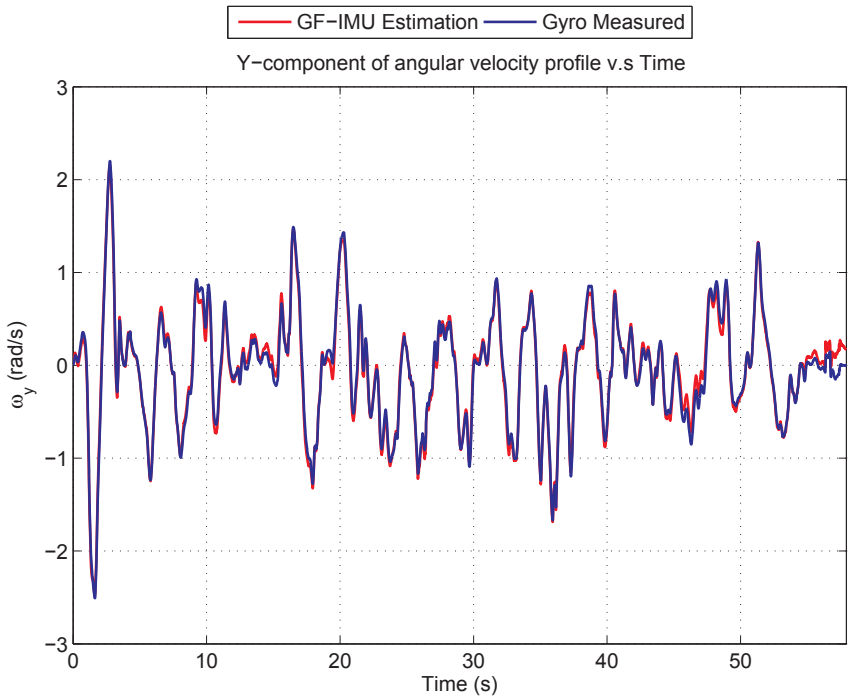

Fig. 3.12 Y-component of estimated and gyro measured angular velocity (free-hand motion)

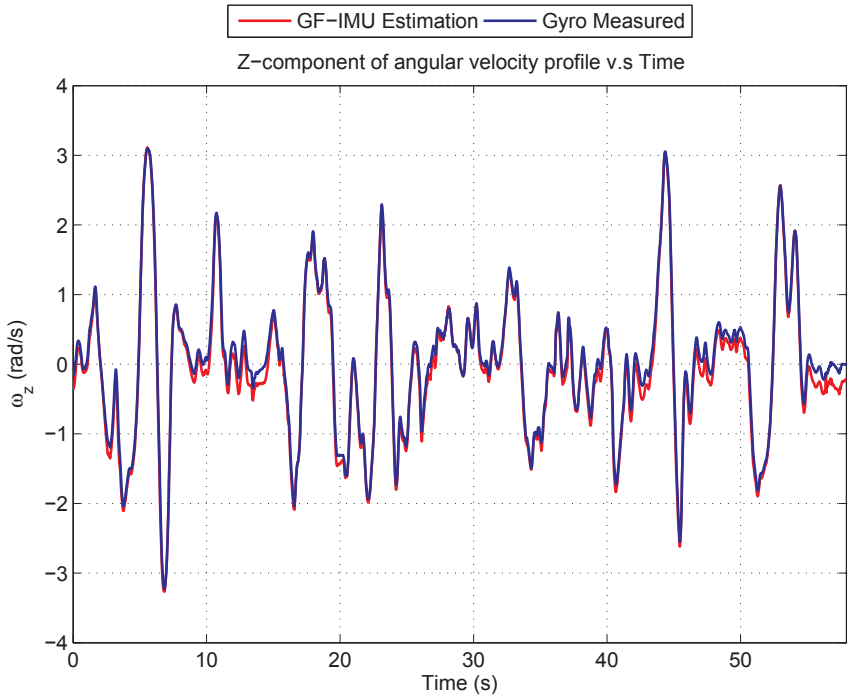

Fig. 3.13 Z-component of estimated and gyro measured angular velocity (free-hand motion)

From the plots we see that proper fusion of the AIV in the GF-IMU gives a solution that is matching the gyro triad measurement for dynamic motion.

3.7.4 Turntable Angular Motion Profile Results

The turntable gives us the possibility to assign an angular motion profile with different settings like constant velocity or constant angular acceleration. We apply a profile of different angular speed as shown in Fig. 3.14 in the *z*-axis because it is a single-axis turntable. We programmed the turntable to rotate from 1 rad/s to 5 rad/s with either having 2 rad/s^2 in accelerating periods or -2 rad/s^2 in decelerating periods.

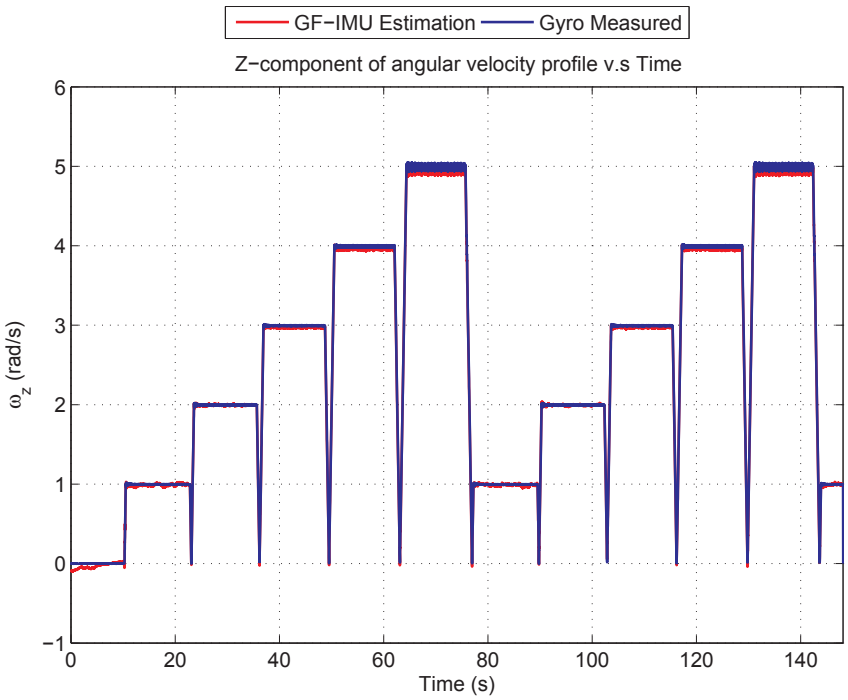

Fig. 3.14 Z-component of estimated and gyro measured angular velocity (turntable profile)

From Fig. 3.14 we see that the estimated output is able to track the programmed motion profile. It is also able to track the wobble introduced by the turntable at higher speeds as the measured gyro output has a similar behavior.

3.7.5 Effect of Varying the Angular Rate

In this part we check the effect of varying the angular rate. Through computing the variance of the estimated angular speed we try to find a relation between the magnitude of the speed and the expected resolution of the estimation. Theoretically, the estimation performance should be improved for increasing the magnitude of the angular rate and the tabulated results are in agreement with this. Higher speeds are excluded from table because of the wobble effect.

Table 3.3 shows the tabulated standard deviation errors of the steady estimated values for different speeds. Theoretically, the estimation performance should be improved for increasing the magnitude of the angular rate and the tabulated results are in agreement with this. Higher speeds are excluded from table because of the wobble effect.

Table 3.3 Effect of varying the angular speed

Angular rate $(\mathrm{rad/s})$	Std. dev. of steady estimated solution error
0	2.8×10^{-4}
1	1.5×10^{-4}
2	8.05×10^{-5}
3	6.18×10^{-5}

3.8 Summary

In this chapter, we presented a novel solution for estimating the angular motion from a multiple distributed tri-axial accelerometers measurements in a GF-IMU. The integration approach is performed using an EKF. In case of using tactical grade accelerometers or better, the error model is dominated by noise error and hence bias estimation is unnecessary and the model can be reduced to include only angular motion terms. Experimental results show that proper fusion of the AIV in the GF-IMU can solve the sign indeterminacy problem for dynamic motion. The more accurate sensors we use the higher chances for avoiding sign indeterminacy problems.

Chapter 4
Aiding Fixed Distributed Accelerometers by Rotating Accelerometers and Conventional Gyros

In this chapter, we present a novel configuration of fixed distributed accelerometers combined with rotating accelerometers to infer the angular motion. The main advantage of using rotating accelerometer over fixed one is having direct measurements of the angular velocity. This configuration can be used to find a complete attitude solution. For the static case, the heading is computed from angular velocity resulting from the Earth rotation sensed by the rotating accelerometer while tilt angles are found from the projected gravity sensed by accelerometer triad. We also summarize the benefits of using conventional gyros to aid the GF-IMU.

4.1 Motivation for Aid

The external aid to the GF-IMU is necessary in certain scenarios as we explain next.

4.1.1 Problem of Sign Indeterminacy

Any fixed distributed accelerometer set gives an angular velocity vector with undetermined sign as shown by Costello [40]. This is mainly because the quadratic terms do not give a unique angular velocity vector solution. Instead, we get two solutions. For solving this problem, some researchers propose the fusion of the angular acceleration vector with quadratic terms of angular velocity to keep the solution in the right track of sign [6] but in reality there is no guarantee for such a solution to work in all scenarios specially when the angular acceleration components are very small. For the determination of algebraic sign in a completely GF-IMU, there exist solutions using accelerometers that vibrate in a known matter with respect to the body as proposed initially by Merhav [5] and recently by Costello [9] where he gave a solution that does not require integration. The conventional low-cost gyros can be used to insure a correct sign convergence in the GF-IMU as shown in [41]. Other possible integration approaches include GPS [13, 32] and tri-axial magnetometers [7] to have a non-drifting orientation estimate; however, they are non-inertial solutions. For simplicity, we focus on practical solutions for the sign-indeterminacy problem rather than having a completely GF-IMU. The use of low-cost gyros for aiding the convergence of the angular velocity vector to the correct sign value might be a realistic and cost effective solution. Aiding GF-IMU by conventional gyros is simpler

than using rotating accelerometers. The integration result will be determined by the quality of the accelerometers and gyros used. Theoretically, a mono-axial gyro is sufficient to give the complete correct sign solution if all the angular velocities have nonzero values in 3D.

4.1.2 Increasing the Range of Measurable Angular Rate

The range of measurable angular rate depends on the range of the used accelerometers and the distribution distance. One advantage of the GF-IMU over conventional IMU could be the possibility of extending the range of the measurable angular rate. Unlike the conventional gyros, in GF-IMU angular rate range is dependent upon distance from accelerometers to the axis of rotation known as the radius of curvature.

4.2 Rotating Accelerometers and Conventional Gyros Aid

4.2.1 Previous Research on the Use of Vibrating or Rotating Accelerometers

There are intensive research efforts to deploy fixed accelerometers in inferring the angular motion, however a little attention was given to the use of rotating accelerometers. The fixed accelerometers have a simple setup; however, their use does not give an explicit expression for the angular velocity. The appearance of the quadratic terms introduces a sign indeterminacy problem as explained before. Through the use of fixed accelerometers and rotating accelerometers, we get non vanishing Coriolis force terms. A rotating accelerometer is an accelerometer that rotates at a known angular velocity around its sensing axis. The whole rotating accelerometer assembly is mounted rigidly to the IMU frame. The principle of using a moving accelerometer is used in commercial MEMS gyros. For example, the MEMS gyros from Analog Devices are based on a resonating mass that generates a Coriolis force [42]. One of the oldest approaches for inferring angular velocity from rotating accelerometers is to use only three rotating accelerometers but with many tricks like ignoring angular acceleration terms and solving using numerical integration as explained in [5]. Recently, a new approach for using a configuration of fixed and rotating accelerometers but with a larger number of rotating accelerometers, has been proposed in [9]. Our contribution is extracting the angular velocity with a less number of rotating accelerometers and without assuming any approximations which might degrade the quality of the measurements. Moreover, we still benefit from our previously described Kalman filters setups.

4.2.2 Previous Research on Gyro Aid to GF-IMU

Apparently, it might be an inappropriate approach to combine a GF-IMU with traditional gyros; however, such approach has many advantages as we will show later. For simplicity reasons, we will call this IMU which uses both approaches to sense angular rate as the hybrid IMU. There are few publications considered this option [43] [41]. In [41], the aid was proposed to overcome the sign indeterminacy problem and to improve the AME in general. In that work, the bias vector of the gyro triad was not considered. New low-cost MEMS gyros and accelerometers sensors are characterized by having lower noise; however, bias is still a problem in MEMS specially the "turn on" to "turn on" bias and bias variation over temperature. Hybrid IMU can give a bias free solution by benefiting from both types of data.

4.3 Configuration of Fixed and Rotating Accelerometers

4.3.1 Preliminary Math

We formulate our system based on the equation of motion of the measurable acceleration of a point moving in 3D within a body which also moves with respect to the inertial frame. The measurable acceleration $\underline{a}_{ir}^{b}$ of a moving point at distance $\underline{r}^{b}$ from the body center $\underline{o}^{b}$

$$\underline{a}_{ir}^{b} = \underline{a}_{io}^{b} + \underline{g}_{o}^{b} - \underline{g}_{r}^{b} + \underline{a}_{or}^{b} + 2\underline{\omega}_{ib}^{b} \times \underline{\upsilon}_{or}^{b} + \dot{\underline{\omega}}_{ib}^{b} \times \underline{r}^{b} + \underline{\omega}_{ib}^{b} \times \underline{\omega}_{ib}^{b} \times \underline{r}^{b} \tag{4.1}$$

where $\underline{a}_{io}^{b}$ is the acceleration vector at a fixed point $\underline{o}^{b}$ with respect to the inertial frame $\underline{a}_{io}^{b} = \begin{bmatrix} a_{ox} & a_{oy} & a_{oz} \end{bmatrix}^{T}$, $\underline{a}_{or}^{b}$ is the acceleration vector of moving point $\underline{r}^{b}$ with respect to $\underline{o}^{b}$ $\underline{a}_{or}^{b} = \left.\dfrac{d\underline{\upsilon}_{ob}^{b}}{dt}\right|_{b} = \begin{bmatrix} a_{bpx} & a_{bpy} & a_{bpz} \end{bmatrix}^{T}$, $\underline{\upsilon}_{or}^{b}$ is the velocity vector of point $\underline{r}^{b}$ with respect to the body center $\left.\dfrac{d\underline{r}^{b}}{dt}\right|_{b} = \begin{bmatrix} \upsilon_{bpx} & \upsilon_{bpy} & \upsilon_{bpz} \end{bmatrix}^{T}$, $\underline{\omega}_{ib}^{b}$ is turn rate of the body frame with respect to the inertial frame $\underline{\omega}_{ib}^{b} = \begin{bmatrix} \omega_{x} & \omega_{y} & \omega_{z} \end{bmatrix}^{T}$, $\dot{\underline{\omega}}_{ib}^{b}$ is the angular acceleration vector $\dot{\underline{\omega}}_{ib}^{b} = \begin{bmatrix} \dot{\omega}_{x} & \dot{\omega}_{y} & \dot{\omega}_{z} \end{bmatrix}^{T}$, $\times$ is a cross product operation defined as a skew symmetric form and $\underline{g}_{o}^{b} - \underline{g}_{p}^{b}$ is the local gravity difference vector between the two points.

In (4.1), the superscript *b* denotes that the quantity is expressed in the body frame. The gravitational difference vector can be ignored for relatively small distribution distance and hence simplifies to

$$\underline{a}_{ir}^{b} = \underline{a}_{io}^{b} + \underline{a}_{or}^{b} + 2\underline{\omega}_{ib}^{b} \times \underline{\upsilon}_{or}^{b} + \dot{\underline{\omega}}_{ib}^{b} \times \underline{r}^{b} + \underline{\omega}_{ib}^{b} \times \underline{\omega}_{ib}^{b} \times \underline{r}^{b} . \tag{4.2}$$

We rewrite (4.2) in matrix form as

$$\begin{bmatrix} a_{rx} \\ a_{ry} \\ a_{rz} \end{bmatrix} = \begin{bmatrix} a_{ox} \\ a_{oy} \\ a_{oz} \end{bmatrix} + \begin{bmatrix} a_{bpx} \\ a_{bpy} \\ a_{bpz} \end{bmatrix} + 2\begin{bmatrix} 0 & -\omega_z & \omega_y \\ \omega_z & 0 & -\omega_x \\ -\omega_y & \omega_x & 0 \end{bmatrix}\begin{bmatrix} \upsilon_{bpx} \\ \upsilon_{bpy} \\ \upsilon_{bpz} \end{bmatrix} + \begin{bmatrix} -\omega_y^2 - \omega_z^2 & \omega_x\omega_y - \dot{\omega}_z & \omega_x\omega_z + \dot{\omega}_y \\ \omega_x\omega_y + \dot{\omega}_z & -\omega_z^2 - \omega_x^2 & \omega_y\omega_z - \dot{\omega}_x \\ \omega_x\omega_z - \dot{\omega}_y & \omega_y\omega_z + \dot{\omega}_x & -\omega_x^2 - \omega_y^2 \end{bmatrix}\begin{bmatrix} p_x \\ p_y \\ p_z \end{bmatrix}. \tag{4.3}$$

We consider the following configuration of rotating and fixed accelerometers shown in Fig. 4.1 where the fixed accelerometer triads are symbolized as A, B, C, D as described previously and the mono-axial rotating accelerometers are symbolized as r_B, r_C, r_D.

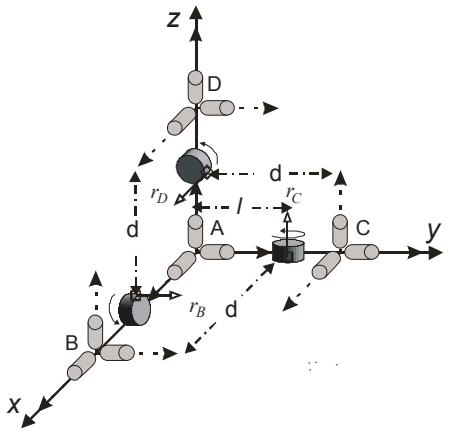

Fig. 4.1 Fixed and rotating accelerometers configuration

The rotating accelerometers have the shown positions in Fig. 4.1 at time t=0 with r_B rotates around the y axis with sensing axis along the y axis, r_C rotates around the z axis with sensing axis along the z axis and r_D rotates around the x axis with sensing axis along the x axis. For all rotating accelerometers, we assume they rotate at unique angular velocity ω_r with unique radius of rotation ρ and the center of rotation is placed at distance l from the body frame center. The position vector of the rotating accelerometer r_D on the traversed circular path is given as

$$\begin{bmatrix} p_x \\ p_y \\ p_z \end{bmatrix}_{r_D} = \begin{bmatrix} 0 \\ \rho\cos\omega_r t \\ \rho\sin\omega_r t + l \end{bmatrix}. \tag{4.4}$$

The velocity is the time derivative of the position and hence the velocity vector is derived as

$$\begin{bmatrix} v_{bpx} \\ v_{bpy} \\ v_{bpz} \end{bmatrix}_{r_D} = \frac{d}{dt}\begin{bmatrix} p_x \\ p_y \\ p_z \end{bmatrix}_{r_D} = \begin{bmatrix} 0 \\ -\rho\omega_r \sin\omega_r t \\ \omega_r \rho \cos\omega_r t \end{bmatrix}. \tag{4.5}$$

The acceleration is the time derivative of the velocity and hence the acceleration vector is derived as

$$\begin{bmatrix} a_{bpx} \\ a_{bpy} \\ a_{bpz} \end{bmatrix}_{r_D} = \frac{d}{dt}\begin{bmatrix} v_{bpx} \\ v_{bpy} \\ v_{bpz} \end{bmatrix}_{r_D} = \begin{bmatrix} 0 \\ -\rho\omega_r^2 \cos\omega_r t \\ -\omega_r^2 \rho \sin\omega_r t \end{bmatrix}. \tag{4.6}$$

Similarly for accelerometer r_B, the position of the rotating accelerometer on the traversed circle is given as

$$\begin{bmatrix} p_x \\ p_y \\ p_z \end{bmatrix}_{r_B} = \begin{bmatrix} \rho\sin\omega_r t + l \\ 0 \\ \rho\cos\omega_r t \end{bmatrix}. \tag{4.7}$$

The velocity at point r_B is derived as

$$\begin{bmatrix} v_{bpx} \\ v_{bpy} \\ v_{bpz} \end{bmatrix}_{r_B} \frac{d}{dt}\begin{bmatrix} p_x \\ p_y \\ p_z \end{bmatrix}_{r_B} = \begin{bmatrix} \omega_r \rho \cos\omega_r t \\ 0 \\ -\rho\omega_r \sin\omega_r t \end{bmatrix}. \tag{4.8}$$

The acceleration vector at point r_B is the time derivative of the velocity and it is given as

$$\begin{bmatrix} a_{bpx} \\ a_{bpy} \\ a_{bpz} \end{bmatrix}_{r_B} = \frac{d}{dt}\begin{bmatrix} v_{bpx} \\ v_{bpy} \\ v_{bpz} \end{bmatrix}_{r_B} = \begin{bmatrix} -\omega_r^2 \rho \sin\omega_r t \\ 0 \\ -\rho\omega_r^2 \cos\omega_r t \end{bmatrix}. \tag{4.9}$$

Similarly for accelerometer r_C, the position of the rotating accelerometer on the traversed circle is given as

$$\begin{bmatrix} p_x \\ p_y \\ p_z \end{bmatrix}_{r_C} = \begin{bmatrix} \rho\cos\omega_r t \\ \rho\sin\omega_r t + l \\ 0 \end{bmatrix}. \tag{4.10}$$

The velocity at point r_C is derived as

$$\begin{bmatrix} v_{bpx} \\ v_{bpy} \\ v_{bpz} \end{bmatrix}_{r_C} = \frac{d}{dt}\begin{bmatrix} p_x \\ p_y \\ p_z \end{bmatrix}_{r_C} = \begin{bmatrix} -\rho\omega_r \sin\omega_r t \\ \omega_r \rho \cos\omega_r t \\ 0 \end{bmatrix}. \tag{4.11}$$

The acceleration vector at point r_C is the time derivative of the velocity vector and it is given as

$$\begin{bmatrix} a_{bpx} \\ a_{bpy} \\ a_{bpz} \end{bmatrix}_{r_C} = \frac{d}{dt}\begin{bmatrix} \upsilon_{bpx} \\ \upsilon_{bpy} \\ \upsilon_{bpz} \end{bmatrix}_{r_C} = \begin{bmatrix} -\omega_r^2 \rho \cos\omega_r t \\ -\rho\omega_r^2 \sin\omega_r t \\ 0 \end{bmatrix}. \tag{4.12}$$

Since we are interested in the values of acceleration where the rotating accelerometers are mounted as shown in Fig. 4.1, we substitute the position, velocity and acceleration values given in (4.4) - (4.12) into (4.3) and form the following vector equation

$$\begin{bmatrix} a_x^{r_D} \\ a_y^{r_B} \\ a_z^{r_C} \end{bmatrix} = \begin{bmatrix} a_x^A \\ a_y^A \\ a_z^A \end{bmatrix} + 2\begin{bmatrix} \omega_z\omega_r\rho\sin\omega_r t + \omega_y\omega_r\rho\cos\omega_r t \\ \omega_x\omega_r\rho\sin\omega_r t + \omega_z\omega_r\rho\cos\omega_r t \\ \omega_y\omega_r\rho\sin\omega_r t + \omega_x\omega_r\rho\cos\omega_r t \end{bmatrix} + \begin{bmatrix} (\omega_x\omega_y - \dot{\omega}_z)\rho\cos\omega_r t + (\omega_x\omega_z + \dot{\omega}_y)(\rho\sin\omega_r t + l) \\ (\omega_y\omega_z - \dot{\omega}_x)\rho\cos\omega_r t + (\omega_x\omega_y + \dot{\omega}_z)(\rho\sin\omega_r t + l) \\ (\omega_x\omega_z - \dot{\omega}_y)\rho\cos\omega_r t + (\omega_y\omega_z + \dot{\omega}_x)(\rho\sin\omega_r t + l) \end{bmatrix}. \tag{4.13}$$

Equation (4.13) can be simplified by sampling at the moment where sine terms are equal to zero. In such moments the cosine terms are equal to 1. The simplified equations becomes

$$\begin{bmatrix} a_x^{r_D} \\ a_y^{r_B} \\ a_z^{r_C} \end{bmatrix} = \begin{bmatrix} a_x^A \\ a_y^A \\ a_z^A \end{bmatrix} + 2\begin{bmatrix} \omega_y\omega_r\rho \\ \omega_z\omega_r\rho \\ \omega_x\omega_r\rho \end{bmatrix} + \begin{bmatrix} (\omega_x\omega_y - \dot{\omega}_z)\rho + (\omega_x\omega_z + \dot{\omega}_y)l \\ (\omega_y\omega_z - \dot{\omega}_x)\rho + (\omega_x\omega_y + \dot{\omega}_z)l \\ (\omega_x\omega_z - \dot{\omega}_y)\rho + (\omega_y\omega_z + \dot{\omega}_x)l \end{bmatrix}. \tag{4.14}$$

The angular rate components are extracted as

$$\begin{aligned} \omega_y &= (a_x^{r_D} - a_x^A - (\omega_x\omega_y - \dot{\omega}_z)\rho - (\omega_x\omega_z + \dot{\omega}_y)l)/2\omega_r\rho \\ \omega_z &= (a_y^{r_B} - a_y^A - (\omega_y\omega_z - \dot{\omega}_x)l - (\omega_x\omega_y + \dot{\omega}_z)l)/2\omega_r\rho \\ \omega_x &= (a_z^{r_C} - a_z^A - (\omega_x\omega_z - \dot{\omega}_y)\rho - (\omega_y\omega_z + \dot{\omega}_x)l)/2\omega_r\rho \end{aligned}. \tag{4.15}$$

It should be noted that, the angular velocity can be extracted using two rotating accelerometers since the three dimensional components of the angular velocity appear in any two combinations of the rotating accelerometers equations as shown in (4.13).

4.4 Static Scenario Special Case (North-Finding System)

For a complete static attitude finding system that finds heading by sensing Earth rotation, the required number of accelerometers can be reduced to an accelerometer triad and a rotating accelerometer as shown in Fig. 4.2. Reduction is possible because the angular acceleration terms become zeros and the

quadratic terms are extremely small that they can be ignored. One common approach is to use a mono-axial rotating accelerometer that has its sensing axis along gravity to find the north [44-46]. Though the use of one accelerometer might sound to be very reasonable, the system is sensitive to errors in misalignment from horizontal position besides the need for leveling equipment. Considering that every IMU contains three accelerometers, we can benefit from those sensors to have a north finding system.

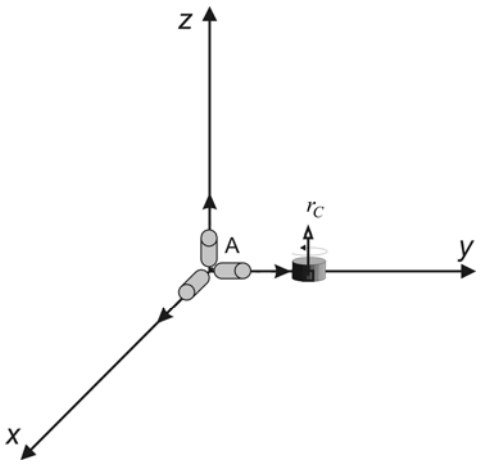

Fig. 4.2 Reduced configuration of fixed accelerometer triad and rotating accelerometer

4.4.1 System Equations

As explained before, equation (4.13) is reduced for the rotating accelerometer r_C to be

$$a_z^{r_C} = a_z^A + 2\rho\omega_r(\omega_y \sin\omega_r t + \omega_x \cos\omega_r t). \tag{4.16}$$

The index pulse determines the initial position of the rotating accelerometer and accelerometer output is sampled at a constant sampling rate. For a local navigation frame NED, the gravity and Earth rotation vectors are given as

$$\underline{g}^n = \begin{bmatrix} 0 \\ 0 \\ g \end{bmatrix},\ \underline{\omega}_{ie}^n = \begin{bmatrix} \omega_{ie}\cos\Phi \\ 0 \\ -\omega_{ie}\sin\Phi \end{bmatrix} = \begin{bmatrix} \omega_N \\ 0 \\ \omega_D \end{bmatrix} \tag{4.17}$$

where Φ is the geodetic latitude angle; ω_{ie} is the Earth turn rate and g is the gravity of the Earth. The DCM which transforms from the body frame to the navigation frame is referred as C_b^n. To transform from the body frame to the navigation frame, we need three separate rotations consisting of three angles known as Euler angles. The three sequential rotations are

Roll ϕ about x axis.

Pitch θ about y axis.

Yaw φ about z axis. The resulting rotation matrix becomes

$$C_n^b = C_3 C_2 C_1 = \begin{bmatrix} 1 & 0 & 0 \\ 0 & c_\phi & s_\phi \\ 0 & -s_\phi & c_\phi \end{bmatrix} \begin{bmatrix} c_\theta & 0 & -s_\theta \\ 0 & 1 & 0 \\ -s_\theta & 0 & c_\theta \end{bmatrix} \begin{bmatrix} c_\varphi & s_\varphi & 0 \\ -s_\varphi & c_\varphi & 0 \\ 0 & 0 & 1 \end{bmatrix}$$
$$C_b^n = (C_b^n)^T = \begin{bmatrix} c_\varphi c_\theta & c_\varphi s_\theta s_\phi - s_\varphi c_\phi & c_\varphi s_\theta c_\phi + s_\varphi s_\phi \\ s_\varphi c_\theta & c_\varphi c_\phi + s_\varphi s_\theta s_\phi & s_\varphi s_\theta c_\phi - c_\varphi s_\phi \\ -s_\theta & c_\theta s_\phi & c_\theta c_\phi \end{bmatrix} \tag{4.18}$$

where c_x, s_x and t_x represent the mathematical operations of $\cos(x)$, $\sin(x)$ and $\tan(x)$ respectively. The element in the ith row and the jth column represents the cosine of the angle between the i-axis of the reference frame and the j-axis of the body frame [25]. The tilt angles can be extracted from the gravity vector according to the following relationship

$$\begin{bmatrix} f_x^b \\ f_y^b \\ f_z^b \end{bmatrix} = C_n^b \begin{bmatrix} 0 \\ 0 \\ g \end{bmatrix}. \tag{4.19}$$

The inverse of the DCM is its transpose since it is an orthogonal matrix. Hence the measured gravity vector expressed in the body frame is given as

$$\begin{bmatrix} f_x^b \\ f_y^b \\ f_z^b \end{bmatrix} = \begin{bmatrix} c_\varphi c_\theta & s_\varphi c_\theta & -s_\theta \\ c_\varphi s_\theta s_\phi - s_\varphi c_\phi & s_\varphi s_\theta s_\phi + c_\varphi c_\phi & c_\theta s_\phi \\ c_\varphi s_\theta c_\phi + s_\varphi s_\phi & s_\varphi s_\theta c_\phi - c_\varphi s_\phi & c_\theta c_\phi \end{bmatrix} \begin{bmatrix} 0 \\ 0 \\ g \end{bmatrix}. \tag{4.20}$$

The matrix equation is simplified to the following three equations

$$\begin{aligned} f_x^b &= -g \cdot \sin\theta \\ f_y^b &= g \cdot \cos\theta \sin\phi \\ f_z^b &= g \cdot \cos\theta \cos\phi \end{aligned} \tag{4.21}$$

The pitch angle is found as

$$\theta = \sin^{-1}\left(\frac{-f_x^b}{g}\right). \tag{4.22}$$

The roll angle is found as

$$\phi = \tan^{-1}\left(\frac{f_y^b}{f_z^b}\right). \tag{4.23}$$

Next, we present two solutions for finding the heading angle. The first solution is based on synchronized demodulation. The second solution is suitable for estimation based solutions. In other words, we can handle the problem as if it is a problem for estimating the DCM elements from the measurements of the accelerometer triad and the rotating accelerometer. It can be shown that, the knowledge of the accelerometer triad measurements besides the knowledge of two angular rate components are enough to make the DCM elements observable.

4.4.2 The Leveled Case

For the leveled case, we need only a rotating accelerometer to find the north since we have zero tilt. The measurable angular rate due to Earth rotation is

$$\begin{bmatrix}\omega_x\\ \omega_y\\ \omega_z\end{bmatrix}=\begin{bmatrix} c_\varphi & s_\varphi & 0\\ -s_\varphi & c_\varphi & 0\\ 0 & 0 & 1\end{bmatrix}\begin{bmatrix}\omega_N\\ 0\\ \omega_D\end{bmatrix}=\begin{bmatrix}\omega_N\cos\varphi\\ -\omega_N\sin\varphi\\ \omega_D\end{bmatrix}. \tag{4.24}$$

Substitute (4.24) into (4.16) and using the following trigonometric identity

$$\cos(u\pm v)=\cos(u)\cos(v)\mp\sin(v)\sin(v). \tag{4.25}$$

The rotating accelerometer output becomes

$$\begin{aligned} a_z^{r_C} &= a_z^A + 2\omega_r\rho(-\omega_N\sin\varphi\sin\omega_r t+\omega_N\cos\varphi\cos\omega_r t)\\ a_z^{r_C} &= a_z^A + 2\omega_r\rho\omega_N\cos(\omega_r t+\varphi)\\ a_z^{r_C} &= g + A_c\cos(\omega_r t+\varphi) \end{aligned}. \tag{4.26}$$

Equation (4.26) shows that the measurable angular rate consists of a constant component combined with a sinusoidal signal. The sinusoidal signal holds the heading angle information in its phase angle. There are different approaches that can be used to extract the heading information. The synchronized demodulation approach is independent on bias and scale factor parameters as described in [5, 44, 45]. Assuming the accelerometer measurement has a scale factor and bias error model combined with white noise given as

$$\tilde{a}=s_a\cdot a_z^{r_C}+b_a+w_a. \tag{4.27}$$

We use the signum function of the synchronized sinusoidal wave because it requires less computation. We compute the following integral term for the signum of the cosine function

$$
\begin{aligned}
c_i &= \int_0^T \tilde{a} \cdot \mathrm{sgn}(\cos \omega_r t).dt \\
&= \int_0^T (s_a \cdot a_z^{r_C} + b_a + w_a) \cdot \mathrm{sgn}(\cos \omega_r t) \cdot dt \\
&= \int_0^T (s_a \cdot (g + A_c \cos(\omega_r t + \varphi)) + b_a + w_a) \cdot \mathrm{sgn}(\cos \omega_r t) \cdot dt \\
&= \frac{4}{\omega_r} \cdot s_a \cdot A_c \cdot \cos(\varphi) + \int_0^T (s_a \cdot g + b_a + w_a) \cdot \mathrm{sgn}(\cos \omega_r t) \cdot dt
\end{aligned}
\tag{4.28}
$$

The right side integral term vanishes if the bias combined with gravity remains constant and the white noise is considered to be considerably small. It can be approximated as

$$
c_i \approx \frac{4}{\omega_r} \cdot s_a \cdot A_c \cdot \cos(\varphi) \,. \tag{4.29}
$$

We compute the integral for the signum of the sine function

$$
\begin{aligned}
s_i &= -\int_0^T \tilde{a} \cdot \mathrm{sgn}(\sin \omega_r t) \cdot dt \\
&= -\int_0^T (s_a \cdot a_z^{r_C} + b_a + w_a) \cdot \mathrm{sgn}(\sin \omega_r t) \cdot dt \\
&= -\int_0^T (s_a \cdot (g + A_c \cos(\omega_r t + \varphi)) + b_a + w_a) \cdot \mathrm{sgn}(\sin \omega_r t) \cdot dt \\
&= \frac{4}{\omega_r} \cdot s_a \cdot A_c \cdot \sin(\varphi) - \int_0^T (s_a \cdot g + b_a + w_a).\mathrm{sgn}(\sin \omega_r t) \cdot dt
\end{aligned}
\tag{4.30}
$$

Similarly, the s_i can be approximated as

$$
s_i \approx \frac{4}{\omega_r} \cdot s_a \cdot A_c \cdot \sin(\varphi) \,. \tag{4.31}
$$

Now the azimuth angle can be extracted as

$$
\varphi = \tan^{-1}\left(\frac{s_i}{c_i}\right). \tag{4.32}
$$

Cleary, the computed value will not depend either on the scale factor or the bias. This is a great advantage because the signal is combined with harmonic signals due to vibration and using a finite-duration impulse response filter (FIR) will scale the amplitude of the filtered signal greatly.

The second approach does not require integration and it is based on our previously described method of synchronized sampling. By sampling (4.26), after filtering the constant component due to gravity and bias, at the instants when the accelerometer crosses the initial position as indicated by index pulse we get the cosine of the heading angle as

$$a_{index} = A_c \cos(\varphi) . \tag{4.33}$$

We sample again after $90°$ from the initial position to get the sine of the heading angle

$$a_{index+90°} = A_c \cos(\varphi + \frac{\pi}{2}) = -A_c \sin(\varphi) . \tag{4.34}$$

The azimuth angle is extracted as

$$\varphi = \tan^{-1}\left(\frac{-a_{index+90^0}}{a_{index}}\right). \tag{4.35}$$

This method requires much less computation than the synchronized demodulation method and it can handle the scale factor error. The constant components will be removed by the FIR filter. This method can be used to calibrate the accelerometer output after filtering by finding the magnitude of the signal A_c .

4.4.3 The Non-leveled Case

The following solution is similar to the derivation given in the leveled case as described in [45]. The measurable angular rate due to Earth rotation is

$$\begin{bmatrix}\omega_x\\ \omega_y\\ \omega_z\end{bmatrix} = \begin{bmatrix} c_\varphi c_\theta & s_\varphi c_\theta & -s_\theta \\ c_\varphi s_\theta s_\phi - s_\varphi c_\phi & s_\varphi s_\theta s_\phi + c_\varphi c_\phi & c_\theta s_\phi \\ c_\varphi s_\theta c_\phi + s_\varphi s_\phi & s_\varphi s_\theta c_\phi - c_\varphi s_\phi & c_\theta c_\phi \end{bmatrix} \begin{bmatrix}\omega_N\\ 0\\ \omega_D\end{bmatrix} = \begin{bmatrix} \omega_N c_\varphi c_\theta - \omega_D s_\theta \\ \omega_N (c_\varphi s_\theta s_\phi - s_\varphi c_\phi) + \omega_D c_\theta s_\phi \\ \omega_N (c_\varphi s_\theta c_\phi + s_\varphi s_\phi) + \omega_D c_\theta c_\phi \end{bmatrix}. \tag{4.36}$$

Substituting the values of x and y components of the angular velocity in (4.16), the rotating accelerometer output becomes

$$a_z^{r_C} = a_z^A + 2\rho\omega_r((\omega_N (c_\varphi s_\theta s_\phi - s_\varphi c_\phi) + \omega_D c_\theta s_\phi)\sin\omega_r t + (\omega_N c_\varphi c_\theta - \omega_D s_\theta)\cos\omega_r t) . \tag{4.37}$$

The following trigonometric identity is used to simplify (4.37)

$$\begin{aligned} & a\sin(x) + b\cos(x) = \sqrt{a^2 + b^2}\,\sin(x + \zeta) \\ & \zeta = \arctan\left(\frac{b}{a}\right) + \begin{cases} 0 \text{ if } a \ \geq 0 \\ \pi \text{ if } a < 0 \end{cases} \end{aligned} . \tag{4.38}$$

Using the Earth components definition given in (4.17) and the trigonometric identity, the rotating accelerometer output becomes

$$
\begin{aligned}
&a_z^{r_C} = a_z^A + 2\rho\omega_r((\omega_{ie}\,\mathrm{c}_\Phi(c_\varphi s_\theta s_\phi - s_\varphi c_\phi) - \omega_{ie}s_\Phi c_\theta s_\phi)\sin\omega_r t + (\omega_{ie}c_\Phi c_\varphi c_\theta + \omega_{ie}s_\Phi s_\theta)\cos\omega_r t)\\
&a = \omega_{ie}\,\mathrm{c}_\Phi(c_\varphi s_\theta s_\phi - s_\varphi c_\phi) - \omega_{ie}s_\Phi c_\theta s_\phi\\
&b = \omega_{ie}c_\Phi c_\varphi c_\theta + \omega_{ie}s_\Phi s_\theta\\
&a_z^{r_C} = a_z^A + 2\rho\omega_r\sqrt{a^2+b^2}\cos(\omega_r t + \zeta)\\
&\zeta = \arctan\left(\frac{b}{a}\right) + \begin{cases} 0 \text{ if } a \ge 0 \\ \pi \text{ if } a < 0 \end{cases}
\end{aligned}
\qquad (4.39)
$$

Equation (4.39) is used to extract the ζ angle in a similar way to extracting the heading angle for the leveled case. The tilt angles can be found from (4.22) and (4.23) and then substituted in (4.39)to find the unknown heading as shown in [45] where a closed form solution was derived. Rewriting (4.39) as

$$
\begin{aligned}
&a\tan(\zeta) = b\\
&(\omega_{ie}\,\mathrm{c}_\Phi(c_\varphi s_\theta s_\phi - s_\varphi c_\phi) - \omega_{ie}s_\Phi c_\theta s_\phi)\tan(\zeta)\\
&= \omega_{ie}c_\Phi c_\varphi c_\theta + \omega_{ie}s_\Phi s_\theta\\
&(\tan(\zeta)\omega_{ie}\,\mathrm{c}_\Phi\, s_\theta s_\phi - \omega_{ie}c_\Phi c_\theta)c_\varphi - \tan(\zeta)\omega_{ie}\,\mathrm{c}_\Phi\, c_\phi s_\varphi\\
&= \omega_{ie}s_\Phi(c_\theta s_\phi\tan(\zeta) + s_\theta)
\end{aligned}
\qquad (4.40)
$$

We rearrange (4.40) as

$$
\begin{aligned}
&I = \tan(\zeta)\omega_{ie}\,\mathrm{c}_\Phi\, s_\theta s_\phi - \omega_{ie}c_\Phi c_\theta\\
&J = -\tan(\zeta)\omega_{ie}\,\mathrm{c}_\Phi\, c_\phi\\
&K = \omega_{ie}s_\Phi c_\theta s_\phi\tan(\zeta) + \omega_{ie}s_\Phi s_\theta\\
&Js_\varphi + Ic_\varphi = K
\end{aligned}
\qquad (4.41)
$$

Using (4.38) again, we can solve to find the heading angle in a similar way to finding the ζ angle. We rewrite (4.41) as

$$
\begin{aligned}
&\sqrt{I^2+J^2}\sin(\varphi+\varsigma) = K\\
&\varsigma = \arctan\left(\frac{I}{J}\right) + \begin{cases} 0 \text{ if J} \ge 0 \\ \pi \text{ if J} < 0 \end{cases}
\end{aligned}
\qquad (4.42)
$$

The heading angle is computed as

$$
\varphi = \arcsin\left(K \Big/ \sqrt{I^2+J^2}\right) - \varsigma\,. \qquad (4.43)
$$

The second method using synchronized sampling has the advantage of less computation. Using (4.16), we find ω_x by sampling at the initial position and ω_y by sampling again after 90° from the initial position. Those two components are substituted in (4.36) to find the unknown heading. The nonlinear equations can be solved either numerically or handled as estimation problem for estimating the DCM elements [47].

4.5 Experimental Results

4.5.1 Rotating Accelerometer Design Example

Before doing the experimental implementation of the system we give the numerical values for a design example to show the feasibility of using rotating accelerometers in detecting small angular rate values. We assign the parameters values based on specifications of accelerometers from the market and with distance parameters that give the system portability.

Table 4.1 Numerical values for rotating accelerometer design example

Parameter (Unit)	l (cm)	ρ (cm)	Δt (s)	$w_{acc.}$ ($\mu g/\sqrt{Hz}$)	b_a (μg)	d (cm)	ω_r (rad/s)
Value	10	2	0.01	1	2400	15	50

We compute the variance of the angular velocity component noise, which is also known as ARW, based on (4.14) as

$$\sigma_g^2 = R_a(1/(2\omega_r^2\rho^2) + 1/(2\omega_r^2 d^2) + l^2/(2\omega_r^2 d^2\rho^2)) . \tag{4.44}$$

Based on the parameter values given in Table 4.1, we get the following variance

$$\sigma_g^2 = 0.7311R_a . \tag{4.45}$$

The computed standard deviation of the measurable angular velocity is

$$\sigma_g = 8.38\mu \text{ (rad/s}/\sqrt{\text{Hz}}) = 4808.38\mu \text{ (°/s}/\sqrt{\text{Hz}}) = 1.7 \text{ (°/h}/\sqrt{\text{Hz}}) . \tag{4.46}$$

For different values of rotational speeds of the accelerometer we tabulated the computed standard deviation of measurable angular velocity as shown in Table 4.2.

Table 4.2 Computed standard deviation of angular rate for different rotational speeds

Rotational speed ω_r (rad/s)	50	100	500
Measurable rate std. dev. σ_g (°/h/$\sqrt{Hz}$)	1.7	0.85	0.17

The tabulated values show the possibility of having measurable angular rate with extremely small ARW values.

4.5.2 Technical Issues Regarding Implementation and Calibration

The calibration procedure described in section 3.4 is applicable to fixed accelerometers. The rotating accelerometers are calibrated independently from the fixed accelerometers using a different approach.

The scale factor can be found as described previously in subsection 4.4.2. A constant turn rate of a rotating accelerometer is not necessary but an exact knowledge of the rotation rate is important. The measurement of the accelerometer's rotation rate is achieved using an optical encoder. The rotation can be achieved using a rotating module built of a motor equipped with an encoder and supplied with a slip ring or using a vibrating accelerometer. The slip ring transmits the accelerometer's output signal and power connections from the rotating part.

4.5.3 Experimental Setup for North Finding System

We implemented two experimental setups of using the rotating accelerometers as a north finding system. The sampled output of the accelerometer during rotation should represent a sinusoidal signal. We experiment with two configurations, one is using an ACUTRONIC single-axis turntable as shown in Fig. 4.3 and the other one is using a rotating module as shown in Fig. 4.4. Instead of using one accelerometer we used two accelerometers mounted on both sides of the rotating rod to increase the S/N ratio and to remove vibration. More using two accelerometers we get a balanced setup. A turntable is used to operate at different speeds. The used accelerometers are of the type SF1500S.A from Colibrys.

Fig. 4.3 Reduced configuration of rotating accelerometers using turntable

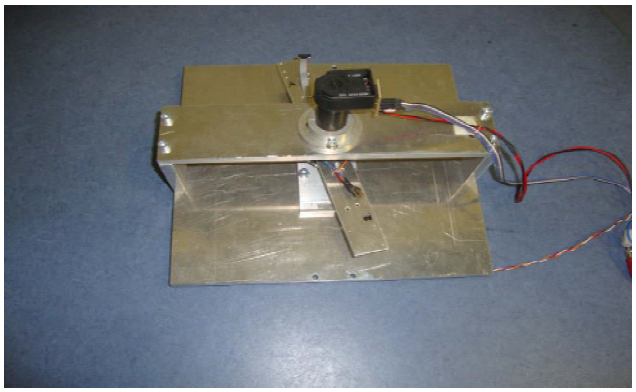

Fig. 4.4 Reduced configuration of rotating accelerometers using a rotating module

The separation distance is set to 28 cm. A DSP based platform with 24 bit analog to digital converter (ADC) is used to acquire data at a sampling rate of 512 Hz. The rotation speed is 200 rpm so the frequency of the sinusoidal signal should be f=3.333 Hz. The time series output is extremely noisy as shown in Fig. 4.5.

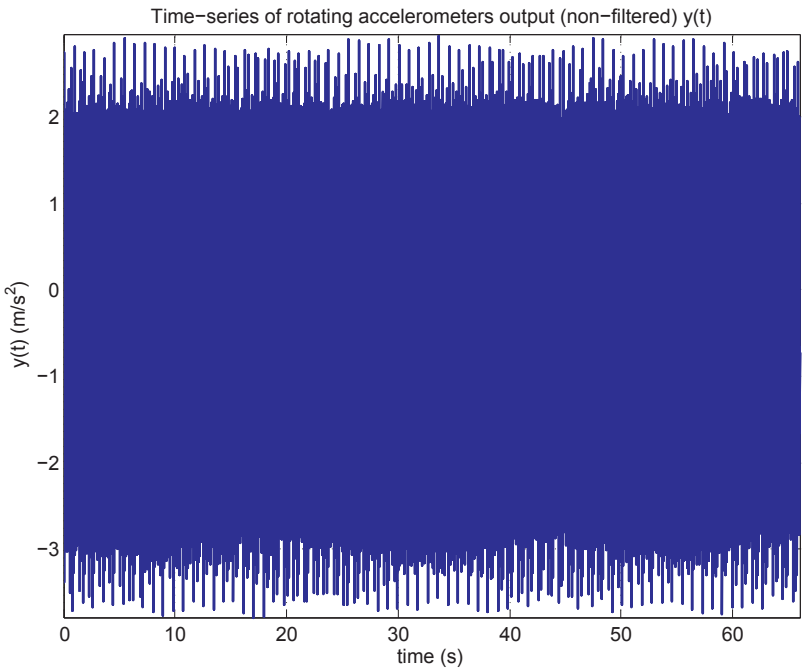

Fig. 4.5 Time series accelerometer output

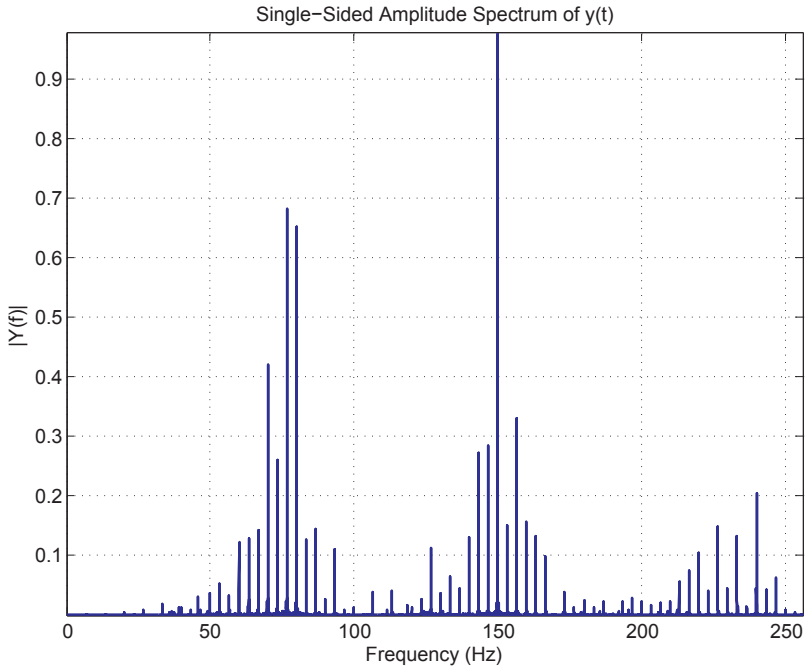

Fig. 4.6 The corresponding single-sided amplitude spectrum

Fig. 4.6 shows the corresponding spectrum of the accelerometer output. It shows that the harmonics have much higher amplitude than the desired signal. Though we use high quality turntable, such harmonics can not be avoided and we should filter out the signal. We tried to reduce vibration mechanically by balancing the rod during rotations; however, such harmonics are difficult to be filtered mechanically. From the spectrum, we can see that band pass frequency filtering is a suitable solution.

4.5.4 Filtering the Signal

FIR filters have many advantages such as phase linearity and stability. They can be realized in hardware or software. The filter simply performs a linear combination of current and previous values of the input signal

$$y(n) = \sum_{m=0}^{M} b_m x(n-m) . \tag{4.47}$$

The z transform is given as

$$H(z) = \sum_{m=0}^{M} b_m z^{-m} . \tag{4.48}$$

The filter order determines the filter complexity.

4.5.5 Successive Steps Experiment

We rotated the turntable in 5 successive steps with the turn rate kept constant in every step and each step has roughly 10 degrees difference from the previous. We do so since in this case we do not need accurate reference of north. We check if north finding system is able to track the difference between successive steps. The signal is band-pass filtered using FIRLS function in Matlab. The filtered signal has initially overshot but shortly it converges as shown in Fig. 4.7 for one position for duration of 66 seconds. Fig. 4.8 is a zoom window of the filtered signal to show the stable sinusoidal wave.

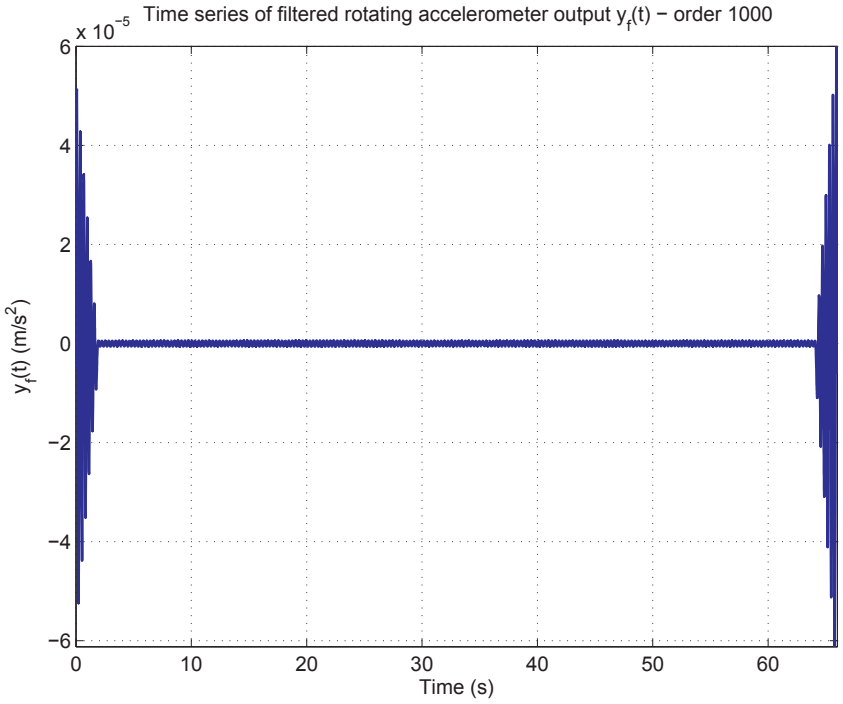

Fig. 4.7 Time-series of filtered accelerometer output

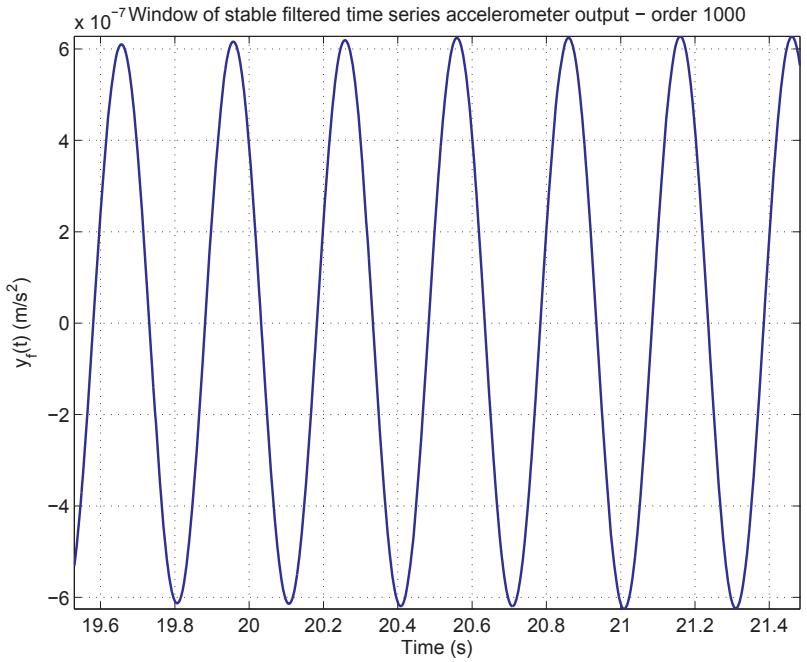

Fig. 4.8 Window of stable filtered time series signal

The sinusoidal periods are averaged to produce one sinusoidal period to improve the accuracy of the computed heading angle as shown in Fig. 4.9.

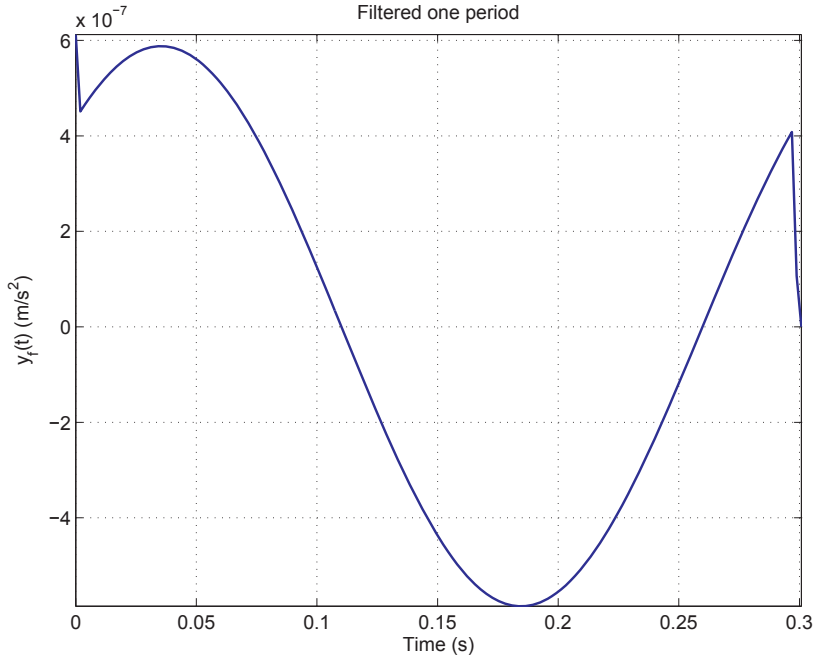

Fig. 4.9 Filtered one period

Table 4.3 Estimated heading angle for different positions

Order	Azimuth (º) Order 2000		Azimuth (º) Order 1000		Azimuth (º) Order 200	
Step	Syn. d.	Syn. s.	Syn. d.	Syn. s.	Syn. d.	Syn. s.
1	-42.076 -42.282	-40.859	-42.058 -42.262	-41.805	-42.119 -42.290	-49.616
2	-51.560 -51.761	-49.986	-51.592 -51.791	-50.891	-51.563 -51.742	-53.798
3	-64.745 -64.902	-62.844	-64.780 -64.936	-63.519	-64.651 -64.772	-69.221
4	-73.859 -73.967	-71.715	-73.855 -73.961	-72.271	-73.660 -73.751	-75.406
5	-82.375 -82.425	-80.156	-82.399 -82.447	-80.604	-82.216 -82.245	-83.744

For digital integration, we use the rectangular and trapezoidal integration methods. Results of the two methods of integration are shown respectively in Table 4.3 in the "Syn. d." column and compared with the synchronized sampling method in "Syn. s." column. We compute the heading angle for three filter orders. The computed values show that increasing FIR order above 200 has little effect on improving the heading angle accuracy. Moreover, changing the integration method from trapezoidal to rectangular has small effect on the result. The computed heading angles are in harmony with the steps change. The synchronized demodulation method is more robust than synchronized sampling method especially for low-order FIR filter. The synchronized sampling method requires a higher sampling rate for efficient FIR filtering.

4.6 Gyro Aided GF-IMU Using Three-state EKF Model

The aid of conventional gyro triad to the GF-IMU constitutes a new type of IMU that we call a hybrid IMU to distinguish it from the GF-IMU and the conventional IMU. Next, we describe the filter briefly since it is similar to the one given in section 3.5 with state vector to be estimated given as

$$\underline{x} = \begin{bmatrix} x_1 & x_2 & x_3 \end{bmatrix}^T = \begin{bmatrix} \sigma_x & \sigma_y & \sigma_z \end{bmatrix}^T . \tag{4.49}$$

The only difference will be adding a vector measurement coming from the gyro triad.

4.6.1 Initialization and Prediction

We can use the direct gyro measurement vector for initialization

$$\hat{\underline{x}}_0^+ = E\{\underline{x}_0\} = \begin{bmatrix} \sigma_{x_0} & \sigma_{y_0} & \sigma_{z_0} \end{bmatrix}^T = \begin{bmatrix} \sigma_{x_{meas}} & \sigma_{y_{meas.}} & \sigma_{z_{meas.}} \end{bmatrix}^T . \tag{4.50}$$

The initial estimate error covariance is set to the gyro variance since it is the best available information

$$P_0^+ = E\{(\underline{x}_0 - \hat{\underline{x}}_0^+)(\underline{x}_0 - \hat{\underline{x}}_0^+)^T\} = (\Delta t)^2 R_g I_{3\times 3} . \tag{4.51}$$

The predicted state vector and estimation error covariance are updated as given in the equation set (3.19)-(3.27).

4.6.2 Measurement Update

The measurement vector $\underline{h}$ is composed of the directly measured angular change vector by a triad of gyros and the quadratic terms and it is corrupted with a white noise vector and it is given as

$$\underline{y}_k = \underline{h}_k(\underline{x}, \underline{v}) = \begin{bmatrix} x_1 & x_2 & x_3 & x_1x_2 & x_1x_3 & x_2x_3 & x_1^2 & x_2^2 & x_3^2 \end{bmatrix}_k^T + \begin{bmatrix} v_1 & .. & v_9 \end{bmatrix}_k^T . \tag{4.52}$$

The measurement Jacobian matrix is computed as

$$H_k = \left.\frac{\partial \underline{h}_k(\underline{x}, \underline{v})}{\partial \underline{x}}\right|_{x=\hat{x}_k^-} = \begin{bmatrix} I_{3\times 3} & H_{12} \end{bmatrix}_{x=\hat{x}_k^-}^T , \quad H_{12} = \begin{bmatrix} x_2 & x_3 & 0 & 2x_1 & 0 & 0 \\ x_1 & 0 & x_3 & 0 & 2x_2 & 0 \\ 0 & x_1 & x_2 & 0 & 0 & 2x_3 \end{bmatrix} . \tag{4.53}$$

The gyros' measurements are uncorrelated with accelerometers' measurements and hence the covariance of the measurement vector is computed as

$$R_k = \begin{bmatrix} (\Delta t)^2 R_g I_{3\times 3} & 0_{3\times 6} \\ 0_{6\times 3} & R_{22} \end{bmatrix} . \tag{4.54}$$

where R_{22} is as given in (3.30). The Kalman gain, the a posteriori estimation error covariance and the a posteriori state estimate are updated as given in the equation set (3.32)-(3.34).

4.7 Simulation Results

4.7.1 Trajectory Profile

Again we use the same angular velocity profile used before with the mathematical description as given in (3.35). The simulation parameters for the accelerometers are set as given in section 3.6.1 and the gyros triad has gyros noise of $w_g = 3\ ^\circ/\sqrt{h}$. In simulations we compare the performance of the GF-

IMU with the performance of the hybrid IMU. The state vector is initialized properly around the true state with initial state error of 5% of the true value for both cases.

Table 4.4 Numerical values of the simulation parameters for the hybrid IMU

Parameter (Unit)	ω_x (rad/s)	ω_z (rad/s)	f (Hz)	Δt (s)	$w_{acc.}$ ($g/\sqrt{Hz}$)	w_g ($^\circ/\sqrt{h}$)	d (m)	T (s)
Value	3.29	0.658	1	0.01	$50\,\mu$	3	0.2	10

4.7.2 Results and Analysis

The angular change profiles of true, gyros measured, GF-IMU estimations and hybrid estimations are plotted in Fig. 4.10 - Fig. 4.12 for the three dimensional components. The gyro measured output is the gyro triad measurement while the GF-IMU estimation is the solution given by GF-IMU. The hybrid estimation is the solution which combines the GF-IMU solution and the gyro measurement.

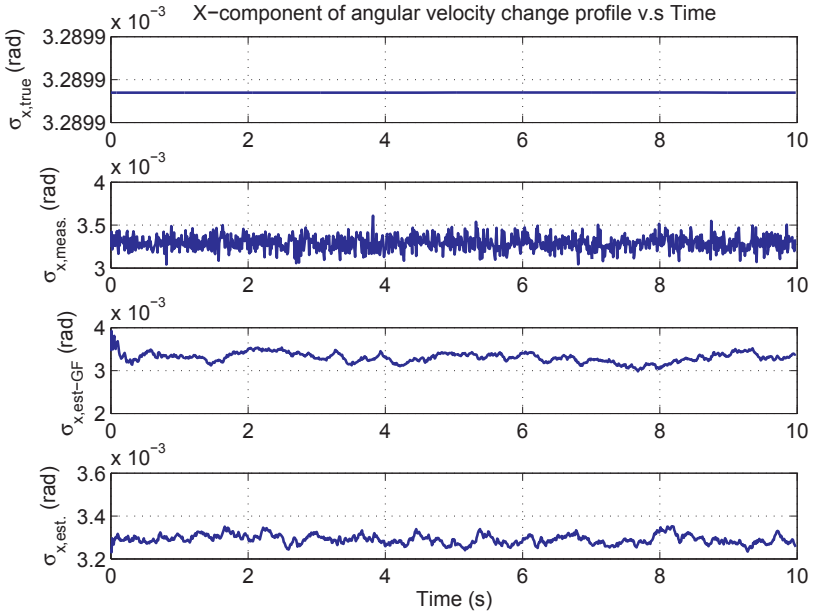

Fig. 4.10 X-component of estimated and measured angular velocity change

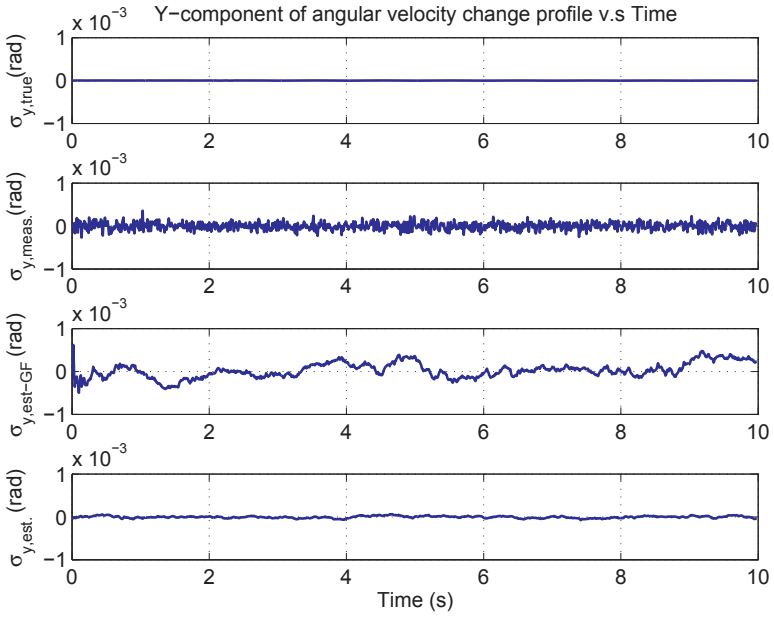

Fig. 4.11 Y-component of estimated and measured angular velocity change

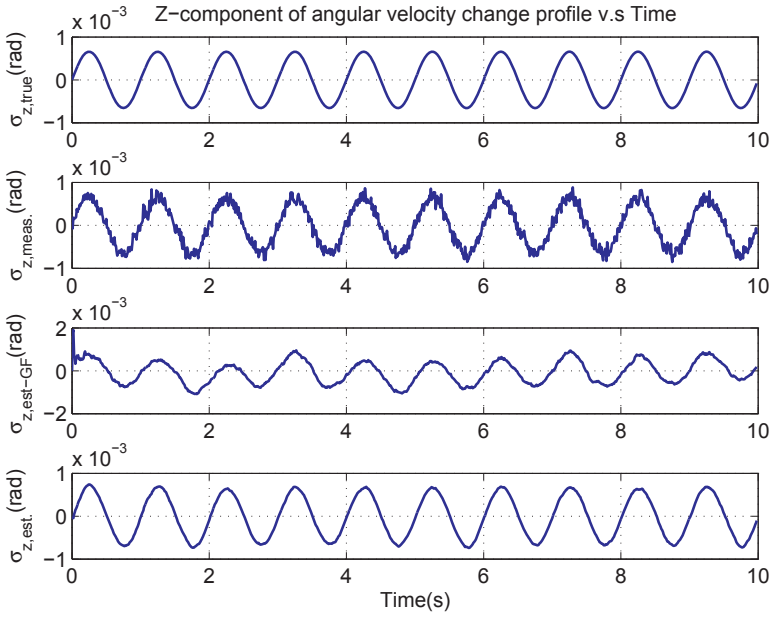

Fig. 4.12 Z-component of estimated and measured angular velocity change

Estimations and measurement errors of angular change are also plotted in Fig. 4.13, Fig. 4.14 and Fig. 4.15 to show the magnitude of error clearly

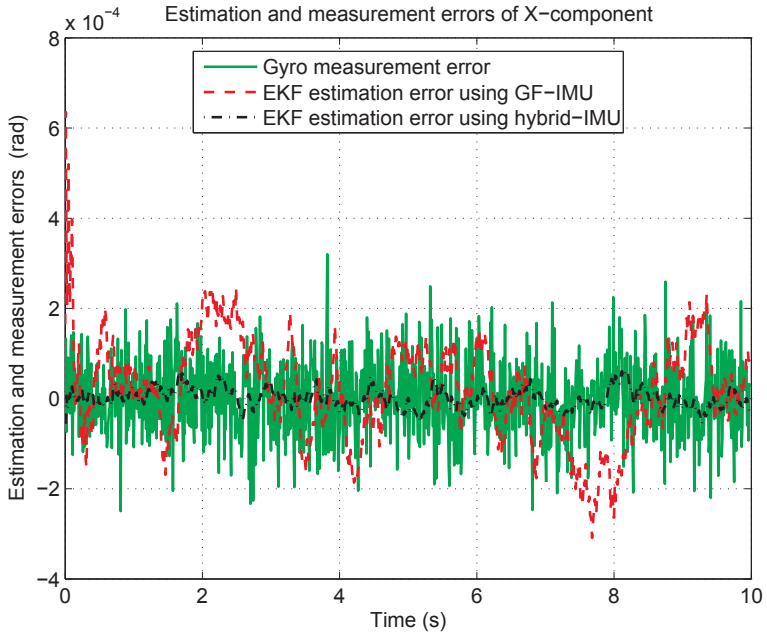

Fig. 4.13 Estimated and measured angular change error in *x* dimension

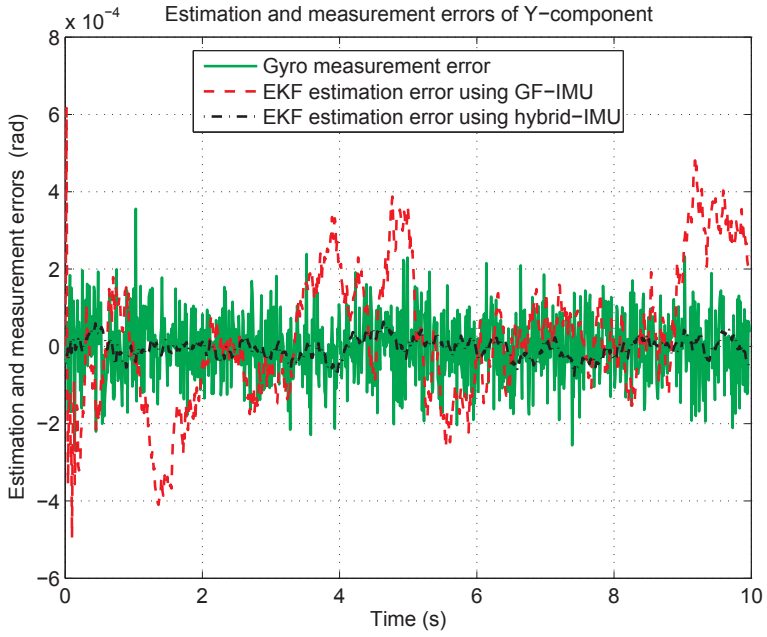

Fig. 4.14 Estimated and measured angular change error in *y* dimension

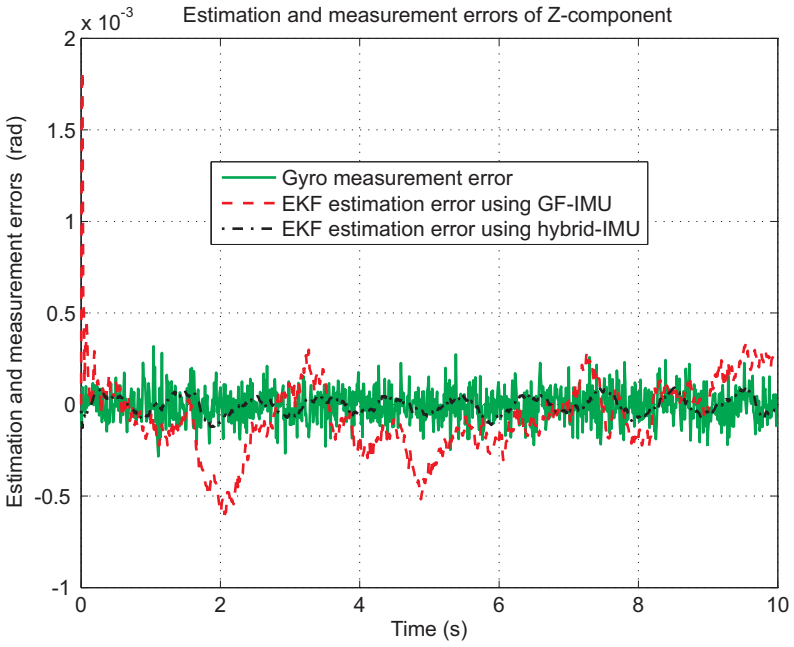

Fig. 4.15 Estimated and measured angular change error in z dimension

From Fig. 4.13 - Fig. 4.15 we notice that the hybrid IMU has a faster convergence than the GF-IMU convergence. The low-cost gyro measurements follow the reference trajectory but with a high level of white noise. In the z component estimation, the hybrid IMU estimation benefited from the angular acceleration coming from GF-IMU hence its performance is much better than GF-IMU estimation. We see the superiority of the hybrid IMU estimation based on the AIV and the gyro measurement vector over the GF-IMU estimation based on the AIV.

4.8 Robustness of the Direct EKF

Not only the low-cost gyros help in the sign convergence, give more accurate estimate and prove smooth convergence but they also give robustness against improper initialization and robustness to detect smaller angular signals that can not be detected by either GF-IMU or low-cost gyros.

4.8.1 Robustness to Small Angular Signal Detection

In this part we reduce the magnitude of the trajectory described in (3.35) to be $\omega_x = 0.0822$ rad/s and $\omega_z = 0.0164$ *rad* / s . Other parameters remain unchanged.

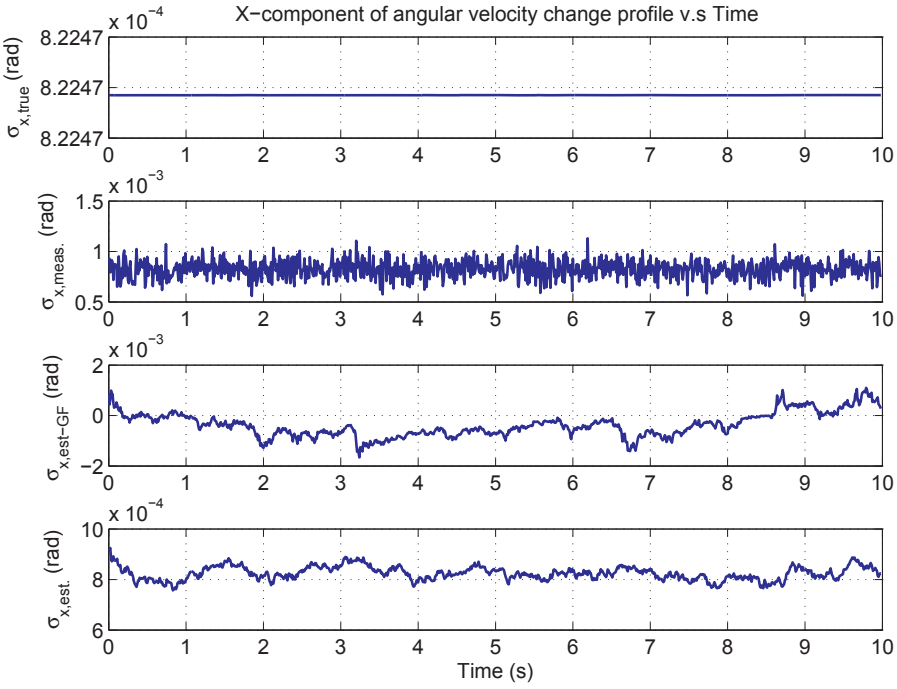

Fig. 4.16 X-component of estimated and measured angular velocity change

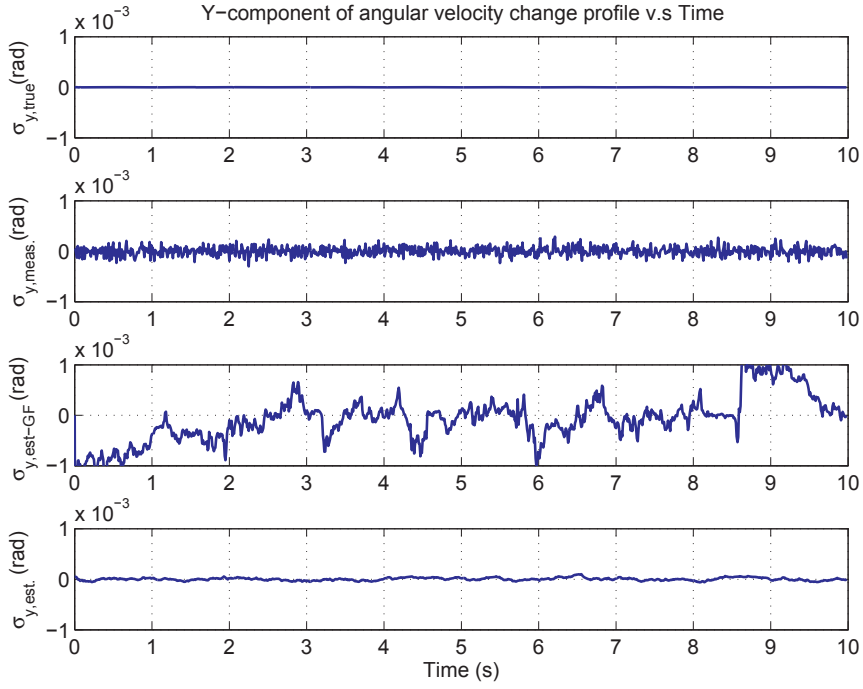

Fig. 4.17 Y-component of estimated and measured angular velocity change

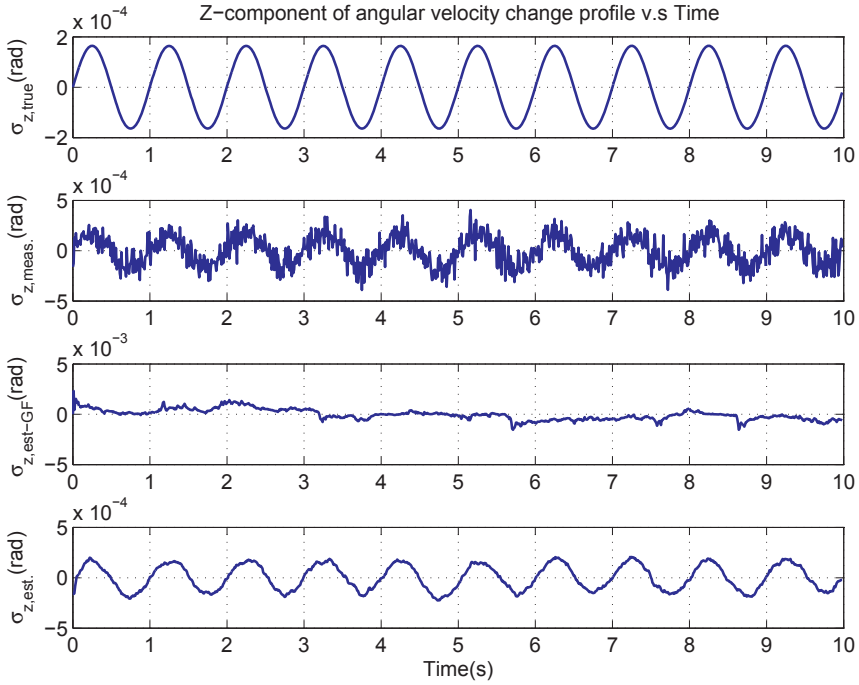

Fig. 4.18 Z-component of estimated and measured angular velocity change

From the previous figures it is clear that the hybrid IMU is more capable of detecting small signals than GF-IMU. Moreover, the estimated angular change of the hybrid IMU is less noisy than the gyro measured output.

4.9 Summary

In this chapter, we presented a novel configuration of fixed distributed accelerometers combined with rotating accelerometers to have direct measurements of the angular velocity. Experimental results show that a rotating accelerometer can be used to find the heading angle after filtering harmonics due to vibration. Also, we presented an EKF model for improving the angular motion knowledge by combining the AIV and the conventional gyro triad measurements. Simulation results show that both types of measurements have complementary nature and hence integration gives the advantage of both. Also, the aid of low-cost traditional gyros is recommended to avoid sign indeterminacy problem and to accelerate convergence smoothly. More complex dynamic models that enable us to estimate the drifting bias parameters in the MEMS gyros can be used.

Chapter 5

Angular Motion Estimation Utilizing Dynamic Models and Constrained Kalman Filtering

In this chapter, we present another novel solution for estimating the angular motion based on the dynamic models in a GF-IMU. During conducting research for the possible filter approaches, we derived nonlinear equality constraints. Hence, we incorporate the constraints in the filter to improve the accuracy of the angular motion estimation, which in turn improves the attitude accuracy.

5.1 AME Using Dynamic Models in a GF-IMU

In this section, we summarize the results of using dynamic models borrowed from tracking theory in describing the evolution of the state space in time to have an estimate of the angular motion in a GF-IMU. Mainly, we use the dynamic models to have the appended bias parameters observable and hence have better angular motion knowledge. Moreover, a good model is useful to extract the maximum amount of information from the observation. Observability analysis is done to determine the conditions for having an observable state vector. For higher grades of accelerometers and under relatively higher sampling frequency, the error of an accelerometer can be dominated by noise error. Consequently, simulation results are given for two models, one with bias parameters appended to the state vector and the other without bias parameters. Bias parameters can be appended to the state space vector if it is desired to be estimated.

5.1.1 Why Do We Need Sophisticated Models?

We developed an integration filter for GF-IMU configurations that consists of twelve mono-axial accelerometers. In our filter design, we used the angular acceleration and the quadratic terms of the angular velocity of the GF-IMU. As a straightforward solution, we have used a direct three state model based on Euler first order integration. The advantage of using such a model is that there is no assumption needs to be made about the dynamics of the motion and hence such a solution fits most scenarios. Though the first order Euler integration model has a simple form, some of the bias parameters, which exist in most of the inertial sensors, will not be observable. Hence, it fits cases where white noise is corrupting accelerometers measurements. The importance of this research is that within a proper dynamic model, the drifting biases can be estimated and hence the quality of the

estimated angular velocity improved greatly. Moreover, any priory information about the motion can be applied in the model to get an improved performance of the AME filter.

5.2 Dynamic Models to Be Considered

In general, a good model is useful to extract the maximum amount of information from the observation. We will utilize the proper dynamic models in the AME in the GF-IMU. We focus on the dynamic models used for maneuvering targets tracking surveyed in [48]. Tracking theory dynamic models are used previously to model the angular acceleration evolution in time [38, 49]. Here, we give a spatial motion extension to the planner motion case given in [38]. The constant angular velocity model makes no use of the measured angular acceleration measurements, so such a model is not a candidate to be considered in our work. Hence, we consider models in which the target angular acceleration that is chosen to be the descriptor of a target maneuvers and modeled as a random process. Next we describe the models that can be used for Kalman filter process update.

5.2.1 Wiener-process Angular Acceleration Model

This model assumes that the angular acceleration is a Wiener process, or more generally and precisely, the angular acceleration is a process with independent increments, which is not necessarily a Wiener process. This model is referred as a constant angular acceleration model (CAA) or a nearly constant angular acceleration model. It can be considered as a special case of a Gauss-Markov process. This model makes the angular acceleration a process with an increasing variance and it is given as

$$\dot{\alpha}(t) = w(t)\,. \tag{5.1}$$

The discrete-time form is given as

$$\alpha_k = \alpha_{k-1} + w_{k-1}\,. \tag{5.2}$$

Since we have time uncorrelated noise, the corresponding state space representation of the Wiener sequence angular acceleration model in 3D motion including angular velocity vector is given as

$$\begin{bmatrix} \underline{\omega}_k \\ \underline{\alpha}_k \end{bmatrix} = \begin{bmatrix} I_{3\times3} & \Delta t I_{3\times3} \\ 0_{3\times3} & I_{3\times3} \end{bmatrix} \begin{bmatrix} \omega_{k-1} \\ \alpha_{k-1} \end{bmatrix} + \begin{bmatrix} \Delta t I_{3\times3} \\ I_{3\times3} \end{bmatrix} \underline{w}_{k-1}\,. \tag{5.3}$$

5.2.2 First-order Markov Model (Singer Angular Acceleration Model)

This model was initially used for modeling linear acceleration [50] and lately used for angular acceleration modeling as given in [49]. It has much wider coverage than a constant angular velocity or constant angular acceleration models. The singer model can be adjusted using the specifications of the

accelerometers used. The Singer model assumes that the target acceleration is a zero-mean stationary first-order Markov process. The time evolution of the angular acceleration in continuous-time is written as

$$\dot{\alpha} = -\beta\alpha + w\,. \tag{5.4}$$

where w is a zero-mean white noise with variance σ_N^2 and β is the reciprocal of the time constant (or reciprocal of correlation time). The discrete-time form of this process is given as

$$\alpha_k = e^{-\beta\Delta t}\alpha_{k-1} + \sigma_\alpha\sqrt{1-e^{-2\beta\Delta t}}\,u_{k-1}\,. \tag{5.5}$$

where u_i is a unit variance samples from a Gaussian random number generator and σ_α is the steady-state variance. Since the correlation time $1/\beta$ is much larger than sampling time Δt, the following approximation is used

$$e^{-\beta\Delta t} \approx 1-\beta\Delta t\,. \tag{5.6}$$

Considering a first order linearization for the exponential term in (5.6), the process can be approximated as

$$\alpha_{k+1} = \left(1-\beta\Delta t\right)\alpha_k + \sqrt{2\beta\Delta t}\,\sigma_\alpha u_k\,. \tag{5.7}$$

The autocorrelation function Ψ_α is exponentially decaying and given as

$$\Psi_\alpha = E\{\alpha(t+\tau)\alpha(t)\} = \sigma_\alpha^2 e^{-\beta|\tau|}\,. \tag{5.8}$$

The corresponding state space representation of the wiener sequence angular acceleration model in 3D motion including angular velocity vector is given as

$$\begin{bmatrix}\underline{\omega}_k\\ \underline{\alpha}_k\end{bmatrix} = \begin{bmatrix} I_{3\times3} & \Delta t I_{3\times3}\\ 0_{3\times3} & \left(1-\beta\Delta t\right)I_{3\times3}\end{bmatrix}\begin{bmatrix}\omega_{k-1}\\ \alpha_{k-1}\end{bmatrix} + \begin{bmatrix}\Delta t I_{3\times3}\\ I_{3\times3}\end{bmatrix}\underline{w}_{k-1}\,. \tag{5.9}$$
$$\underline{w}_{k-1} = \sqrt{2\beta\Delta t}\,\sigma_\alpha\underline{u}_{k-1}$$

The variance is selected according to the ternary-uniform mixture as suggested in [49].

5.2.3 Other Models to Be Considered

Angular jerk which is the derivative of the angular acceleration can be used in the same way we used the angular acceleration based models. Using angular jerk based models increases the dimension of the state space vector which increases the computational load.

5.3 Sensor Error Model and the Measured AIV and Calibration

5.3.1 The Accelerometer Error Model to Be Used

Each accelerometer measurement $\tilde{a}$ is assumed to be corrupted by a bias b_a error component and a continuous-time white noise error component w_{acc}. All accelerometers are assumed to have a common upper bound for the noise variance and bias instability. The discrete-time white noise depends on the square root of the sampling time $\sqrt{\Delta t}$ and it is given as

$$\tilde{a} = a + b_a + w_{acc}\sqrt{\Delta t}/\Delta t . \tag{5.10}$$

The variance of the discrete-time noise component $R_{disc.}$ of each accelerometer measurement of the acceleration is

$$R_{disc.} = E\{w_{acc}^2\}/\Delta t = R_{acc}/\Delta t . \tag{5.11}$$

Every drifting accelerometer bias has the unit of g or its equivalent derivatives and is modeled as random process driven by white noise. The previously described Markov model is used often to model the bias or we can use the simple model of random walk given as

$$\dot{b}_a = w_{ba} . \tag{5.12}$$

In discrete-time the random walk bias model is given as

$$b_{ak} = b_{ak-1} + w_{ba,k-1} . \tag{5.13}$$

Using the accelerometer's error model shown in (5.10), we rewrite the measured AIV with inherited accelerometers errors as

$$\begin{aligned} \dot{\tilde{\omega}}_x &= \dot{\omega}_x + b_1 + w_1 \\ &\vdots \\ \tilde{\omega}_z^2 &= \omega_z^2 + b_9 + w_9 \end{aligned} \tag{5.14}$$

where $b_1..b_9$ represent the new bias parameters and $w_1..w_9$ represent the noise errors.

5.3.2 Capturing the Bias in the AIV

The GF-IMU configuration can be calibrated for exact value distribution distance using a turn table. Assuming the accelerometer's error as described before, we need to calibrate for bias. The bias can be approximated as a nearly constant but slowly varying parameter as it changes with temperature and many other parameters. Initial bias calibration is very easy to be performed since leaving the GF-IMU in a static position means all angular information terms should be zero because the quadratic terms of

Earth's turn rate are extremely small for a small separation distance. Hence, we can find the initial value of the nine bias parameters in the AIV.

5.4 An EKF Solution Using Singer Model with Appending Bias Parameters

Though we have twelve accelerometers and this means we have twelve unknown bias parameters, we are interested in estimating the resulting nine bias parameters $b_1..b_9$ in the AIV given in (5.14). The state vector is composed of the angular velocity vector, the angular acceleration vector and the nine bias parameters given as

$$\begin{aligned} &\underline{x} = \begin{bmatrix} \underline{\omega}^T & \underline{\alpha}^T & \underline{b}_\alpha^T & \underline{b}_{\omega^2}^T \end{bmatrix}^T, \quad \underline{\omega} = \begin{bmatrix} \omega_x & \omega_y & \omega_z \end{bmatrix}^T, \quad \underline{\alpha} = \begin{bmatrix} \dot{\omega}_x & \dot{\omega}_y & \dot{\omega}_z \end{bmatrix}^T \\ &\underline{b}_\alpha = \begin{bmatrix} b_1 & b_2 & b_3 \end{bmatrix}^T, \underline{b}_{\omega^2} = \begin{bmatrix} b_4 & b_5 & b_6 & b_7 & b_8 & b_9 \end{bmatrix}^T \end{aligned} . \tag{5.15}$$

5.4.1 Initialization

The initial state vector and the initial estimate error covariance are set as shown in (3.17) and (3.18).

5.4.2 Prediction

Based on the previously described motion dynamic model and the accelerometer bias model, we can write the discrete-time space model as

$$\begin{aligned} &\begin{bmatrix} \underline{\omega} \\ \underline{\alpha} \\ \underline{b}_\alpha \\ \underline{b}_{\omega^2} \end{bmatrix}_k = \begin{bmatrix} I_{3\times3} & \Delta t I_{3\times3} & 0 & 0 \\ 0 & (1-\beta\Delta t) I_{3\times3} & 0 & 0 \\ 0 & 0 & I_{3\times3} & 0 \\ 0 & 0 & 0 & I_{6\times6} \end{bmatrix} \begin{bmatrix} \underline{\omega} \\ \underline{\alpha} \\ \underline{b}_\alpha \\ \underline{b}_{\omega^2} \end{bmatrix}_{k-1} + \begin{bmatrix} \Delta t I_{3\times3} & 0 & 0 \\ I_{3\times3} & 0 & 0 \\ 0 & I_{3\times3} & 0 \\ 0 & 0 & I_{6\times6} \end{bmatrix} \begin{bmatrix} \underline{w}_\alpha \\ \underline{w}_{b_a} \\ \underline{w}_{b_{\omega^2}} \end{bmatrix}_{k-1} . \\ &\underline{x}_k = F_{k-1}\underline{x}_{k-1} + G_{k-1}\underline{w}_{k-1} \end{aligned} \tag{5.16}$$

The process covariance is computed as

$$Q_{k-1} = G \sum_{k-1} G^T \quad , \ \sum_{k-1} = E\{\underline{w}_{k-1}\underline{w}_{k-1}^T\} . \tag{5.17}$$

The predicted state vector and estimation error covariance are updated as given in the equation set (3.19)-(3.27).

5.4.3 Measurement Update

The AIV that is composed of the angular acceleration vector and six quadratic terms of angular velocity combined with the nine bias parameters given as

$$\underline{h}_k = \begin{bmatrix} x_4 & x_5 & x_6 & x_1x_2 & x_1x_3 & x_2x_3 & x_1^2 & x_2^2 & x_3^2 \end{bmatrix}_k^T + \begin{bmatrix} x_7 & x_8 & x_9 & x_{10} & x_{11} & x_{12} & x_{13} & x_{14} & x_{15} \end{bmatrix}_k^T + \underline{v}_k \tag{5.18}$$

The measurement Jacobian matrix is computed as

$$H_k = \left.\frac{\partial \underline{h}_k(\underline{x},\underline{v})}{\partial \underline{x}}\right|_{x=\hat{x}_k^-} = \begin{bmatrix} 0_{3\times3} & I_{3\times3} & I_{3\times3} & 0_{3\times6} \\ H_{21}^T & 0_{6\times3} & 0_{6\times3} & I_{6\times6} \end{bmatrix}_{x=\hat{x}_k^-}, \; H_{21} = \begin{bmatrix} x_2 & x_3 & 0 & 2x_1 & 0 & 0 \\ x_1 & 0 & x_3 & 0 & 2x_2 & 0 \\ 0 & x_1 & x_2 & 0 & 0 & 2x_3 \end{bmatrix}. \tag{5.19}$$

The measurement error covariance matrix is computed as

$$R_k = \begin{bmatrix} R_\alpha & M \\ M^T & R_{\omega^2} \end{bmatrix}, \; R_{\omega^2} = \left(\frac{R_{disc.}}{d^2}\right) \begin{bmatrix} 1 & \frac{1}{4} & \frac{1}{4} & 0 & 0 & \frac{-1}{2} \\ \frac{1}{4} & 1 & \frac{1}{4} & 0 & \frac{-1}{2} & 0 \\ \frac{1}{4} & \frac{1}{4} & 1 & -\frac{1}{2} & 0 & 0 \\ 0 & 0 & \frac{-1}{2} & \frac{3}{2} & \frac{-1}{2} & \frac{-1}{2} \\ 0 & \frac{-1}{2} & 0 & \frac{-1}{2} & \frac{3}{2} & \frac{-1}{2} \\ \frac{-1}{2} & 0 & 0 & \frac{-1}{2} & \frac{-1}{2} & \frac{3}{2} \end{bmatrix} \tag{5.20}$$

$$R_\alpha = \left(\frac{R_{disc.}}{d^2}\right) \begin{bmatrix} 1 & -1/4 & -1/4 \\ -1/4 & 1 & -1/4 \\ -1/4 & -1/4 & 1 \end{bmatrix}, \; M = \left(\frac{R_{disc.}}{d^2}\right) \begin{bmatrix} \frac{-1}{4} & \frac{1}{4} & 0 & 0 & \frac{-1}{2} & \frac{1}{2} \\ \frac{1}{4} & 0 & \frac{-1}{4} & \frac{1}{2} & 0 & \frac{-1}{2} \\ 0 & \frac{-1}{4} & \frac{1}{4} & \frac{-1}{2} & \frac{1}{2} & 0 \end{bmatrix}.$$

The Kalman gain, the a posteriori estimation error covariance and the a posteriori state estimate are updated as given in the equation set (3.32)-(3.34).

5.5 An EKF Solution Using Singer Model without Appended Bias Parameters

The state vector is reduced to the angular velocity and the angular acceleration vectors and it is given as

$$\underline{x} = \begin{bmatrix} \underline{\omega}^T & \underline{\alpha}^T \end{bmatrix}^T, \quad \underline{\omega} = \begin{bmatrix} \omega_x & \omega_y & \omega_z \end{bmatrix}^T, \quad \underline{\alpha} = \begin{bmatrix} \dot{\omega}_x & \dot{\omega}_y & \dot{\omega}_z \end{bmatrix}^T. \tag{5.21}$$

5.5.1 Initialization

The initial state vector and the initial estimate error covariance are initialized the same way as before in (3.17) and (3.18).

5.5.2 Prediction

Based on the previously described motion dynamic model we write the discrete-time space model as

$$\begin{bmatrix} \underline{\omega}_k \\ \underline{\alpha}_k \end{bmatrix} = \begin{bmatrix} I_{3\times3} & \Delta t I_{3\times3} \\ 0_{3\times3} & (1-\beta\Delta t) I_{3\times3} \end{bmatrix} \begin{bmatrix} \omega_{k-1} \\ \alpha_{k-1} \end{bmatrix} + \begin{bmatrix} \Delta t I_{3\times3} \\ I_{3\times3} \end{bmatrix} \underline{w}_{k-1} . \qquad (5.22)$$
$$\underline{w}_{k-1} = \sqrt{2\beta\Delta t}\,\sigma_\alpha \underline{u}_{k-1}$$

The predicted estimation error covariance and state estimate are updated as in (3.26) and (3.27).

5.5.3 Measurement Update

The AIV that is composed of the angular acceleration vector and six quadratic terms of angular velocity combined given as

$$\underline{h}_k = \begin{bmatrix} x_4 & x_5 & x_6 & x_1x_2 & x_1x_3 & x_2x_3 & x_1^2 & x_2^2 & x_3^2 \end{bmatrix}_k^T + \underline{v}_k . \qquad (5.23)$$

The measurement Jacobian matrix is computed as

$$H_k = \left.\frac{\partial \underline{h}_k(\underline{x},\underline{v})}{\partial \underline{x}}\right|_{x=\hat{x}_k^-} = \begin{bmatrix} 0_{3\times3} & I_{3\times3} \\ H_{21}^T & 0_{6\times3} \end{bmatrix}_{x=\hat{x}_k^-}, \; H_{21} = \begin{bmatrix} x_2 & x_3 & 0 & 2x_1 & 0 & 0 \\ x_1 & 0 & x_3 & 0 & 2x_2 & 0 \\ 0 & x_1 & x_2 & 0 & 0 & 2x_3 \end{bmatrix}. \qquad (5.24)$$

The Kalman gain, the a posteriori estimation error covariance and the a posteriori state estimate are updated as given in the equation set (3.32)-(3.34).

5.6 Observability Analysis

Using the dynamic model gives us the possibility to have all the bias parameters in the resulting angular terms observable under some conditions. In this section, we determine under which conditions is the state space observable. First, we remove the noise in this observability analysis which leaves us with the simpler homogeneous state- space system

$$\begin{aligned} \dot{\underline{x}} &= A\underline{x} \\ \underline{y} &= \underline{h}(\underline{x}) \end{aligned} . \qquad (5.25)$$

We follow the local observability test based on Lie derivatives [51] which is used in [38] for the one dimensional angular motion. We compute L which denotes the set of all finite linear combinations of

Lie derivatives of the measurement vector with respect to f for various values of constant input.

$$L_f^0(h_i) = h_i \,. \tag{5.26}$$

Higher order Lie derivatives are computed as

$$L_f^k(h_i) = h_i^k \,. \tag{5.27}$$

For our model which has *n* states, the higher order Lie derivatives starting from the third derivative are entirely zero vectors as shown next

$$\underline{h} = \begin{bmatrix} x_4 + x_7 \\ x_5 + x_8 \\ x_6 + x_9 \\ x_1x_2 + x_{10} \\ x_1x_3 + x_{11} \\ x_2x_3 + x_{12} \\ x_1^2 + x_{13} \\ x_2^2 + x_{14} \\ x_3^2 + x_{15} \end{bmatrix}, \dot{\underline{h}} = \begin{bmatrix} 0 \\ 0 \\ 0 \\ x_2x_4 + x_1x_5 \\ x_3x_4 + x_1x_6 \\ x_3x_5 + x_2x_6 \\ 2x_1x_4 \\ 2x_2x_5 \\ 2x_3x_6 \end{bmatrix}, \ddot{\underline{h}} = \begin{bmatrix} 0 \\ 0 \\ 0 \\ 2x_4x_5 \\ 2x_4x_6 \\ 2x_5x_6 \\ 2x_4^2 \\ 2x_5^2 \\ 2x_6^2 \end{bmatrix}, \dddot{\underline{h}} = \begin{bmatrix} 0 \\ 0 \\ 0 \\ 0 \\ 0 \\ 0 \\ 0 \\ 0 \\ 0 \end{bmatrix}, ..., \underline{h}^{n-1} = \begin{bmatrix} 0 \\ 0 \\ 0 \\ 0 \\ 0 \\ 0 \\ 0 \\ 0 \\ 0 \end{bmatrix}. \tag{5.28}$$

The system is observable if the observability matrix O, defined next, has a rank of 15. The observability matrix is defined as

$$\mathrm{O}(x_0, u) = \begin{bmatrix} dL_f^0(h_1) \\ \vdots \\ dL_f^0(h_p) \\ \vdots \\ dL_f^{n-1}(h_1) \\ \vdots \\ dL_f^{n-1}(h_p) \end{bmatrix}. \tag{5.29}$$

where p is the number of measurements. In our case, we have nine measurements and fifteen states so the dimension of the observability matrix is 135x15. After removing the zero rows we get the following matrix with independent rows

$$\mathrm{O}_{red.}=\begin{bmatrix}\mathrm{O}_{11} & I_{9\times 9}\\ \mathrm{O}_{21} & 0_{6\times 9}\\ \mathrm{O}_{31} & 0_{6\times 9}\end{bmatrix},\ \mathrm{O}_{11}=\begin{bmatrix}0_{3\times 3} & I_{3\times 3}\\ \mathrm{O}_{211} & 0_{6\times 3}\end{bmatrix},\ \mathrm{O}_{211}=\begin{bmatrix}x_2 & x_1 & 0\\ x_3 & 0 & x_1\\ 0 & x_3 & x_2\\ 2x_1 & 0 & 0\\ 0 & 2x_2 & 0\\ 0 & 0 & 2x_3\end{bmatrix}$$

$$\mathrm{O}_{21}=\begin{bmatrix}x_5 & x_4 & 0 & x_2 & x_1 & 0\\ x_6 & 0 & x_4 & x_3 & 0 & x_1\\ 0 & x_6 & x_5 & 0 & x_3 & x_2\\ 2x_4 & 0 & 0 & 2x_1 & 0 & 0\\ 0 & 2x_5 & 0 & 0 & 2x_2 & 0\\ 0 & 0 & 2x_6 & 0 & 0 & 2x_3\end{bmatrix},\ \mathrm{O}_{31}=\begin{bmatrix}0 & 0 & 0 & 2x_5 & 2x_4 & 0\\ 0 & 0 & 0 & 2x_6 & 0 & 2x_4\\ 0 & 0 & 0 & 0 & 2x_6 & 2x_5\\ 0 & 0 & 0 & 4x_4 & 0 & 0\\ 0 & 0 & 0 & 0 & 4x_5 & 0\\ 0 & 0 & 0 & 0 & 0 & 4x_6\end{bmatrix}. \tag{5.30}$$

Therefore, the condition to have an observable state space model is that the angular acceleration vector has at least one nonzero component in any of the three dimensions of motion or in other words the magnitude of the angular acceleration has a nonzero value.

5.7 Simulation Results for the Augmented Model

We consider a sinusoidal trajectory which is considered often in literature [2, 38, 49]. Moreover, such a trajectory satisfies the observability condition of a nonzero angular acceleration.

5.7.1 Trajectory Profile and Parameters Setting

In two dimensions we have a harmonic angular oscillation and in the third dimension we assume no angular motion. The mathematical description of the angular motion is given as

$$\underline{\omega}(t)=\omega_m \sin(2\pi ft)[1\quad 1\quad 0]^T. \tag{5.31}$$

$$\underline{\alpha}(t)=2\pi f\omega_m \cos(2\pi ft)[1\quad 1\quad 0]^T. \tag{5.32}$$

For a practical value of the accelerometer's noise and bias levels, we consider the specifications of the accelerometers manufactured by Analog devices. We want to have a portable IMU so we choose the separation distance to be 0.4 m. The duration time T of the experiment is 20 seconds.

Table 5.1 Numerical values of the simulation parameters

Parameter (Unit)	ω_m (rad/s)	f (Hz)	Δt (s)	$w_{acc.}$ ($\mathrm{g}/\sqrt{\mathrm{Hz}}$)	$bias$ (g)	d (m)	T (s)
Value	0.4112	0.5	0.01	200 µ	2400 µ	0.4	20

The state vector is initialized properly around the true state with initial state error of 5% of the true value. The bias values were selected randomly from a distribution with 1 standard deviation of $2400\,\mu g$ as shown in Fig. 5.1 and Fig. 5.2 show plots of the angular velocity and the angular acceleration profiles respectively.

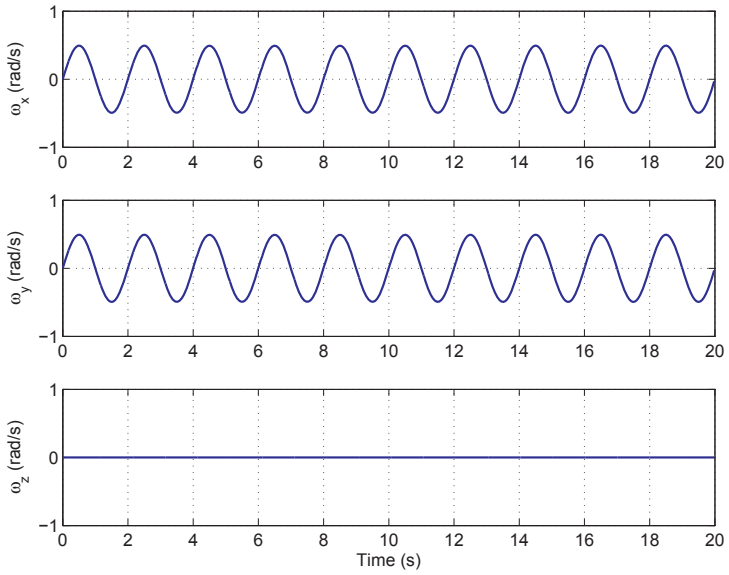

Fig. 5.1 Angular velocity trajectory profile

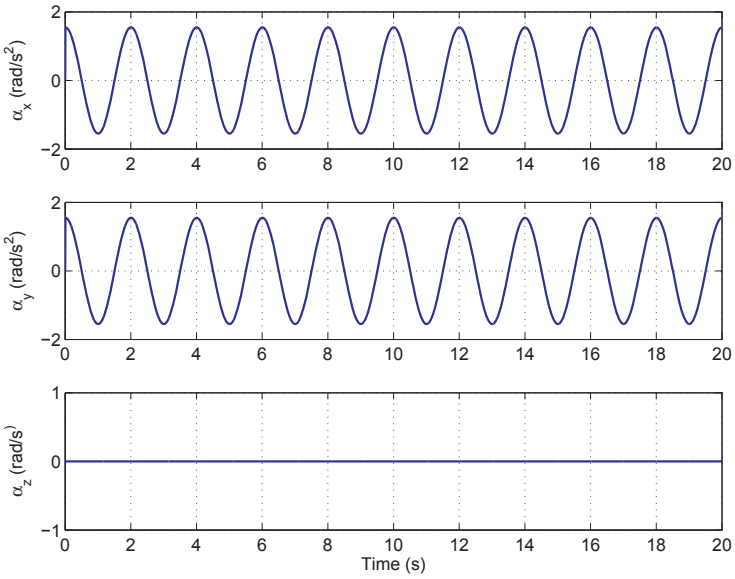

Fig. 5.2 Angular acceleration trajectory profile

5.7.2 Results and Analysis

Errors in the estimated angular velocity and the estimated angular acceleration vectors are plotted next in Fig. 5.3 and Fig. 5.4 respectively.

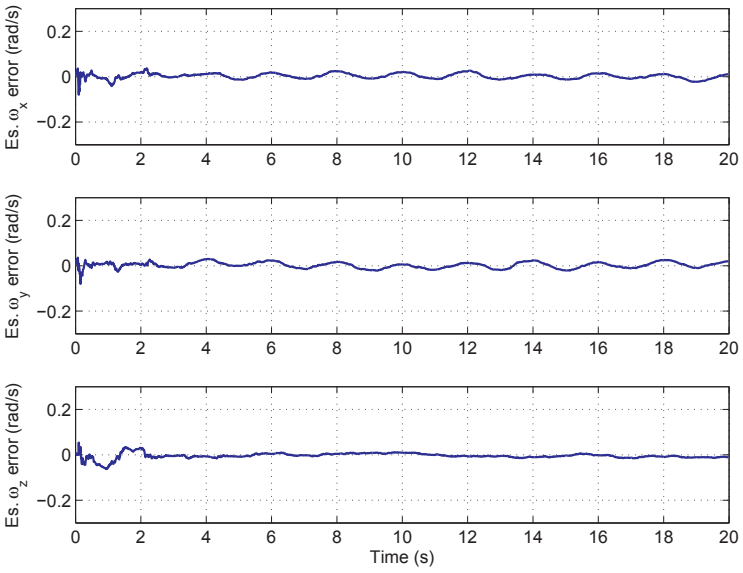

Fig. 5.3 Angular velocity estimation error

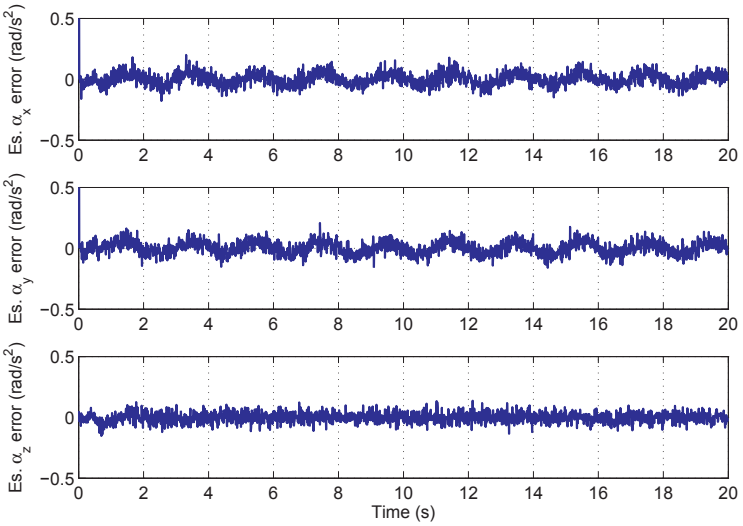

Fig. 5.4 Angular acceleration estimation error

Clearly, we see a good convergence to the true angular velocity and angular acceleration. We see a small swing in the x and y components of the angular velocity and angular acceleration. This is

because we model the angular acceleration as random process driven by white noise while the true trajectory is sinusoidal one. From simulations, the magnitude of this swing increases as the frequency of oscillation of the trajectory increases and decreases incase of low frequency oscillation. So the CAA and the Markov model are not suitable for high dynamic oscillations. The estimation errors in the nine bias parameters are shown in Fig. 5.5 next.

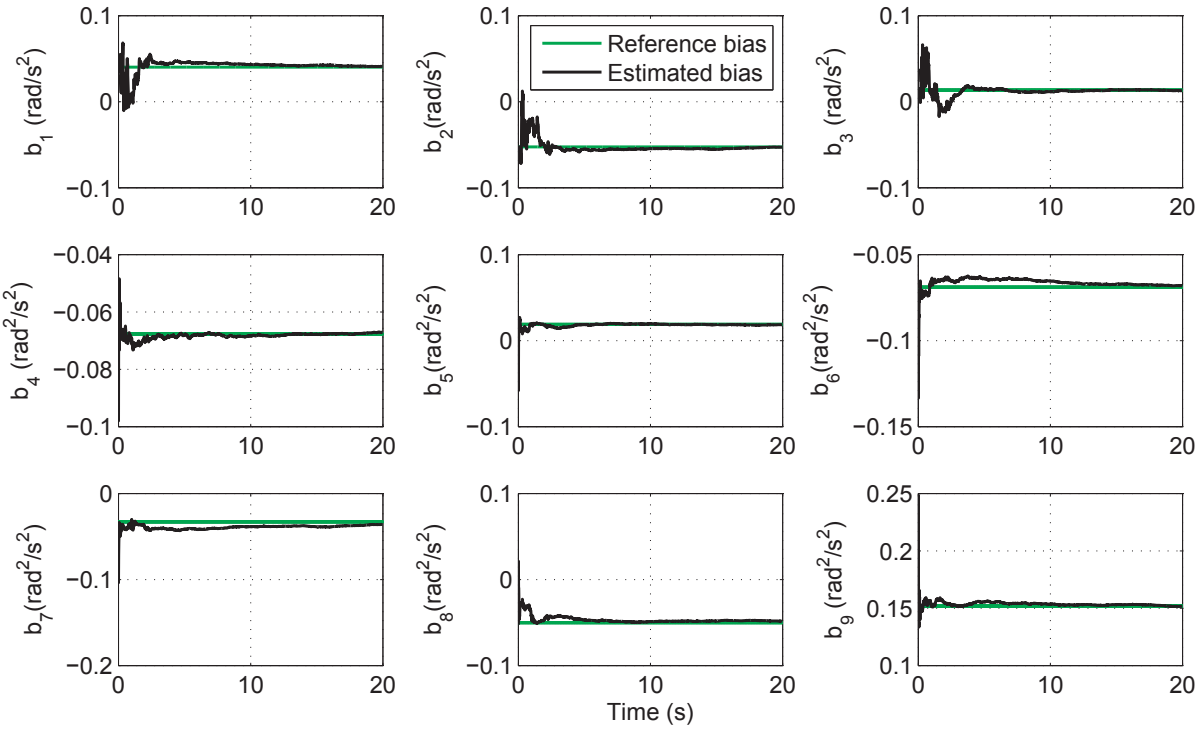

Fig. 5.5 Estimated and reference bias parameters in the AIV

The plots show the convergence of all estimated bias parameters in the AIV to their exact value with small steady state error. Moreover, from extensive simulations we find that reducing the noise error level of in accelerometers gives a smoother and a faster convergence of bias.

5.7.3 Effect of Improper Initialization

Since we use an EKF form which is a linearization of the Kalman filter, the proper initialization of the state vector is important to avoid filter divergence. However, limited level of initialization error can be tolerated by the filter because the nonlinearity is not high. If no information is available about bias parameters in the AIV from calibration process, the bias parameters can be initialized with a zero vector. Simulations show that the filter converges without problems but after larger time for the

previously mentioned bias stability. We show next in Fig. 5.6 and Fig. 5.7 the plots of the errors in the estimated angular velocity and acceleration vectors for the improper initialization case.

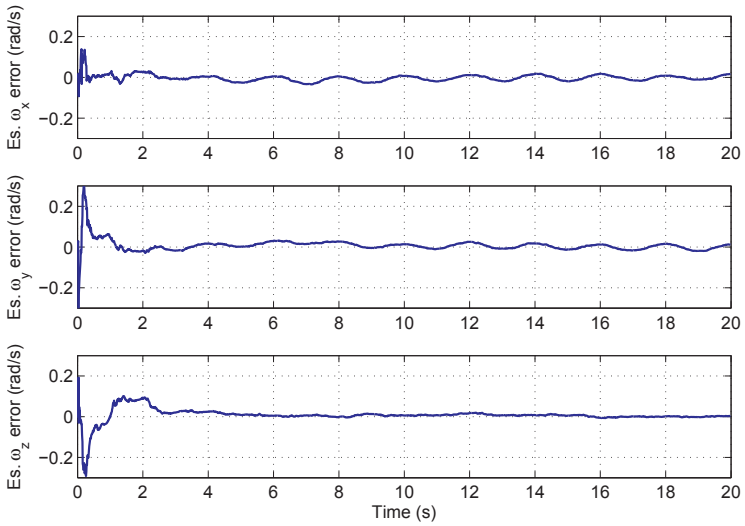

Fig. 5.6 Angular velocity estimation error with initialization error

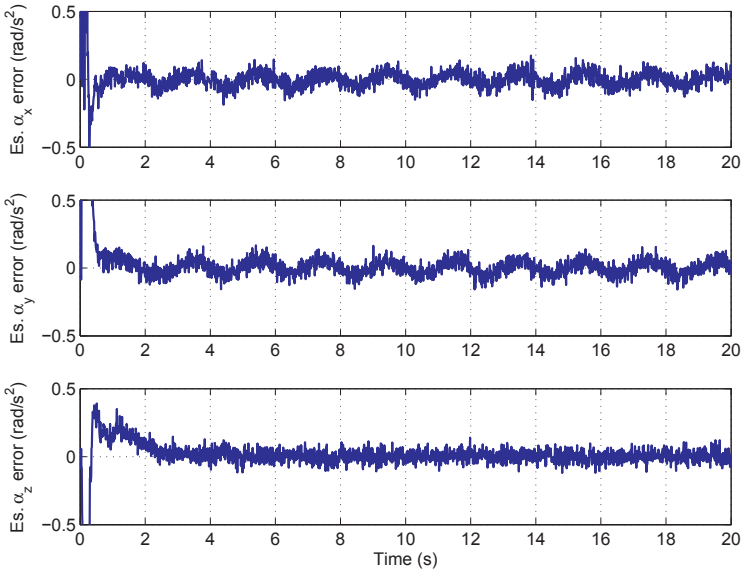

Fig. 5.7 Angular acceleration estimation error with initialization error

5.8 Simulation Results for Non-Augmented Model

In this part of simulations, we consider the same trajectory described previously but with bias parameters non-appended to the state vector which means we simply ignore them. The condition for ignoring bias parameters is explained previously in subsection 3.6.2.

5.8.1 Trajectory Profile and Parameter Setting

We repeat the previously used trajectory profile with same settings except for the noise and bias levels which are set to $w_{acc.} = 100\ \mu g/\sqrt{\text{Hz}}$ and the bias selected randomly from distribution with 1 standard deviation of $100\ \mu g$. The chosen accelerometer specifications satisfy the criteria that the error is dominated by white noise error at the selected sampling rate of 0.01 s.

5.8.2 Results and Analysis

First, the execution time was much smaller than the previous model which has bias parameters appended because we have much simpler state model. Using a reduced model implies reducing computation load remarkably. The plots of errors in the estimated angular velocity and the estimated angular acceleration vectors are shown in Fig. 5.8 and Fig. 5.9 respectively. From figures we see a fast convergence to the true profile of angular velocity and angular acceleration. Again, we see a small swing in the x and y components of the angular velocity and the angular acceleration which is explained previously in section 5.7.2.

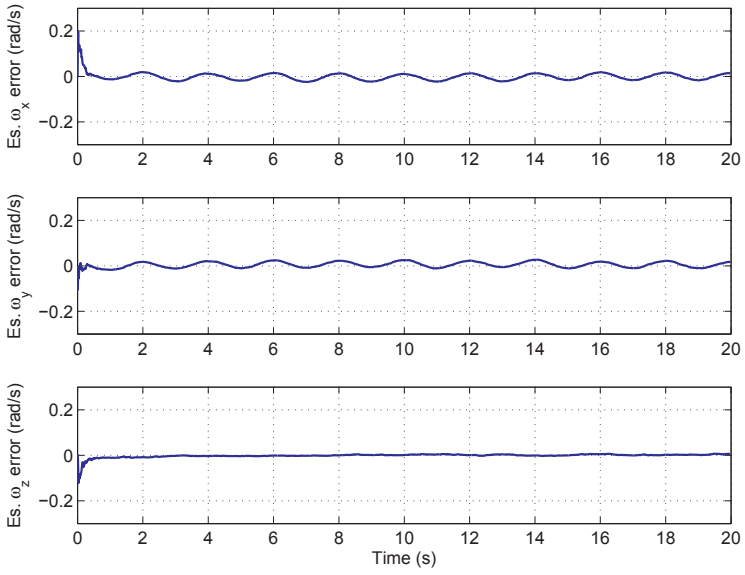

Fig. 5.8 Angular velocity estimation error for reduced model

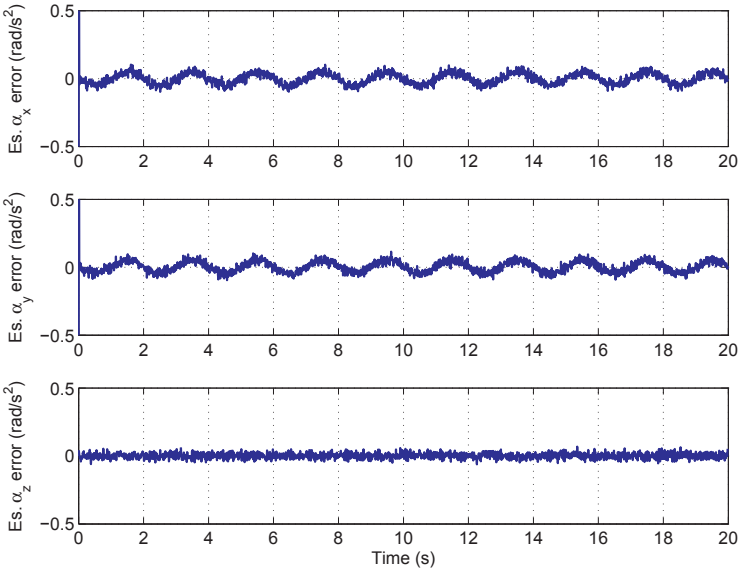

Fig. 5.9 Angular acceleration estimation error for reduced model

To see the effect of ignoring higher bias values, we repeated the simulation with the same parameter values used in section 5.8 and created a plot of the estimated angular velocity. Such parameter values do not meet the criteria that accelerometer's error is dominated by white noise error and hence this results in a biased estimate of the angular velocity as shown in Fig. 5.10.

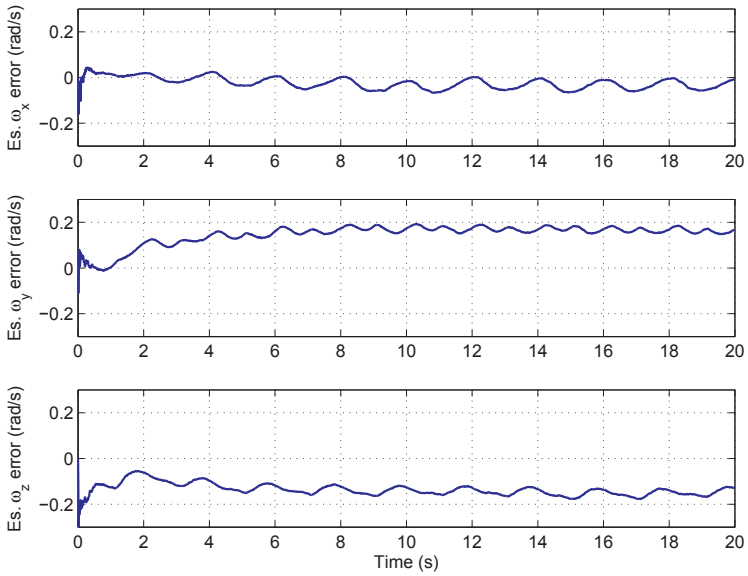

Fig. 5.10 Angular velocity estimation error for reduced model with non-calibrated bias

5.9 Constraints Derivation

In this section, we derive the equality constraints that exist in the model because of orthogonal accelerations. For a non-coning motion, the centripetal acceleration vector $\underline{\omega}_{ib}^{b} \times \underline{\omega}_{ib}^{b} \times \underline{p}^{b}$ and the tangential acceleration vector $\underline{\dot{\omega}}_{ib}^{b} \times \underline{p}^{b}$ in (3.3) are orthogonal. The two vectors are represented as

$$\underline{a}_c = \begin{bmatrix} -(\omega_y^2 + \omega_z^2)p_x + \omega_x\omega_y p_y + \omega_x\omega_z p_z \\ \omega_x\omega_y p_x - (\omega_z^2 + \omega_x^2)p_y + \omega_y\omega_z p_z \\ \omega_x\omega_z p_x + \omega_y\omega_z p_y - (\omega_x^2 + \omega_y^2)p_z \end{bmatrix} \tag{5.33}$$

$$\underline{a}_t = \begin{bmatrix} -\dot{\omega}_z p_y + \dot{\omega}_y p_z \\ \dot{\omega}_z p_x - \dot{\omega}_x p_z \\ -\dot{\omega}_y p_x + \dot{\omega}_x p_y \end{bmatrix}. \tag{5.34}$$

We use three vectors as basis set that spans all possible distributed positions

$$\begin{bmatrix} p_x \\ p_y \\ p_z \end{bmatrix} \in \left\{ \begin{bmatrix} 1 \\ 0 \\ 0 \end{bmatrix}, \begin{bmatrix} 0 \\ 1 \\ 0 \end{bmatrix}, \begin{bmatrix} 0 \\ 0 \\ 1 \end{bmatrix} \right\}. \tag{5.35}$$

Applying inner product on (5.33) and (5.34) with three different values of $\begin{bmatrix} p_x & p_y & p_z \end{bmatrix}^T$ as given in (5.35), produces the following set of equations

$$\begin{bmatrix} -(\omega_y^2 + \omega_z^2) \\ \omega_x\omega_y \\ \omega_x\omega_z \end{bmatrix} \odot \begin{bmatrix} 0 \\ \dot{\omega}_z \\ -\dot{\omega}_y \end{bmatrix} = 0 \tag{5.36}$$

$$\begin{bmatrix} \omega_x\omega_y \\ -(\omega_z^2 + \omega_x^2) \\ \omega_y\omega_z \end{bmatrix} \odot \begin{bmatrix} -\dot{\omega}_z \\ 0 \\ \dot{\omega}_x \end{bmatrix} = 0 \tag{5.37}$$

$$\begin{bmatrix} \omega_x\omega_z \\ \omega_y\omega_z \\ -(\omega_x^2 + \omega_y^2) \end{bmatrix} \odot \begin{bmatrix} \dot{\omega}_y \\ -\dot{\omega}_x \\ 0 \end{bmatrix} = 0. \tag{5.38}$$

After computing the inner product on the above vectors, we get the following equations

$$\begin{aligned}
&\omega_x\omega_y\dot{\omega}_z - \omega_x\omega_z\dot{\omega}_y = 0 \\
&\omega_y\omega_z\dot{\omega}_x - \omega_x\omega_y\dot{\omega}_z = 0 \\
&\omega_x\omega_z\dot{\omega}_y - \omega_y\omega_z\dot{\omega}_x = 0
\end{aligned} . \tag{5.39}$$

The last constraint is dependent on the first two. Therefore, the remaining two independent constraints are

$$\begin{aligned}
&\omega_x\omega_y\dot{\omega}_z - \omega_x\omega_z\dot{\omega}_y = 0 \\
&\omega_y\omega_z\dot{\omega}_x - \omega_x\omega_y\dot{\omega}_z = 0
\end{aligned} . \tag{5.40}$$

5.10 Constrained EKF

We derived two constraints that need to be integrated within the EKF algorithm. The constraints equations shown in (5.40) contain angular acceleration components. The derivation of the angular acceleration vector from angular velocity vector by differentiation would give a noisy value hence we append the angular acceleration to the state vector. Moreover, the derivation of the Jacobian of the constraints will be much easier. Using the angular change vector augmented with angular velocity change vector as a state vector, results in the following state vector

$$\underline{x} = \begin{bmatrix} x_1 & .. & x_6 \end{bmatrix}^T = \begin{bmatrix} \sigma_x & \sigma_y & \sigma_z & \alpha_x & \alpha_y & \alpha_z \end{bmatrix}^T . \tag{5.41}$$

5.10.1 Initialization

The initial state vector and the initial estimate error covariance are set as shown in (3.17), (3.18).

5.10.2 Prediction

We use a nearly constant angular velocity change state-space model, which is also known as Wiener-sequence model, for the process update. It assumes that the angular velocity change increment is an independent (white noise) process. Other sophisticated models for target dynamics, which can be used for process update, are surveyed in [52]. As discussed previously using this model, we can estimate the bias parameters in the AIV when they are appended to the state vector. This model is expressed in discrete-time as

$$\begin{aligned}
&\underline{x}_k = F'_{k-1}\underline{x}_{k-1} + G'_{k-1}\underline{w}_{k-1} \\
&F'_{k-1} = \begin{bmatrix} I_{3\times3} & \Delta t I_{3\times3} \\ 0_{3\times3} & I_{3\times3} \end{bmatrix},\ G'_{k-1} = \begin{bmatrix} \Delta t I_{3\times3} \\ I_{3\times3} \end{bmatrix}.
\end{aligned} \tag{5.42}$$

This process noise covariance is computed as

$$Q'_{k-1} = G'_{k-1}\,\mathrm{cov}(\underline{w}_{k-1})G'^{T}_{k-1}\,. \tag{5.43}$$

The a priori estimation error covariance is updated as

$$P_k^- = F'_{k-1}P^+_{k-1}F'^{T}_{k-1} + Q'_{k-1}\,. \tag{5.44}$$

The a priori state estimate is updated as

$$\underline{\hat{x}}_k^- = F'_{k-1}\underline{\hat{x}}^+_{k-1}\,. \tag{5.45}$$

5.10.3 Measurement Update

The whole AIV given in (3.8) - (3.10) is used to derive the measurement of the new state vector. Considering the existence of a white Gaussian noise in each accelerometer measurement, the observation inherits also white Gaussian noise $\underline{v}$ vector and it is written as

$$y'_k = \underline{h}'_k(\underline{x},\underline{v}) = \begin{bmatrix} x_4 & x_5 & x_6 & x_1x_2 & x_1x_3 & x_2x_3 & x_1^2 & x_2^2 & x_3^2 \end{bmatrix}^T_k + \begin{bmatrix} v_1 & .. & v_9 \end{bmatrix}^T_k\,. \tag{5.46}$$

The Jacobian of the new measurement model H'_k is expressed in terms of the Jacobian of three-state model H given in (3.29) as

$$H'_k = \left.\frac{\partial \underline{h}'_k(\underline{x},\underline{v})}{\partial \underline{x}}\right|_{x=\hat{x}_k^-} = \begin{bmatrix} 0_{3\times3} & I_{3\times3} \\ H & 0_{6\times3} \end{bmatrix}_{x=\hat{x}_k^-}\,. \tag{5.47}$$

The measurement covariance R'_k of the new model is computed based on the previously derived measurement covariance R_k, cross correlated covariance M_k and covariance Q_{k-1} of the three-state model

$$R'_k = \begin{bmatrix} Q_{k-1}/(\Delta t)^2 & M_k/\Delta t \\ M_k^T/\Delta t & R_k \end{bmatrix}. \tag{5.48}$$

The Kalman gain is updated as

$$K_k = P_k^- H'^{T}_k (H'_k P_k^- H'^{T}_k + R'_k)^{-1}\,. \tag{5.49}$$

The a posteriori estimation error covariance and the a posteriori state estimate are updated as given in (3.33)-(3.34).

5.10.4 Handling of the Nonlinear Equality Constraints

There are many approaches for handling equality constraints in the Kalman filtering literature. Common approaches include pseudo measurement, projection and model reduction approaches. Due to the nonlinearity of the constraints, model reduction is not applicable in our system. In the pseudomeasurement approach, also known as pseudo-observation approach, each nonlinear constraint

is modeled as an observation with additive white Gaussian noise to relax the rigidity of the constraints. An example of that approach for the use of kinematic constraint is described in [53] with the decreasing covariance rationale which was introduced to relax the rigidity of the constraints. In projection approach, the unconstrained estimate is projected onto the constraints surface as developed by Simon [54] or using its second order nonlinear extension [55]. The UKF, which has proven to be superior to the EKF in case of significant nonlinearities, can be also applied to incorporate nonlinear constraints to achieve a better estimation performance either using pseudomeasurement approach or projection function [56]. However, we choose an algorithm, which might be computationally less demanding compared with other algorithms. In our simulations, we use the smoothly constrained Kalman filter (SCKF) developed by Geeter for applying nonlinear constraints because nonlinear constraints are different from linear constraints due to truncation and base point errors resulting from EKF linearization [56, 57]. Essentially the SCKF algorithm is classified as a pseudomeasurement approach combined with the iterated extended Kalman filter (IEKF), which iteratively applies nonlinear observations to reduce truncation errors. In every time step, each constraint is linearized with the last available estimate and applied iteratively with exponentially decreasing uncertainty. The smooth application of constraints is motivated by the fact that applying a measurement of variance ζ is equivalent to applying the same measurement k times each with variance $k\zeta$. The equality constraints function and its Jacobian matrix, considering the new state vector, are derived from (5.40) as

$$\underline{e}_c(\underline{x}) = \begin{bmatrix} x_1x_2x_6 - x_1x_3x_5 \\ x_2x_3x_4 - x_1x_2x_6 \end{bmatrix} = \underline{0}\ ,\ \mathrm{E}_c = \frac{\partial \underline{e}_c(\underline{x})}{\partial \underline{x}} = \begin{bmatrix} x_2x_6 - x_3x_5 & x_1x_6 & -x_1x_5 & 0 & -x_1x_3 & x_1x_2 \\ -x_2x_6 & x_3x_4 - x_1x_6 & x_2x_4 & x_2x_3 & 0 & -x_1x_2 \end{bmatrix}. \tag{5.50}$$

The following algorithm summarizes how to incorporate the constraints after measurement update using the SCKF

$$
\begin{aligned}
&\underline{\hat{x}} = \underline{\hat{x}}_k^+, \quad P = P_k^+ \\
&\text{for } c = 1,2 \\
&\{i = 0,\ e(\underline{x}) = row_c(\underline{e}_c(\underline{x}))\ ,\ E = row_c(E_c)\big|_{\underline{\hat{x}}} \\
&\zeta_0 = \gamma EPE^T,\ s = \max_j(E_j P_{jj} E_j)\big/EPE^T \\
&\text{while}(s < s_{th}) \\
&\{\zeta_c = \zeta_0 e^{-i},\ E = row_c(E_c)\big|_{\underline{\hat{x}}} \\
&K = (PE^T)(EPE^T + \zeta_c)^{-1} \\
&\underline{\hat{x}} = \underline{\hat{x}} - Ke(\underline{\hat{x}}) \\
&P = (I_{6\times 6} - KE)P \\
&i = i + 1 \\
&s = \max_j(E_j P_{jj} E_j)\big/EPE^T \\
&\} \text{ end while } \} \text{ end for} \\
&\underline{\hat{x}}_k^+ = \underline{\hat{x}},\quad P_k^+ = P
\end{aligned}
\tag{5.51}
$$

The function row_c finds the *c*-th row of $\underline{e}_c(\underline{x})$ and E_c to apply constraints sequentially. The value of the fraction factor γ for the initial variance needs to be verified by simulations. The relative strength s compares the variance in the denominator, which is a sum of terms, to one of the largest terms forming that variance. The symbol s_{th} is a termination criterion for the application of constraints, which Geeter sets to be $s_{th} = 100$ as a practical value. To avoid any convergence problems, we should apply those constraints after sufficiently applying the observations. For rapidly changing angular velocity profile it would be difficult to estimate the angular velocity change, consequently in such situations the constraints are not applied.

5.11 EKF Constrained Model Simulation Results and Analysis

A similar setup to the one described in section 3.6 is repeated here for the constrained model. In the following plots, we compare the performance of the EKF constrained model with the EKF unconstrained model. We choose a constant angular velocity trajectory and we set the separation distance *d* to 1 m. The angular velocity vector is given as

$$\underline{\omega}(t) = \omega[1 \quad 1 \quad 1]^T . \tag{5.52}$$

The angular velocity along each component is set to $\omega = 3.29$ rad/s . Three levels of white noise error are considered in the simulation, namely tactical, automotive and consumer grade as categorized as shown in Table 5.2. We evaluate the improvement in the estimation performance by computing the

root mean square error (RMSE) over Monte Carlo runs. Clearly, there will be an improvement due to the use of the dynamic model over the three-state model.

Table 5.2 Accelerometers Categories

Performance Parameter	Consumer	Automotive	Tactical
Noise Floor VRW ($\mu g/\sqrt{Hz}$)	2000	1000	500

The RMSE is computed over 500 Monte Carlo runs. Due to space limitations, we show here the simulation results in Fig. 5.11 - Fig. 5.14 using tactical accelerometers category only. We applied the constraints directly after passing 10 seconds to distinguish between the improvement due to use of dynamic model and the improvement due to the application of constraints. The RMSE of the angular change components and the angular change vector are tabulated in Table 5.3 for the three categories of accelerometers.

Table 5.3 Comparison of steady state RMSE for different accelerometers categories

D=1 m	Tactical Grade		Automotive Grade		Consumer Grade	
Model	Unconstrained	Constrained	Unconstrained	Constrained	Unconstrained	Constrained
Term						
$\underline{\sigma}\ [rad]$	4.09×10^{-5}	8.54×10^{-6}	8.44×10^{-5}	1.47×10^{-5}	1.66×10^{-4}	2.64×10^{-5}
$\sigma_x\ [rad]$	2.38×10^{-5}	4.97×10^{-6}	4.74×10^{-5}	8.17×10^{-6}	9.94×10^{-5}	1.55×10^{-5}
$\sigma_y\ [rad]$	2.29×10^{-5}	4.87×10^{-6}	4.84×10^{-5}	8.53×10^{-6}	9.32×10^{-5}	1.50×10^{-5}
$\sigma_z\ [rad]$	2.41×10^{-5}	4.95×10^{-6}	5.04×10^{-5}	8.74×10^{-6}	9.42×10^{-5}	1.52×10^{-5}

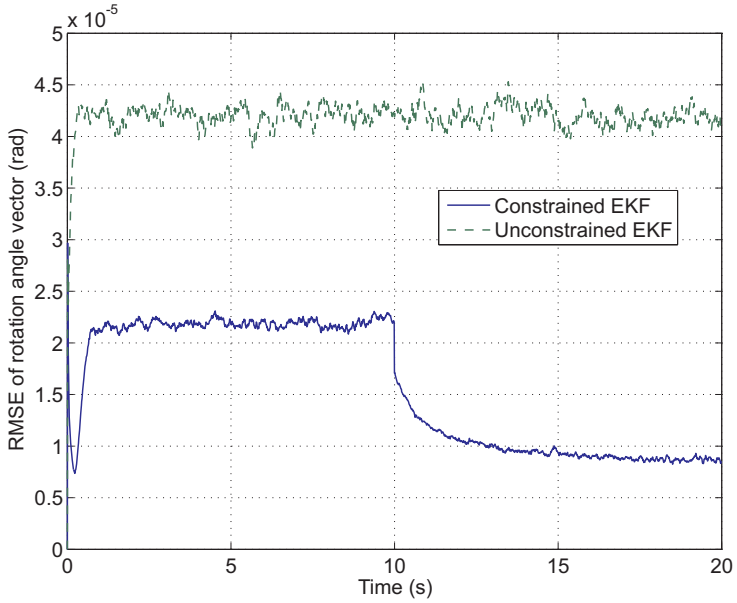

Fig. 5.11 RMSE of angular change vector

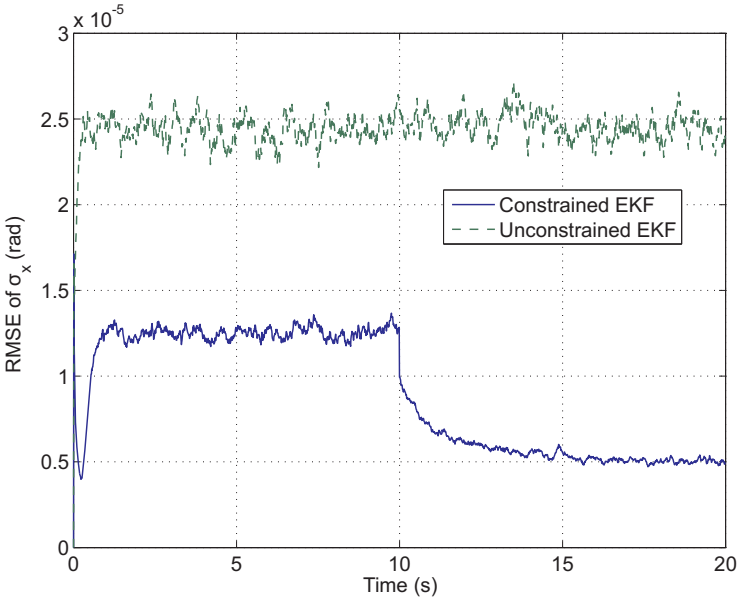

Fig. 5.12 RMSE of σ_x

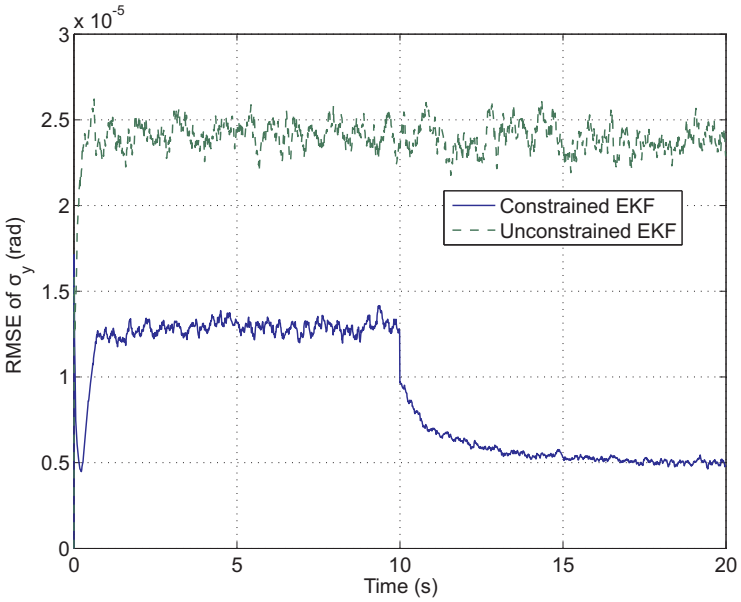

Fig. 5.13 RMSE of σ_y

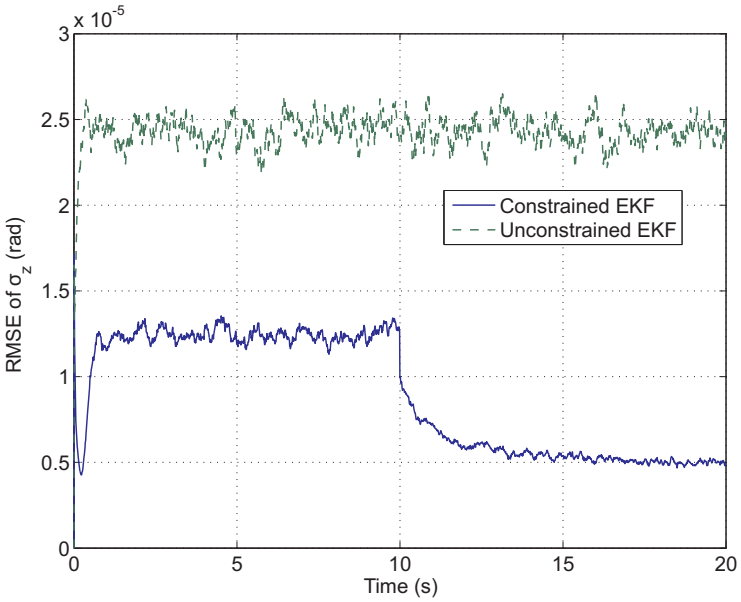

Fig. 5.14 RMSE of σ_z

For all categories of accelerometers, there was a clear superiority of the constrained model over three-state model in the steady state RMSE and this superiority increases after applying the constraints. Typically, we should have a similar improvement reflected in the RMSE of each estimated angular change component due to the symmetry of the GF-IMU configuration, equal signal input in 3D

components and symmetry of the constraints. The simulation results are in agreement with that.

5.12 Summary

In this chapter, we presented another approach for AME utilizing dynamic models in 3D which is capable of estimating bias parameters in the AIV in the GF-IMU. Observability analysis shows that the state space model with appended AIV bias parameters is observable whenever the angular acceleration vector has non-zero magnitude. Simulation results show the filter ability to track the bias parameters in the AIV. Moreover, we derived nonlinear equality constraints and presented a filter approach to benefit from the constraints in improving estimation performance. This improvement is verified by simulation results.

Chapter 6
DCM Based Attitude Estimation

In this chapter, we describe an attitude estimation algorithm based on the DCM attitude representation and analyze its performance. This algorithm is appropriate for the implementation of a low-cost AHRS which is composed of MEMS IMU and magnetometer triad. To reduce the computational burden, we estimate only six elements of the nine elements of the DCM. Kalman filtering is used to fuse the angular rate, specific force and magnetometer triad measurements. The DCM model has an advantage over other attitude representations because it has linear measurement equations of accelerometer and magnetometer triads. For the DCM orthogonalization, we recommend a low computational burden algorithm within the integration filter. Finally experimental data is used to verify the efficiency of the algorithm.

6.1 Attitude Estimation Using Inertial Sensors

AHRS devices provide attitude and heading information for many applications. Attitude can be found using either vision systems, magnetic, and inertial sensors or using a combination of those systems. For the static case, an accelerometer triad can provide accurate tilt angles (roll and pitch) while the remaining heading angle can be found using the aid of a magnetometer triad in low-cost systems or using gyro-compassing in navigation grade inertial systems. Tilt angles are found by knowing the local gravity vector and measuring the projected gravity on the body frame axes. For the dynamic case, the angular rate vector of a gyro triad output is integrated over time to compute the new attitude. Since magnetometers and accelerometers give a direct measurement of attitude, Kalman filtering methods can correct for the accumulated error resulting from integrating the gyros' outputs. Gyro errors play an important role in determining the quality of the attitude estimation for the dynamic case. Hence, having high quality angular information implies better attitude estimation. Unfortunately, low-cost gyros are characterized by large errors; therefore, there is a need for algorithms that are capable of estimating the gyro bias vector effectively.

6.2 Literature Survey of Common Attitude Representation Methods

There are three common attitude representations that can be used in the implementation of the fusion filter, namely Euler angles, quaternion [58, 59] and DCM [60]. The DCM and quaternion attitude

based models have linear update models with respect to their parameters. One advantage of using a DCM based model is having a linear measurement model for accelerometers and magnetometers with respect to the DCM elements and hence avoiding the linearization errors and reducing computations. Another advantage over Euler-based attitude estimation is getting better results in preserving the singularity points which occur when the pitch angle reaches ±90 degrees [60].

The direct estimation of the DCM elements has been investigated previously. A Kalman filter for the state matrix estimation was developed in [61] and used to estimate a general DCM with applying different DCM orthogonalization methods. The DCM which transforms from the body coordinate frame to the local navigation frame is the most common one and henceforth we use the abbreviation DCM to refer to that matrix. In [60], we see another approach for a DCM based attitude estimation using two cascaded filters : one for estimating the tilt angles and the other for estimating the heading angle where the DCM elements to be estimated are reduced to the second and third rows. In that approach they do not apply the magnetometer triad measurements directly since they find the heading angle and then they create a pseudo-measurement for the second row of the DCM. Another example is given in [62], where the number of the estimated elements is reduced to the third row elements; however, that approach is limited only to roll and pitch angles estimation because the elements of the third row contain no trigonometric functions of the heading angle.

The DCM has nine elements and it is a representation of three independent elements, therefore it has redundancy that can be translated into relations among the DCM elements. Because of this redundancy in the DCM elements, reduction of the number of elements of the DCM to be estimated is desirable to minimize the computations and to avoid applying the nonlinear orthogonality constraints. Theoretically, we can estimate only three elements of the DCM that contain trigonometric functions of three Euler angles. On the other hand, doing so makes improper use of the accelerometer and magnetometer triads measurements. Therefore, we estimate six elements of the DCM and the remaining three elements are found using DCM orthogonalization. The most suitable six elements of the DCM to be estimated are the first and third row because gravity and magnetic field of the Earth has no east component in the NED frame. Those six elements have been used previously in [63], where two Kalman filters were used to estimate the DCM elements and the gyro bias vector. In that approach, two DCM orthogonality constraints were used as pseudo-measurements along with measurements of a magnetometer triad and a mono-axial accelerometer corrected by wind speed. Actually, there are three constraints among six elements of the DCM since they represent three independent elements. In this thesis, we use triads of inertial sensors and magnetometers. Moreover,

we adopt a procedure to benefit from the measurements of the accelerometer triad in the dynamic case and a procedure for validating the magnetometer triad measurements. We use a central filter to estimate the DCM elements and the gyro bias vector. The remaining three constraints are handled using a simple pseudo-measurement approach to ensure the orthogonality of the DCM.

6.3 Attitude Update Using Rotation Angle Vector

6.3.1 Euler Angles Update

The update of Euler angles is performed using the following equation

$$\begin{aligned} \underline{\psi}_k^n &= \underline{\psi}_{k-1}^n + E_{b,k-1}^n \underline{\tilde{\omega}}_{ib,k-1}^b \Delta t \\ E_b^n &= \begin{bmatrix} 1 & s_\theta t_\phi & c_\theta t_\phi \\ 0 & c_\theta & -s_\theta \\ 0 & s_\theta / c_\phi & c_\theta / c_\phi \end{bmatrix} \end{aligned} \tag{6.1}$$

where E_b^n is the rotation rate transformation matrix, $\underline{\psi}$ is the Euler angles vector $\underline{\psi} = [\phi \quad \theta \quad \varphi]^T$ and c_x, s_x and t_x represent the mathematical operations of $\cos(x)$, $\sin(x)$ and $\tan(x)$ respectively.

6.3.2 DCM Update

The rotation angle vector is used to update the attitude DCM of the body frame with respect to a fixed the inertial frame. The update of the attitude DCM due to the rotation of the body frame with respect to the navigation frame has the following differential equation

$$\dot{C}_b^n = C_b^n \underline{\omega}_{nb}^b \times \tag{6.2}$$

where $\underline{\omega}_{nb}^b$ is turn rate of the body frame with respect to the navigation frame expressed in the body frame and $\times$ represents the cross product operation as defined in (3.2). For low-cost gyros, the update will be mainly due to the turn rate of the body frame with respect to the inertial frame. The discrete-time solution is given as

$$C_{b,k}^n = \begin{bmatrix} c_{11} & c_{12} & c_{13} \\ c_{21} & c_{22} & c_{23} \\ c_{31} & c_{32} & c_{33} \end{bmatrix} = C_{b,k-1}^n A_{k-1} . \tag{6.3}$$

The matrix A_{k-1} is another DCM that transforms from the body coordinates at the *k*th computer cycle to the body coordinates at the *k-1*th computer cycle using the angle rotation vector as shown in [25, 64, 65]. The matrix A_{k-1} based on gyro measurement vector is computed as

$$A_{k-1} = e^{\int_{t_{k-1}}^{t_k} \underline{\omega}_{ib}^b \times dt} \quad . \tag{6.4}$$

Assuming that the angular velocity vector has little change during the update interval, we can approximate the angle rotation $\underline{\sigma}$ as

$$\underline{\sigma} = \int_{t_{k-1}}^{t_k} \underline{\omega}_{ib}^b dt \underline{\tilde{\sigma}} \approx \underline{\tilde{\omega}}_{ib}^b \Delta t \, . \tag{6.5}$$

This matrix A is computed as

$$A_{k-1} = I + \frac{\sin\sigma}{\sigma}\left[\underline{\sigma}\times\right] + \frac{1-\cos\sigma}{\sigma^2}\left[\underline{\sigma}\times\right]^2 , \; \sigma = \sqrt{\sigma_x^2 + \sigma_y^2 + \sigma_z^2} \, . \tag{6.6}$$

The matrix A considering a second order approximation is given as

$$A_{k-1} \approx \begin{bmatrix} 1 - \frac{(\sigma_y^2 + \sigma_z^2)}{2} & \frac{\sigma_x\sigma_y}{2} - \sigma_z & \frac{\sigma_x\sigma_z}{2} + \sigma_y \\ \frac{\sigma_x\sigma_y}{2} + \sigma_z & 1 - \frac{(\sigma_x^2 + \sigma_z^2)}{2} & \frac{\sigma_y\sigma_z}{2} - \sigma_x \\ \frac{\sigma_x\sigma_z}{2} - \sigma_y & \frac{\sigma_y\sigma_z}{2} + \sigma_x & 1 - \frac{(\sigma_x^2 + \sigma_y^2)}{2} \end{bmatrix} . \tag{6.7}$$

6.4 DCM Based Attitude Estimation Algorithm

The purpose of the attitude filter is to estimate the attitude through optimal fusion of angular rate, specific force and magnetometer triad measurements. In the AHRS, we aid a standard IMU, which encloses accelerometer and gyro triads, with a magnetometer triad. One important point which should be considered is the bias in inertial sensors. There are several approaches to tackle this problem such as augmentation of the bias to the state vector. The accelerometer bias vector has a small effect on the attitude estimation; hence, we assume it will not change significantly after being calibrated. We append the gyro bias vector to the six DCM elements. However, appending the gyro bias vector makes the process model nonlinear because it introduces state multiplication which can be handled using a pseudo-linear process model as shown in [61]. The state vector can be reduced to the six elements of the DCM if the gyro bias vector is captured using the zero attitude updates, known as zero velocity update (ZUPT), once the body is detected at reset. As mentioned before, we estimate the first and third row of the DCM since the elements of the second row are not observable by either accelerometer triad, at static moments, or magnetometer triad. The state vector consists of the six elements of the DCM appended with the gyro bias vector

$$\begin{aligned}&\underline{c}_1 = \begin{bmatrix} c_{11} & c_{12} & c_{13} \end{bmatrix}^T \ , \ \underline{c}_3 = \begin{bmatrix} c_{31} & c_{32} & c_{33} \end{bmatrix}^T \ , \ \underline{b}_g = \begin{bmatrix} b_{gx} & b_{gy} & b_{gz} \end{bmatrix}^T \\ &\underline{x} = \begin{bmatrix} \underline{c}_1^T & \underline{c}_3^T & \underline{b}_g^T \end{bmatrix}^T \end{aligned} \quad . \tag{6.8}$$

6.4.1 Filter Initialization and Process Update

The state vector and the estimate error covariance are initialized as shown in (3.17) and (3.18). The error model for the angular rate measurement vector is composed of Gaussian white noise error $\underline{w}_g$ and bias error $\underline{b}_g$. Hence, the angular change is computed as

$$\tilde{\underline{\sigma}} = \underline{\omega}_{ib}^b \Delta t + \underline{b}_g \Delta t + \underline{w}_g \sqrt{\Delta t} \ . \tag{6.9}$$

By substituting (6.9) in (6.7) and ignoring second order terms, the measured matrix $\tilde{A}$ can be written in terms of the exact matrix A as

$$\tilde{A}_{k-1} \approx A_{k-1} + \left[\underline{b}_g \Delta t \right] \times + \left[\underline{w}_g \sqrt{\Delta t} \right] \times . \tag{6.10}$$

The DCM update part for the selected rows and considering the gyro bias vector correction based on (6.3) is given as

$$\begin{aligned}&\underline{x}_{1:6,k} = \underline{\mathrm{f}}_{1:6,k-1}(\underline{x}_{k-1}, \underline{u}_{k-1}, \underline{w}_{k-1}) \\ &\underline{x}_{1:3,k} = \tilde{A}_{k-1}^T \underline{x}_{1:3,k-1} - \underline{x}_{1:3,k-1} \times \underline{x}_{7:9,k-1} \Delta t \\ &\underline{x}_{4:6,k} = \tilde{A}_{k-1}^T \underline{x}_{4:6,k-1} - \underline{x}_{4:6,k-1} \times \underline{x}_{7:9,k-1} \Delta t \end{aligned} \quad . \tag{6.11}$$

The gyro bias vector can be modeled as a random process driven by Gaussian white noise vector $\underline{w}_{bg}$ which is uncorrelated with the gyro noise vector $\underline{w}_g$

$$\underline{x}_{7:9,k} = \underline{x}_{7:9,k-1} + \underline{w}_{bg,k-1} \ . \tag{6.12}$$

The process covariance Q_{k-1} is composed of two parts which are the DCM elements process covariance and the gyro bias vector process covariance and it is computed as

$$\begin{aligned}&\underline{w} = \begin{bmatrix} \underline{w}_g \\ \underline{w}_{bg} \end{bmatrix}, \ L_c = \left. \frac{\partial \underline{\mathrm{f}}_{1:6,k-1}}{\partial \underline{w}_g} \right|_{\hat{\underline{x}}_{k-1}^+} = \sqrt{\Delta t} \left[\begin{matrix} \underline{x}_{1:3} \times \\ \underline{x}_{4:6} \times \end{matrix} \right]_{\hat{\underline{x}}_{k-1}^+} \\ &\Sigma_{g,k-1} = E\{ \underline{w}_{g,k-1} \underline{w}_{g,k-1}^T \} = R_g I_{3\times 3} \\ &Q_c = L_{c,k-1} \Sigma_g L_{c,k-1}^T \\ &Q_{bg} = E\{ \underline{w}_{bg_{k-1}} \underline{w}_{bg_{k-1}}^T \} = R_{bg} I_{3\times 3} \\ &Q_{k-1} = \begin{bmatrix} Q_c & 0_{6\times 3} \\ 0_{3\times 6} & Q_{bg} \end{bmatrix} \end{aligned} \quad . \tag{6.13}$$

The a priori state estimate is updated as

$$\underline{\hat{x}}_k^- = F_{k-1}\underline{\hat{x}}_{k-1}^+ \;, F_{k-1} = \begin{bmatrix} \tilde{A}_{k-1}^T & 0_{3\times3} & -\Delta t \underline{x}_{1:3} \times \\ 0_{3\times3} & \tilde{A}_{k-1}^T & -\Delta t \underline{x}_{4:6} \times \\ 0_{3\times3} & 0_{3\times3} & I_{3\times3} \end{bmatrix}_{\underline{\hat{x}}_{k-1}^+} . \tag{6.14}$$

The a priori estimation error covariance is computed as (3.26).

6.4.2 Measurement Update

The accelerometer measurement vector is used to update the tilt angles of the DCM when the AHRS is detected at static or nearly static phase. The accelerometer measurement model is assumed to be corrupted by a white Gaussian noise error. For static scenario, the only measurable acceleration is due to gravity

$$\underline{a}^b = C_n^b \underline{g}^n + \underline{v}_a, \;\; \underline{a}^b = \begin{bmatrix} a_x^b & a_y^b & a_z^b \end{bmatrix}^T . \tag{6.15}$$

The Jacobian of this measurement is simply given as

$$H_a = \begin{bmatrix} 0_{3\times3} & gI_{3\times3} & 0_{3\times3} \end{bmatrix}. \tag{6.16}$$

In practice, it is not always the case for the AHRS to be static. In fact, for the static case there is no need for a gyro update. Therefore, the variance of the accelerometer triad measurements is set to be dynamic. If the magnitude of the accelerometer triad measurements is close to the magnitude of the gravity for certain amount of time then the variance is set small. If the accelerometer triad measurement deviates much from the gravity, then the variance is increased as shown in [66-68]. This is true because the magnitude of the acceleration measurements due to gravity is always equal to g at static position regardless of the orientation.

Through the use of a magnetometer triad, we can estimate the complete attitude including the heading angle. To use this measurement vector directly, we need knowledge of the magnetic field vector in the local navigation frame. The north and down components of the magnetic field depend on the inclination angle ϑ of the Earth's magnetic field [69]. This angle is the angle between the Earth's magnetic field and surface of the Earth. The Earth's magnetic field is given as

$$\underline{h}_m^n = \begin{bmatrix} \cos(\vartheta) & 0 & \sin(\vartheta) \end{bmatrix}^T = \begin{bmatrix} h_{m_N} & 0 & h_{m_D} \end{bmatrix}^T . \tag{6.17}$$

The inclination angle can be found from tables or by transforming non-disturbed magnetometer triad vector measurement into the local navigation frame [70]. The magnetometer measurement model is

assumed to be corrupted by a white Gaussian noise error. The magnetometer triad vector measurement is related to the magnetic field vector $\underline{h}_m^n$ in the NED frame as

$$\underline{h}_m^b = C_n^b \, \underline{h}_m^n + \underline{v}_m \, . \tag{6.18}$$

The Jacobian of this measurement is given as

$$H_m = \begin{bmatrix} h_{m_N}^n I_{3\times3} & h_{m_D}^n I_{3\times3} & 0_{3\times3} \end{bmatrix}. \tag{6.19}$$

A validation test is be performed on the magnetometer triad's measurements as described in [59, 71] in similar way to accelerometer handling. Therefore, the variance of the magnetometer triad measurements is set to be dynamic. If the magnetometer triad measurement deviates much from the unity magnitude, then the variance is increased. This is true because the magnitude of the magnetometer triad measurements should equal to unity since frame transformation does not change it magnitude. The accelerometer and magnetometer triads' measurements constitute the total measurement vector $\underline{y}_k$ which has the Jacobian H_k given as

$$\underline{y}_k = \begin{bmatrix} \underline{a}^b \\ \underline{h}_m^b \end{bmatrix}_k , \; H_k = \begin{bmatrix} H_a \\ H_m \end{bmatrix}_k . \tag{6.20}$$

The measurement covariance matrices of both triads are assumed to be independent with Gaussian distribution

$$R_k = \begin{bmatrix} R_a I_{3\times3} & 0_{3\times3} \\ 0_{3\times3} & R_m I_{3\times3} \end{bmatrix}_k . \tag{6.21}$$

The Kalman gain is updated as shown in the literature covering the Kalman filtering, e.g., [37].

6.4.3 Other Approaches for Using Magnetometers

We describe other approaches of using magnetometer triad vector measurements to find the heading angle for comparison purposes only. The first approach which is given in [72] requires knowledge of the tilt angles (roll and pitch); however, the knowledge of the magnetic field in local navigation frame is not required. This approach is summarized in the following equations

$$\begin{aligned} X_h &= h_{m_x}^b \, \mathrm{c}_\theta + h_{m_y}^b \, \mathrm{s}_\theta \, \mathrm{s}_\phi + h_{m_z}^b \, \mathrm{s}_\theta \, \mathrm{c}_\phi \\ Y_h &= h_{m_y}^b \, \mathrm{c}_\phi - h_{m_z}^b s_\phi \\ \varphi &= \sin^{-1}\!\left(\frac{-Y_h}{\sqrt{X_h^2 + Y_h^2}}\right), \; \varphi = \cos^{-1}\!\left(\frac{X_h}{\sqrt{X_h^2 + Y_h^2}}\right) \end{aligned} \; . \tag{6.22}$$

Another simpler approach is given in [73] which requires knowledge of the magnetic field in local navigation frame and it is formulated as

$$\varphi = \cos^{-1}\left(\frac{h^b_{m_x} + s_\theta h^n_{m_D}}{c_\theta h^n_{m_N}}\right). \tag{6.23}$$

From (6.22) and (6.23), we see clearly the advantage of using the DCM based attitude estimation in terms of linearity and simplicity over the use of Euler angles.

6.4.4 Handling of Nonlinear Constraints of the DCM

The goal of the application of the constraints is to have an orthogonal estimated DCM. The orthogonality of the DCM implies

$$C^n_b (C^n_b)^T = I_{3\times 3}\,. \tag{6.24}$$

The non-estimated row can be found using the following property of cross product of the rows

$$\underline{c}_2 = \hat{\underline{c}}_3 \times \hat{\underline{c}}_1\,. \tag{6.25}$$

Equation (6.24) implies six nonlinear equations considered as constraints on the DCM. Since we estimate six elements, only three constraints are applicable given as

$$\begin{aligned} &c_{11}^2 + c_{12}^2 + c_{13}^2 = 1 \\ &c_{31}^2 + c_{32}^2 + c_{33}^2 = 1 \\ &c_{11}c_{31} + c_{12}c_{32} + c_{13}c_{33} = 0 \end{aligned}\,. \tag{6.26}$$

There are several approaches for handling nonlinear constraints in the literature of Kalman filtering. A comprehensive survey of the approaches can be found in [74]. Proper handling of the constraints can improve the estimation performance. We use the pseudo-measurement approach [53] to get an orthogonal DCM. Each pseudo-measurement is modeled with additive white Gaussian noise. This approach has a decreasing covariance rationale to relax the rigidity of the constraints. The Gaussian noise covariance is initialized with a large value that decreases with time as given next

$$R_{c,k} = (\eta)^k R_i I_{3\times 3} + R_{ss} I_{3\times 3} \quad 0 \le \eta < 1\,. \tag{6.27}$$

where R_{ss} represents steady state covariance and R_i represents the initial covariance. The values of R_{ss} and R_i depend on the current estimation error and can be found from consistency checks. The value of the rationale η is set to 0.92 and its rule is to allow $R_{c,k}$ decrease with time. The constraints function and its Jacobian matrix are derived from (6.26) and it is computed with the available a posteriori state as

$$\underline{h}_c(\underline{x}) = \begin{bmatrix} x_1^2 + x_2^2 + x_3^2 \\ x_4^2 + x_5^2 + x_6^2 \\ x_1x_4 + x_2x_5 + x_3x_6 \end{bmatrix} = \begin{bmatrix} 1 \\ 1 \\ 0 \end{bmatrix}$$
$$H_c = \frac{\partial \underline{h}_c(\underline{x})}{\partial \underline{x}} = \begin{bmatrix} H_1 & H_2 & 0_{3\times 3} \end{bmatrix}_{\hat{\underline{x}}_k^+},\ H_1 = \begin{bmatrix} 2x_1 & 2x_2 & 2x_3 \\ 0 & 0 & 0 \\ x_4 & x_5 & x_6 \end{bmatrix}, H_2 = \begin{bmatrix} 0 & 0 & 0 \\ 2x_4 & 2x_5 & 2x_6 \\ x_1 & x_2 & x_3 \end{bmatrix} \quad (6.28)$$

The Kalman gain, the a posteriori estimation error covariance and the a posteriori state estimate of the constraints are computed according to the EKF equations.

6.5 Experimental Results and Evaluation of the Performance

We analyze the performance of the AHRS algorithm using experimental data collected from human hand motion of the AHRS.

6.5.1 Specifications of Sensors and Parameter Settings

We used the inertial sensors and the magnetometer triad of the older version of the Xsens MTi AHRS as a low-cost platform for testing our algorithm. The specifications of the accelerometers and gyros based on manufacturer datasheet are given in Table 6.1. A total of 12000 points of sensors' measurements are collected at 0.01 s sampling time.

Table 6.1 Specifications of the used inertial sensors

Parameter (unit)	Value
Accelerometer noise ($\mathrm{m/s^2/\sqrt{Hz}}$)	0.002
Accelerometer bias stability ($\mathrm{m/s^2}$)	0.02
Gyro noise ($\mathrm{°/s/\sqrt{Hz}}$)	0.1
Gyro bias stability (°/s)	5
Magnetometer noise ($\mathrm{mGauss/\sqrt{Hz}}$)	0.5
Update rate Δt (s)	0.01

Also, we used the ITG-3200 which is a more accurate gyro triad that has noise specifications of $0.03\ \mathrm{°/s/\sqrt{Hz}}$ to evaluate the filter. Both sensors were mounted to a common base and calibrated for misalignment and bias parameters using a turn table. We refer to Xsens MTi gyro triad as GT1 and to ITG-3200 as GT2 for simplicity.

6.5.2 Trajectory Profile

We kept the common base static at the beginning of the experiment at a known attitude to have accurate reference of the initial conditions and the gyro bias vector then we moved the system using hand motion. Since the both gyro triads do not detect Earth rotation, the outputs of the gyro triads can be adjusted to zero at reset position. Within the trajectory profile, we positioned the base through the initial position to let the filter rest the accumulated errors. Also, we kept the base static at the end at the same initial attitude to have an accurate reference. The plots of the GT1 outputs are shown in Fig. 6.1.

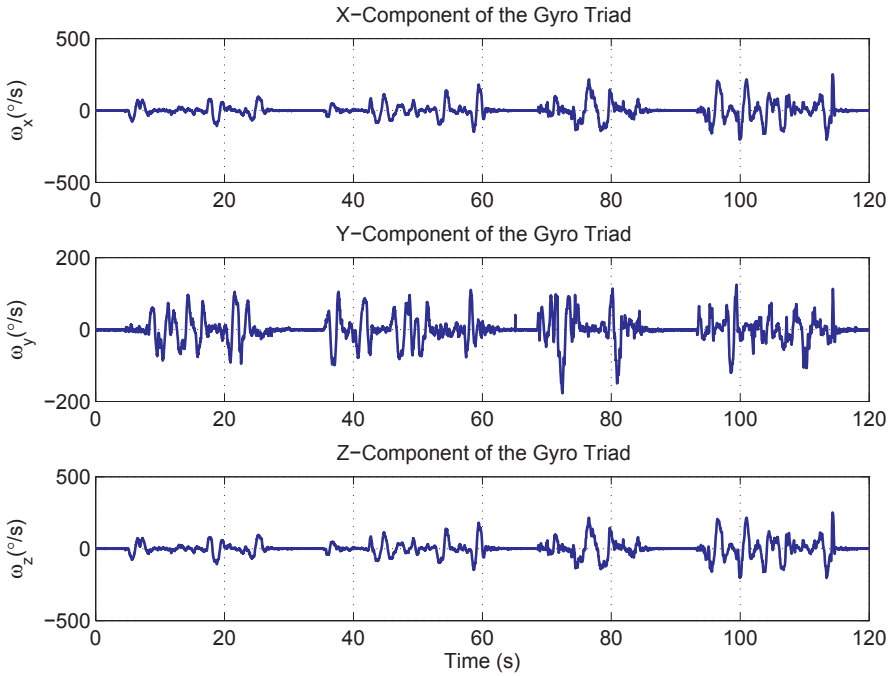

Fig. 6.1 Angular velocity profile measured by the Xsens gyro triad GT1

Fig. 6.2 shows the plots of proper acceleration measured by the Xsens accelerometer triad.

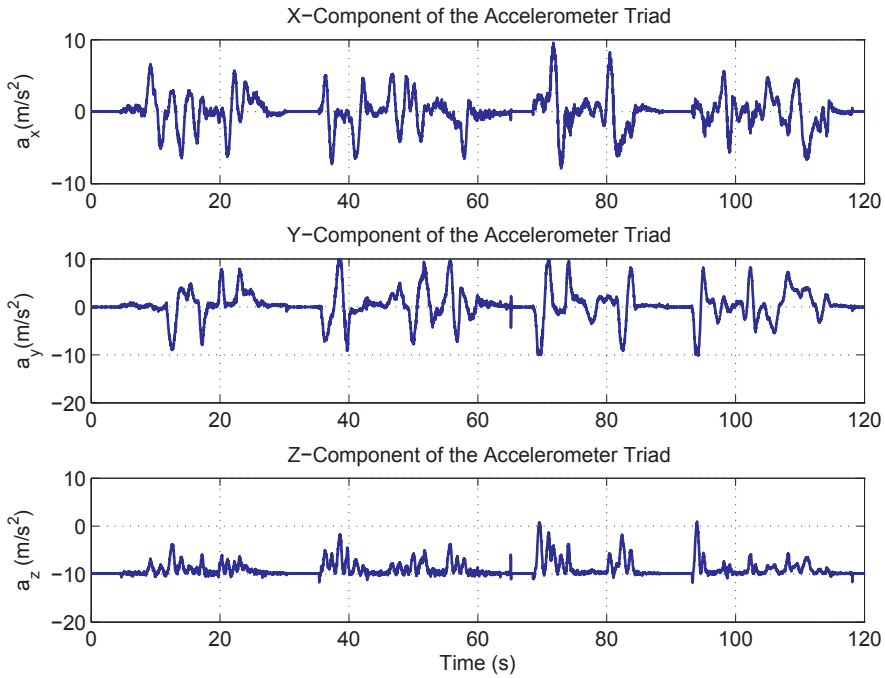

Fig. 6.2 Proper acceleration profile measured by the Xsens accelerometer triad

The outputs of the accelerometer triad show a small value of the accelerometer bias vector which has a small effect on the estimation of the tilts angles. They also show the static moments which will be used for correction.

6.5.3 Attitude Estimation Filter Results

In Fig. 6.3, we plot the results of the Euler angles extracted from the estimated DCM elements, denoted as estimated Euler angles for simplicity for both gyro triads. We also plot Euler angles computed by accumulation of the biased GT1 measurement vector and the bias calibrated GT2 measurement vector. The accumulated Euler angles are initialized correctly with the available accelerometer and magnetometer triads' measurements. We do so to show the effect of the gyro bias vector on the computation of the Euler angles by direct accumulation. The non-biased accumulation of GT2 is used to show the effect of gyro noise on the error accumulation.

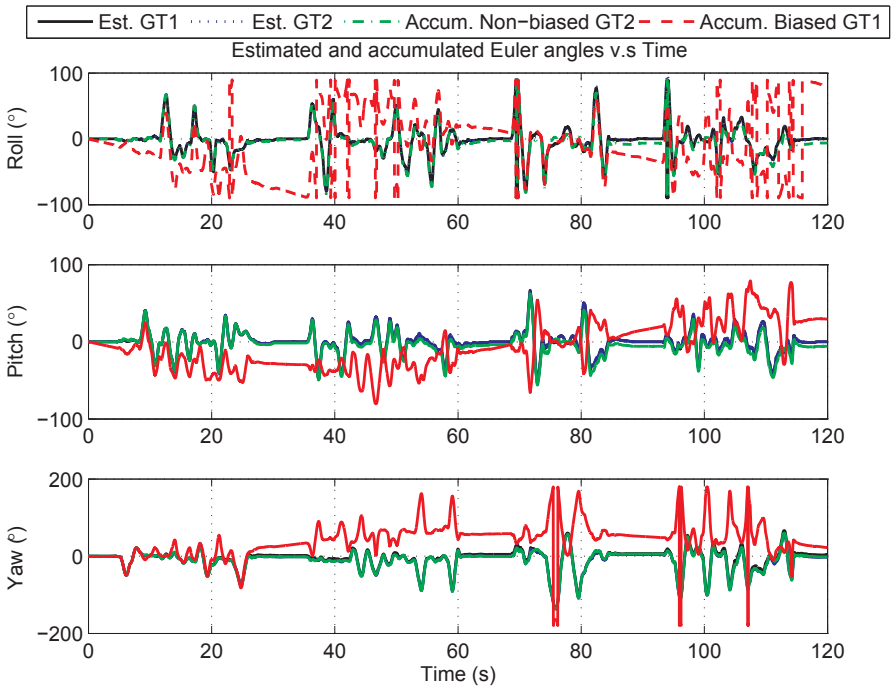

Fig. 6.3 Estimated and accumulated Euler angles

From Fig. 6.3, we see that the estimated Euler angles using both gyro triads are in agreement with those computed by the accumulation of the non-biased GT2 measurement vector. The accumulated Euler angles computed from the biased GT1 measurement vector diverge quickly due to the large gyro bias vector while the accumulated Euler angles computed from the non-biased GT2 measurement vector diverge at a much slower rate. The plots show the advantage of the accelerometer and magnetometer triads' corrections for the estimated Euler angles. Fig. 6.4 shows the difference between the estimated bias and the mean of the gyro bias at static position for the three components of GT1. The estimated gyro bias vector converges quickly to the true vector value with small estimation error though it was initialized improperly to test the filter capability of convergence.

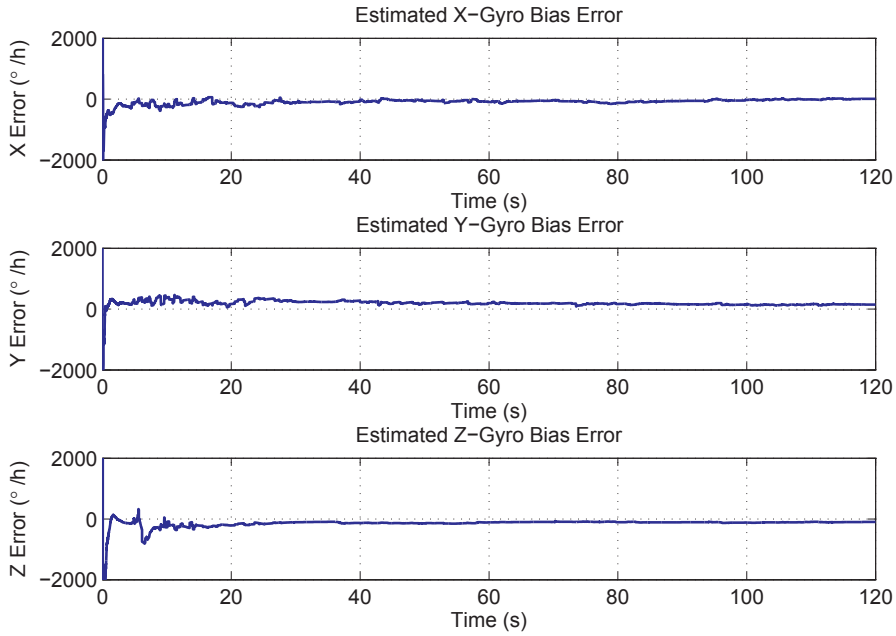

Fig. 6.4 Estimation error of the gyro bias vector

6.6 Summary

In this chapter, we presented the algorithm and the experimental results for a reduced DCM based attitude estimation filter implemented using low-cost IMU and magnetometer triad. The gyro bias vector was appended to the state vector to be estimated. The DCM attitude estimation filer is characterized by its linear measurement model for accelerometer and magnetometer triads. The experimental results show the validity of the filter for low-cost inertial sensors and the capability of the filter in estimating the gyro bias vector. The results also show the divergence effect of non-calibrated gyro bias vector in the accumulated Euler angles. Further research can be conducted to compare the performance and the computational load of the DCM algorithm with Euler and quaternion based attitude estimation algorithms.

Chapter 7
DCM Based GPS/INS Integration

In this chapter, we derive a GPS/INS integration algorithm based on the DCM attitude representation model and analyze its performance. The motivation for this work is to find an algorithm that is capable of tracking the variation of the gyro bias vector during operations and that benefits from the established DCM based attitude estimation algorithms. Filter performance is evaluated using a simulation based on an air vehicle trajectory profile and is compared with Euler angles based UKF. We investigate the effects of improper initialization of the state vector on the filter performance. These results are supplemented using experimental data collected along a car route with two different grades of IMUs. The DCM based model has some advantages over other attitude representations due to its relatively moderate computational load and applicability with different categories of inertial sensors.

7.1 Literature Survey for DCM Based Integrated Navigation

The direct estimation of the DCM elements has been investigated previously; however, it was not used with GPS/INS integration specifically. Most of the previous use focuses on the use of the DCM for AHRS implementation [60-62]. Little attention is given to combine the DCM elements attitude estimation within GPS/INS integration filter. One example for the use of the DCM in INS/GPS is given in [75]; however, the main integration filter is based on error model of Euler angles and the DCM based attitude estimation algorithm is used to estimate the roll and pitch by benefiting from accelerometer triad measurements. The estimated tilt angles are used as measurements in the main INS/GPS algorithm. In our approach, we use only the DCM as attitude representation.

7.1.1 Current GPS/INS Integration Algorithms based on Euler Angles

The Kalman filter is a linear recursive estimation tool that is used for GPS/INS integration. Most of the previous GPS/INS integration filters focus on the use of Euler angles based model which has less number of elements; however it has high nonlinearity due to the use of sinusoidal terms in the process model. Moreover, the direct measurements of magnetometers, which are used often with low-cost inertial sensors, are also nonlinear if it has been used to find Euler angles. Several approaches can be used to overcome the nonlinearity such as using EKF, which gives first order approximation, or using the UKF. Generally, the use of the UKF for the total state model gives good estimation results compared with other linearization methods but it is often highly computationally demanding. The

UKF approximates the distribution function using a certain number of samples instead of approximating the function itself. On the other hand, the linearized error model based on Euler angles attitude representation works well under the conditions of good calibration and alignment of inertial sensors. Under the assumption of small angular change within time update intervals, the error model based on Euler angles can be greatly simplified but that assumption is unlikely to hold when using low-cost gyros that are characterized by large time-varying bias. Low-cost MEMS inertial sensors are characterized by having a large random bias that drifts slowly with time due to its dependency on many parameters such as temperature and gravity sensitivity. Therefore, the bias parameters of MEMS inertial sensors should be calibrated in advance and during the flight for a proper GPS/INS integration using the simplified linearized error model. The on-the-fly bias compensation is needed since the bias components are not constant rather they drift over time. We refer the reader to [76], for a comparison between different Kalman filtering methods to overcome system nonlinearity based on Euler angles for low-cost sensors.

7.1.2 Estimation of the DCM Elements within the GPS/INS Integration Algorithm

The advantages of using DCM as attitude representation was detailed in section 6.2. Since the computation of the DCM is required in any integration approach in the strapdown mechanization equation, estimating it can reduce computations. Though the use of the DCM implies a larger state space model, its computational load is relatively moderate due to its simple time update model.

7.2 The Strapdown Mechanization and DCM Based Filter Formulation

The strapdown mechanization algorithms [25] are the basis for the GPS/INS integration approach. We use the local navigation frame mechanization given as

$$\begin{aligned} \dot{\underline{r}}^n &= \underline{\upsilon}^n \\ \dot{\underline{\upsilon}}^n &= \underline{C}_b^n \underline{a}^b - (2\underline{\omega}_{ie}^n \times + \underline{\omega}_{en}^n \times)\underline{\upsilon}^n + \underline{g}^n \\ \dot{C}_b^n &= C_b^n \underline{\omega}_{nb}^b \times \end{aligned} \tag{7.1}$$

where

$\underline{r}^n$: Position expressed in the NED frame.

$\underline{\upsilon}^n$: Velocity expressed in the NED frame.

$\underline{a}^b$: The true accelerometer measurement vector expressed in the body frame.

$\underline{g}^n$: The gravity vector in the local navigation frame $\begin{bmatrix} 0 & 0 & g \end{bmatrix}^T$.

C_b^n : A DCM that transforms the inertial measurements from the body frame denoted as *b* to the local navigation frame denoted as *n*.

ω_{ie}^n : Earth's turn rate expressed in the body frame.

$\underline{\omega}_{en}^n$: Turn rate of the local navigation frame (transport rate).

$\underline{\omega}_{nb}^n$: Turn rate of the body frame with respect to the local navigation frame.

$\times$: represents the cross product operation defined as skew symmetric form

$$\underline{\omega} = \begin{bmatrix} \omega_x \\ \omega_y \\ \omega_z \end{bmatrix} \quad , \quad \underline{\omega}\times = \begin{bmatrix} 0 & -\omega_z & \omega_y \\ \omega_z & 0 & -\omega_x \\ -\omega_y & \omega_x & 0 \end{bmatrix}. \tag{7.2}$$

7.2.1 State Vector to Be Estimated

We apply the integration approach here to a loosely coupled scenario; however, it is also applicable to other integration scenarios. The state vector is composed of the nine elements of the DCM, the gyros triad bias vector, the accelerometer triad bias vector and six states of position and velocity expressed in the local navigation frame. The elements of the state vector are ordered in the following form

$$\begin{aligned} &\underline{x} = \begin{bmatrix} \underline{c}_1^T & \underline{c}_2^T & \underline{c}_3^T & \underline{b}_g^T & \underline{r}^{n,T} & \underline{\upsilon}^{n,T} & \underline{b}_a^T \end{bmatrix}^T \\ &\underline{c}_1 = \begin{bmatrix} c_{11} & c_{12} & c_{13} \end{bmatrix}^T \ , \ \underline{c}_2 = \begin{bmatrix} c_{21} & c_{22} & c_{23} \end{bmatrix}^T \ , \ \underline{c}_3 = \begin{bmatrix} c_{31} & c_{32} & c_{33} \end{bmatrix}^T , \ \underline{b}_g = \begin{bmatrix} b_{gx} & b_{gy} & b_{gz} \end{bmatrix}^T . \\ &\underline{r}^n = \begin{bmatrix} r_N & r_E & r_D \end{bmatrix}^T , \ \underline{\upsilon}^n = \begin{bmatrix} \upsilon_N & \upsilon_E & \upsilon_D \end{bmatrix}^T , \ \underline{b}_a = \begin{bmatrix} b_{ax} & b_{ay} & b_{az} \end{bmatrix}^T \end{aligned} \tag{7.3}$$

where

$\underline{b}_a$: Accelerometer triad bias vector.

$\underline{b}_g$: Gyro triad bias vector.

7.2.2 System Modeling

The process update is divided into four parts which are the update of the DCM elements, update of gyro bias vector, update of position and velocity vectors and update of acceleration bias vector. The rotation angle vector which is the turn angle of the body frame with respect to a fixed inertial frame is used to update the attitude DCM. Attitude update with respect to a local navigation frame is composed of two updates: one due to the body frame rotation with respect to the inertial frame and the other due to the rotation of the navigation frame with respect to a fixed inertial frame [64]. For low-cost gyros,

the craft rate can be ignored and the update will be mainly due to the turn rate of the body frame with respect to the inertial frame. The discrete-time solution is given as

$$C_{b,k}^{n} = C_{b,k-1}^{n} A_{k-1} . \tag{7.4}$$

The error model for the angular rate measurement vector is composed of Gaussian white noise error $\underline{w}_g$ and bias error $\underline{b}_g$. Hence, the gyro triad measurement vector is given as

$$\tilde{\underline{\omega}}_{ib}^{b} = \underline{\omega}_{ib}^{b} + \underline{b}_g + \underline{w}_g \big/ \sqrt{\Delta t} . \tag{7.5}$$

By ignoring the quadratic terms of gyro errors of bias and noise, the matrix $\tilde{A}$ can be approximated and written in terms of the exact matrix A as

$$\tilde{A}_{k-1} \approx A_{k-1} + \left[\underline{b}_g \Delta t \right] \times + \left[\underline{w}_g \sqrt{\Delta t} \right] \times . \tag{7.6}$$

The DCM update part is given as

$$\begin{aligned}
\underline{x}_{1:9,k} &= \underline{\mathrm{f}}_{1:9,k-1}(\underline{x}_{k-1}, \underline{u}_{k-1,} \underline{w}_{k-1}) \\
\underline{x}_{1:3,k} &= \tilde{A}_{k-1}^{T} \underline{x}_{1:3,k-1} - \underline{x}_{1:3,k-1} \times \underline{x}_{10:12,k-1} \Delta t \\
\underline{x}_{4:6,k} &= \tilde{A}_{k-1}^{T} \underline{x}_{4:6,k-1} - \underline{x}_{4:6,k-1} \times \underline{x}_{10:12,k-1} \Delta t \\
\underline{x}_{7:9,k} &= \tilde{A}_{k-1}^{T} \underline{x}_{7:9,k-1} - \underline{x}_{7:9,k-1} \times \underline{x}_{10:12,k-1} \Delta t
\end{aligned} . \tag{7.7}$$

The gyro bias vector can be modeled as a random process driven by white noise

$$\underline{x}_{10:12,k} = \underline{\mathrm{f}}_{10:12,k-1}(\underline{x}_{k-1}, \underline{u}_{k-1,} \underline{w}_{k-1}) = \underline{x}_{10:12,k-1} + \underline{w}_{bg,k-1} . \tag{7.8}$$

The error model for the accelerometer triad measurement vector is composed of Gaussian white noise error $\underline{w}_{acc}$ and bias error $\underline{b}_a$. Hence, the accelerometer measurement vector is given as

$$\tilde{\underline{a}}^{b} = \underline{a}^{b} + \underline{b}_a + \underline{w}_{acc}, \quad \tilde{\underline{a}}^{b} = \left[\tilde{a}_x^b \quad \tilde{a}_y^b \quad \tilde{a}_z^b \right]^T . \tag{7.9}$$

Using the strapdown local navigation frame mechanization given in (7.1), the velocity and position process update model can be simplified by ignoring the craft rate as

$$\begin{aligned}
\underline{x}_{13:15,k} &= \underline{\mathrm{f}}_{13:15,k-1}(\underline{x}_{k-1}, \underline{u}_{k-1,} \underline{w}_{k-1}) = \underline{x}_{13:15,k-1} + \underline{x}_{16:18,k-1} \Delta t \\
\underline{x}_{16:18,k} &= \underline{\mathrm{f}}_{16:18,k-1}(\underline{x}_{k-1}, \underline{u}_{k-1,} \underline{w}_{k-1}) = \underline{x}_{16:18,k-1} + C_b^n \Big|_{\underline{x}_{k-1}} (\tilde{\underline{a}}^{b} - \underline{x}_{19:21,k-1}) \Delta t + \underline{g}^{n} \Delta t
\end{aligned} . \tag{7.10}$$

In a similar way to the modeling of gyro bias vector, the accelerometer bias vector can be modeled as a random process driven by white noise

$$\underline{x}_{19:21,k} = \underline{\mathrm{f}}_{19:21,k-1}(\underline{x}_{k-1}, \underline{u}_{k-1,} \underline{w}_{k-1}) = \underline{x}_{19:21,k-1} + \underline{w}_{ba,k-1} . \tag{7.11}$$

Considering evaluating the following state transition matrix at $\hat{\underline{x}}_{k-1}^{+}$, the whole process can have a pseudo-linear form given as

$$\underline{x}_k = F_{k-1}\underline{x}_{k-1} + \underline{g}^c \Delta t + \Lambda \begin{bmatrix} \underline{w}_{bg} \\ \underline{w}_{ba} \end{bmatrix}$$

$$\Lambda = \begin{bmatrix} 0_{9\times3} & 0_{9\times3} \\ I_{3\times3} & 0_{3\times3} \\ 0_{6\times3} & 0_{6\times3} \\ 0_{3\times3} & I_{3\times3} \end{bmatrix}, F_{k-1} = \begin{bmatrix} F_{11} & F_{12} \\ F_{21} & F_{22} \end{bmatrix}, F_{11} = \begin{bmatrix} \tilde{A}_{k-1}^T & 0_{3\times3} & 0_{3\times3} & -\Delta t \underline{x}_{1:3}\times \\ 0_{3\times3} & \tilde{A}_{k-1}^T & 0_{3\times3} & -\Delta t \underline{x}_{4:6}\times \\ 0_{3\times3} & 0_{3\times3} & \tilde{A}_{k-1}^T & -\Delta t \underline{x}_{7:9}\times \\ 0_{3\times3} & 0_{3\times3} & 0_{3\times3} & I_{3\times3} \end{bmatrix}, F_{12} = \begin{bmatrix} 0_{12\times9} \end{bmatrix}$$

$$F_{21} = \begin{bmatrix} 0_{3\times3} & 0_{3\times3} & 0_{3\times3} & 0_{3\times3} \\ \Delta t D_1 & \Delta t D_2 & \Delta t D_3 & 0_{3\times3} \\ 0_{3\times3} & 0_{3\times3} & 0_{3\times3} & 0_{3\times3} \end{bmatrix}, F_{22} = \begin{bmatrix} I_{3\times3} & \Delta t I_{3\times3} & 0_{3\times3} \\ 0_{3\times3} & I_{3\times3} & -\Delta t C_b^n \\ 0_{3\times3} & 0_{3\times3} & I_{3\times3} \end{bmatrix} \quad . \tag{7.12}$$

$$D_1 = \begin{bmatrix} \tilde{a}_x^b & \tilde{a}_y^b & \tilde{a}_z^b \\ 0 & 0 & 0 \\ 0 & 0 & 0 \end{bmatrix}, D_2 = \begin{bmatrix} 0 & 0 & 0 \\ \tilde{a}_x^b & \tilde{a}_y^b & \tilde{a}_z^b \\ 0 & 0 & 0 \end{bmatrix}, D_3 = \begin{bmatrix} 0 & 0 & 0 \\ 0 & 0 & 0 \\ \tilde{a}_x^b & \tilde{a}_y^b & \tilde{a}_z^b \end{bmatrix},$$

$$\underline{g}^c = \begin{bmatrix} 0 & 0 & 0 & 0 & 0 & 0 & 0 & 0 & 0 & 0 & 0 & 0 & 0 & 0 & 0 & 0 & 0 & g & 0 & 0 & 0 \end{bmatrix}^T$$

7.2.3 Filter Initialization and Prediction

The initial state vector and the initial estimate error covariance are set as

$$\begin{aligned} \hat{\underline{x}}_0^+ &= E\{\underline{x}_0\} \\ P_0^+ &= E\{(\underline{x}_0 - \hat{\underline{x}}_0^+)(\underline{x}_0 - \hat{\underline{x}}_0^+)^T\} \end{aligned} . \tag{7.13}$$

The a priori state estimate can be updated either using the process model given in (7.7) - (7.10) or using the model given in (7.12) with the matrix F_{k-1} evaluated with last available state vector estimate $\hat{\underline{x}}_{k-1}^+$ as shown in [61] for the attitude part. It is clear that the process model defined in (7.7) - (7.10) has less computational load than the process model defined in (7.12) due to avoiding multiplications of zeros. Considering the model given in for clarity, the a priori state estimate is updated as

$$\hat{\underline{x}}_k^- = F_{k-1}\big|_{\hat{\underline{x}}_{k-1}^+} \hat{\underline{x}}_{k-1}^+ + \underline{g}^c \, . \tag{7.14}$$

Assuming the elements of the process noise vector $\underline{w}$ are uncorrelated, the process covariance is computed as

$$
\begin{aligned}
&\underline{w} = \begin{bmatrix} \underline{w}_g \\ \underline{w}_{bg} \\ \underline{w}_{acc} \\ \underline{w}_{ba} \end{bmatrix}, L_c = \left.\frac{\partial \underline{\mathrm{f}}_{1:9}}{\partial \underline{w}_g}\right|_{\hat{\underline{x}}^+_{k-1}} = \sqrt{\Delta t}\left[\begin{matrix} \underline{x}_{1:3}\times \\ \underline{x}_{4:6}\times \\ \underline{x}_{7:9}\times \end{matrix}\right]_{\hat{\underline{x}}^+_{k-1}} \\
&Q_c = L_{c,k\text{-}1}\sum_g L^T_{c,k\text{-}1}, \quad \sum_g = E\{\underline{w}_{g_{k-1}}\underline{w}^T_{g_{k-1}}\} = R_g I_{3\times 3} \\
&L_{pv} = \left.\frac{\partial \underline{\mathrm{f}}_{13:18}}{\partial \underline{w}_{acc}}\right|_{\hat{\underline{x}}^+_{k-1}} = \sqrt{\Delta t}\left[\begin{matrix} 0_{3\times 3} \\ C_b^n \end{matrix}\right]_{\hat{\underline{x}}^+_{k-1}} \\
&Q_{pv} = L_{pv,k\text{-}1}\ \sum_{acc} L^T_{pv,k\text{-}1},\ \sum_{acc} = E\{\underline{w}_{acc_{k-1}}\underline{w}^T_{acc_{k-1}}\} = R_{acc} I_{3\times 3}\ . \\
&Q_{ba} = E\{\underline{w}_{ba_{k-1}}\underline{w}^T_{ba_{k-1}}\} = R_{ba} I_{3\times 3} \\
&Q_{bg} = E\{\underline{w}_{bg_{k-1}}\underline{w}^T_{bg_{k-1}}\} = R_{bg} I_{3\times 3} \\
&Q_{k\text{-}1} = \begin{bmatrix} Q_c & 0_{9\times 3} & 0_{9\times 6} & 0_{9\times 3} \\ 0_{3\times 9} & Q_{bg} & 0_{3\times 6} & 0_{3\times 3} \\ 0_{6\times 9} & 0_{6\times 3} & Q_{pv} & 0_{6\times 3} \\ 0_{3\times 9} & 0_{3\times 3} & 0_{3\times 6} & Q_{ba} \end{bmatrix}
\end{aligned}
\tag{7.15}
$$

The a priori estimation error covariance is computed as

$$
P_k^- = F_{k-1} P_{k-1}^+ F_{k-1}^T + Q_{k-1}\,. \tag{7.16}
$$

7.2.4 Measurement Update

In the loosely coupled mode, an observation from a GPS receiver consists of the position and the velocity vectors and hence the measurement and the Jacobian matrix for GPS observables are given as

$$
\begin{aligned}
&\underline{y}_k = H_{GPS}\underline{x}_k + \underline{v}_{k,GPS} = \begin{bmatrix} \underline{x}_{13:15} \\ \underline{x}_{16:18} \end{bmatrix} + \underline{v}_{k,GPS} \\
&H_{GPS} = \begin{bmatrix} 0_{3\times 3} & 0_{3\times 3} & 0_{3\times 3} & 0_{3\times 3} & I_{3\times 3} & 0_{3\times 3} & 0_{3\times 3} \\ 0_{3\times 3} & 0_{3\times 3} & 0_{3\times 3} & 0_{3\times 3} & 0_{3\times 3} & I_{3\times 3} & 0_{3\times 3} \end{bmatrix}.
\end{aligned}
\tag{7.17}
$$

The measurement covariance matrix is set to be dynamic to adapt to improper GPS estimates. The covariance is decreased when the GPS solution is good and increased if it is not good. The Position dilution of precision (PDOP), which is computed based on the geometry of the satellites, is used as a measure for the estimated position and velocity accuracy.

The accelerometer measurement vector can be used to update the tilt angles of the DCM when the accelerometer triad is detected at static or nearly static phase. For static scenario, the only measurable acceleration is due to gravity

$$\tilde{\underline{a}}^b = C_n^b \, \underline{g}^n + \underline{b}_a + \underline{w}_{acc} \, . \tag{7.18}$$

The Jacobian of this measurement is simply given as

$$H_a = \begin{bmatrix} 0_{3\times3} & 0_{3\times3} & gI_{3\times3} & 0_{9\times3} & I_{3\times3} \end{bmatrix} . \tag{7.19}$$

For AHRS applications, the variance of the accelerometer triad measurements is set to be dynamic. If the magnitude of the accelerometer triad measurements is close to the magnitude of the gravity for certain amount of time then the variance is set small. If the accelerometer triad measurement deviates much from the gravity, then the variance is increased as shown in [66-68]. This is true because the magnitude of the acceleration measurements due to gravity is always equal to g at static position regardless of the orientation. For the GPS/INS integration filter, the acceleration check might not be enough. To ensure correct update of this measurement, we additionally check the magnitude of the predicted speed for certain amount of time and if it is close to zero then the measurement is validated otherwise it will not be incorporated. Cross correlation, as a result of using the measurement of the accelerometer triad in the process and in the measurement update, can be ignored for simplicity.

The magnetometer triad measurement can be used to estimate the attitude DCM in a linear form with respect to the DCM elements. To do so, we need knowledge of the magnetic field vector in the local navigation frame. The north and the down components of the magnetic field are dependent on the inclination angle ϑ of the Earth's magnetic field [69]

$$\underline{h}_m^n = \begin{bmatrix} h_{m_N}^n & 0 & h_{m_D}^n \end{bmatrix}^T = \begin{bmatrix} \cos(\vartheta) & 0 & \sin(\vartheta) \end{bmatrix}^T . \tag{7.20}$$

Considering a Gaussian white noise error model, the magnetometer triad vector measurement is related to the magnetic field vector $\underline{h}_m^n$ in the NED frame as

$$\begin{aligned} \underline{h}_m^b &= \begin{bmatrix} h_{m_x}^b & m_{m_y}^b & h_{m_z}^b \end{bmatrix}^T = C_n^b \, \underline{h}_m^n + \underline{v}_m \\ H_m &= \begin{bmatrix} h_{m_N}^n I_{3\times3} & 0_{3\times3} & h_{m_D}^n I_{3\times3} & 0_{12\times3} \end{bmatrix} \end{aligned} . \tag{7.21}$$

A validation test is performed on the magnetometer triad's measurements as described in [59, 71]. Other approaches to use the magnetometer vector measurements to find the heading angle are described in [72, 73] ; however they contain trigonometric functions of the Euler angles. In this work, we do not use the magnetometer triad output because we focus on GPS and inertial sensors. The Kalman gain, the a posteriori estimation error covariance and the a posteriori state estimate are updated as given in the equation set (3.32)-(3.34).

7.3 Total State Euler Angles Based UKF

For performance comparison, we select the total state Euler angles based UKF algorithm due to its superior performance over the EKF. Since we use a loosely coupled filter, the sigma points are applied to the nonlinear process model to extract the a priori estimates from the transformed state vectors and for linear measurement update part we use the normal Kalman filter. For simplicity, we refer to the Euler angles based UKF as EAUKF and for DCM Based Kalman filter as DCMKF in the rest of this chapter. Next, we describe briefly the EAUKF model and its governing equations.

7.3.1 State Vector to Be Estimated

The state vector is composed of the position and velocity vectors expressed in the local navigation frame, three Euler angles, the gyros triad bias vector and the accelerometer triad bias vector

$$\begin{aligned}
&\underline{x} = \begin{bmatrix} \underline{r}^{n,T} & \underline{v}^{n,T} & \underline{\psi}^{T} & \underline{b}_a{}^{T} & \underline{b}_g{}^{T} \end{bmatrix}^T \\
&\underline{r}^n = \begin{bmatrix} r_N & r_E & r_D \end{bmatrix}^T,\ \underline{v}^n = \begin{bmatrix} v_N & v_E & v_D \end{bmatrix}^T,\ \underline{\psi} = \begin{bmatrix} \phi & \theta & \varphi \end{bmatrix}^T \ . \\
&\underline{b}_a = \begin{bmatrix} b_{ax} & b_{ay} & b_{az} \end{bmatrix}^T,\ \underline{b}_g = \begin{bmatrix} b_{gx} & b_{gy} & b_{gz} \end{bmatrix}^T
\end{aligned} \tag{7.22}$$

7.3.2 Filter Initialization Prediction

The simplified mechanization model in discrete-time can be expressed in the navigation frame as

$$\begin{aligned}
&\underline{r}_k^n = \underline{r}_{k-1}^n + \underline{v}_{k-1}^n \Delta t \\
&\underline{v}_k^n = (C_{b,k-1}^n (\tilde{a}_{k-1}^b - \underline{b}_{a,k-1}) + \underline{g}^n) \Delta t \\
&\underline{\psi}_k^n = \underline{\psi}_{k-1}^n + E_{b,k-1}^n (\tilde{\underline{\omega}}_{ib,k-1}^b - \underline{b}_{g,k-1}) \Delta t \\
&E_b^n = \begin{bmatrix} 1 & s_\theta t_\phi & c_\theta t_\phi \\ 0 & c_\theta & -s_\theta \\ 0 & s_\theta / c_\phi & c_\theta / c_\phi \end{bmatrix}
\end{aligned} \ . \tag{7.23}$$

The initial state vector and the initial estimate error covariance are computed as given in (7.13). The UKF equations are formulated as given in [37]. For n dimensional state model, we choose $2n$ sigma points vectors as follows

$$\underline{x}^{(i)} = \hat{\underline{x}}_{k-1}^+ + \left(\sqrt{n P_{k-1}^+} \right)_i^T, \underline{x}^{(i+n)} = \hat{\underline{x}}_{k-1}^+ - \left(\sqrt{n P_{k-1}^+} \right)_i^T \quad i = 1,..,n \ . \tag{7.24}$$

The a priori estimate is computed from the mean of the transformed sigma points

$$\hat{\underline{x}}_k^- = \frac{1}{2n} \sum_{i=1}^{2n} \underline{\mathrm{f}}_{k-1} (\underline{x}^{(i)}) \ . \tag{7.25}$$

The a priori error covariance is computed from the transformed sigma points as

$$P_k^- = \frac{1}{2n}\sum_{i=1}^{2n}(\underline{\mathrm{f}}_{k-1}(\underline{x}^{(i)}) - \underline{\hat{x}}_k^-)(\underline{\mathrm{f}}_{k-1}(\underline{x}^{(i)}) - \underline{\hat{x}}_k^-)^T + Q_{k-1} \quad (7.26)$$

where $\sqrt{nP}$ is the matrix square root of nP such that $\left(\sqrt{nP}\right)^T\left(\sqrt{nP}\right) = nP$ which can be obtained from the Cholesky factorization 'CHOL' in MATLAB and $\left(\sqrt{nP}\right)_i$ is the ith row of $\sqrt{nP}$. The matrix Q_{k-1} is the covariance matrix of the system process noise.

7.3.3 Measurement Update

The Kalman gain, the a posteriori estimation error covariance and the a posteriori state estimate are computed according to (3.32)-(3.34).

7.4 Simulation Result of Air Vehicle

7.4.1 Trajectory Profile and Simulation Parameters

In this part, we use a 3D trajectory profile of air vehicle as shown in Fig. 7.1 to evaluate the integration performance of the filters.

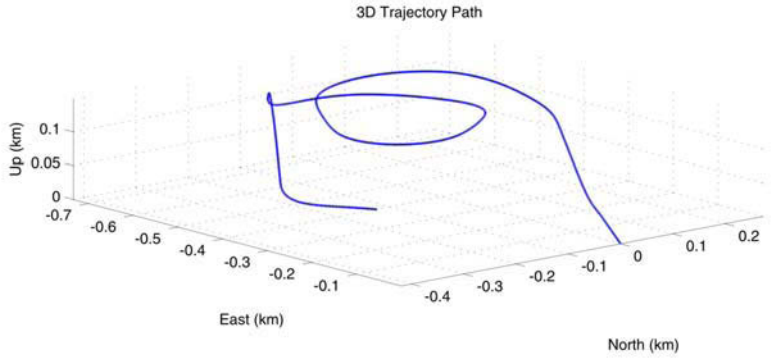

Fig. 7.1 Trajectory profile in 3D

The velocity profile has a highly varying dynamics in the three dimensional components as shown in Fig. 7.2. This trajectory is a mechanization of a high quality inertial data. For that reason, it is used as a reference for generating the GPS measurements of position and velocity at 2 Hz frequency. Due to the high dynamics, only measurements from the GPS are used in the measurement update part of the

filter. The generated GPS measurements have a seeded Gaussian error of one standard deviation equal to 3 m for the position vector and 0.5 m /s for the velocity vector measurements.

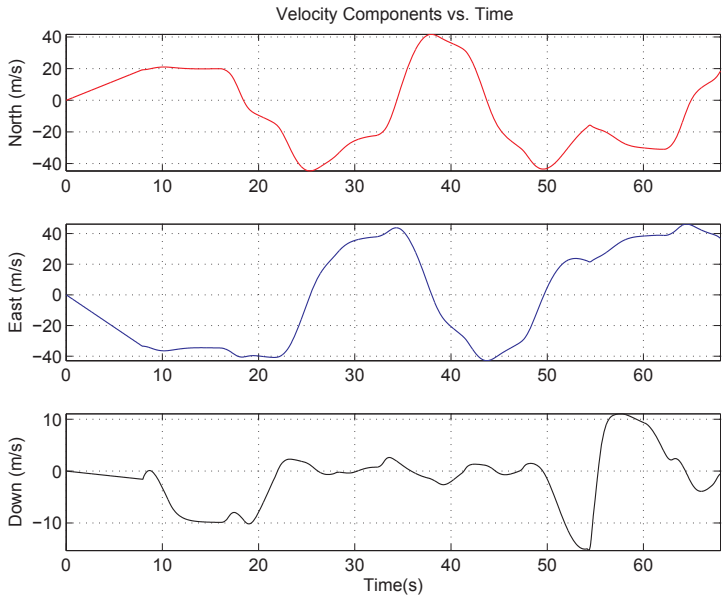

Fig. 7.2 Velocity profile in 3D

The Euler angles profile is shown in Fig. 7.3.

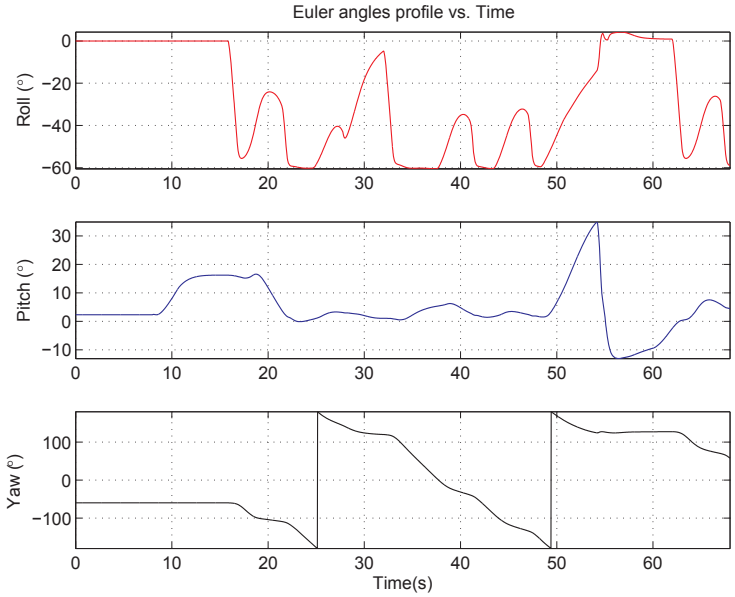

Fig. 7.3 Euler angles profile

The specifications of the seeded noise and bias errors of the inertial sensors and the GPS measurements are given in Table 7.1. The total time of the flight is 68 seconds.

Table 7.1 Numerical values of the simulation parameters

Parameter (Unit)	σ_p (m)	σ_v (m/s)	f_{GPS} (Hz)	Δt (s)	$w_{acc.}$ $(g/\sqrt{Hz})$	w_g $(^\circ/\sqrt{h})$	b_g $(^\circ/h)$	b_a (mg)
Value	3	0.5	2	0.02	$100\,\mu$	3	1500	1

7.4.2 Results for Proper Initialization

In this part, we initialized both filters with accurate values of the DCM and the bias parameters. The position and velocity were initialized with the available measurement from the GPS and hence we set the initial position and velocity error covariance according to the values in Table 7.1. In Fig. 7.4, we plot the estimated Euler angles errors extracted from the estimated DCM elements, denoted as the estimated Euler angles for simplicity and those directly estimated by the EAUKF.

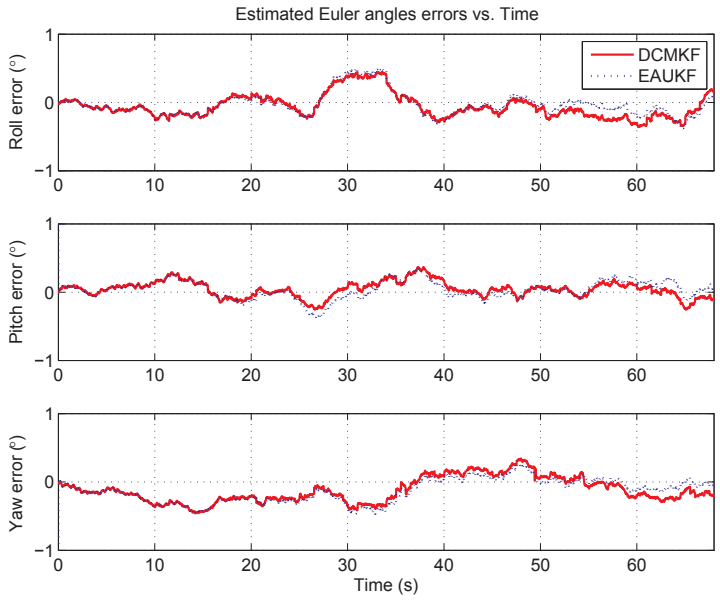

Fig. 7.4 Estimated Euler angles errors

In Fig. 7.4 both estimated Euler angles vectors components have a bounded error of 0.5°. The errors in the estimated position vectors are plotted in Fig. 7.5, which shows a bounded error of less than 2 meters in every dimension for both filters. The estimated gyro bias vectors are nearly identical to reference bias vector and hence we do not plot them here. From Fig. 7.4 and Fig. 7.5, we see

comparable performance of both filters and in some instants we have nearly identical behavior though both filters have different approaches. One explanation for this similarity is that the nonlinearity in the DCM is largely reduced by avoiding the sinusoidal terms.

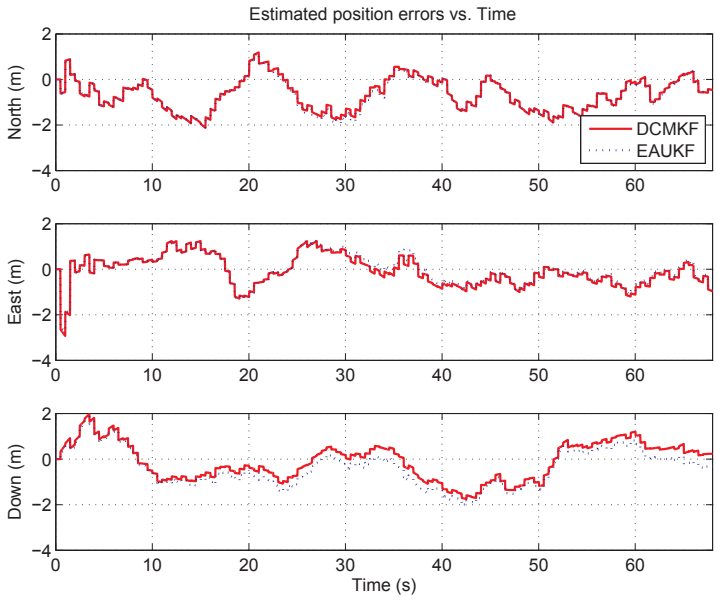

Fig. 7.5 Estimated position errors

7.4.3 Computational Burden of Both Filters

The analytical approach to evaluate the computational burden is performed by counting the number of multiplications and additions used in the filter implementation. However, in our case we have two different models with different mathematical functions. The Euler angles based model contains sinusoidal terms while DCM model has no such terms and this complicates the analytical approach. One solution for a rough comparison is to use Matlab timing function which shows that DCMKF requires 4.61 seconds while the EAUKF filter requires 14.84 seconds. Though the dimension of the DCMKF state vector is larger than that of the EAUKF, the processing time of the DCMKF is much less than that of the EAUKF. This feature of the DCMKF makes it suitable for real-time applications.

7.4.4 Results for Improper Initialization

In this part, we initialized both filters with inaccurate values of the bias parameters to investigate the filters' capability of converging to the true values. Clearly, we will not have a smooth behavior as we would have for the properly initialized filters as shown before. However, after both filters converge, they tend to have smooth behavior. Again, we plot the estimated Euler angles errors and the estimated

position errors. We see relatively large errors for the estimated Euler angles at the beginning and during the convergence as shown in Fig. 7.6 and after the filter converges the errors become much smaller.

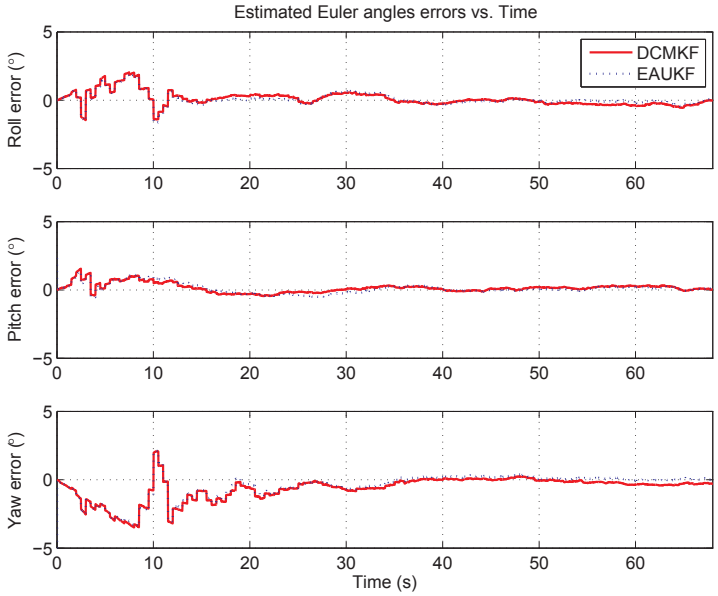

Fig. 7.6 Estimated Euler angles errors for improper initialization

The estimated position errors are also limited and tend to be lower after the filters converge as shown in Fig. 7.7.

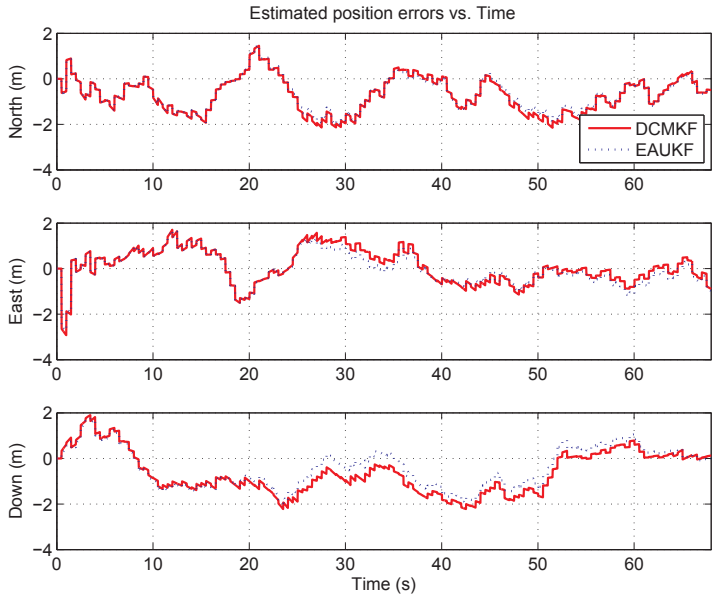

Fig. 7.7 Estimated position errors for improper initialization

The true gyro bias vector is $[1000\ 500\ -1500]^{T}$ (°/h) and the filters were initialized with $[0\ 0\ 0]^{T}$ (°/h) which is far from the true vector value. Both filters converge to the true gyro bias vector in short time for the three components as it can be seen from Fig. 7.8. Again, we see comparable performance in both filters for the improperly initialized case.

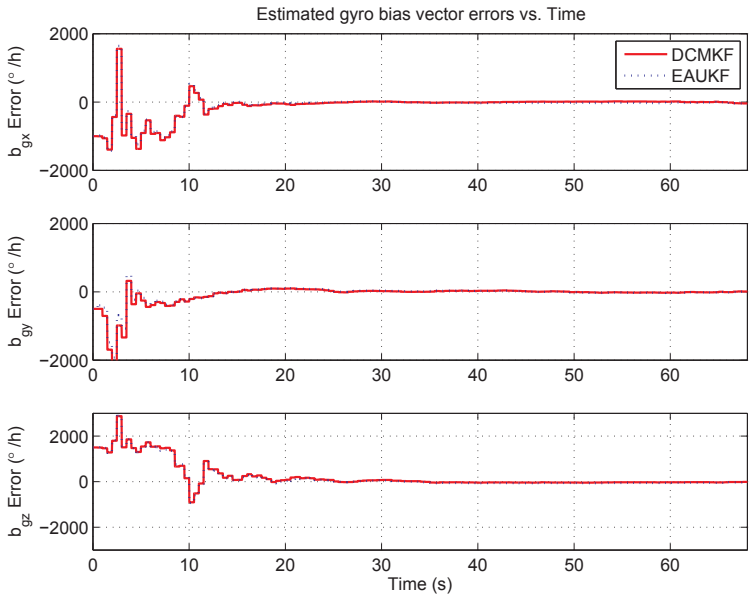

Fig. 7.8 Estimated gyro bias vector errors for improper initialization

7.5 Experimental Results Using Car Collected Data

7.5.1 Route Profile and Sensors' Specifications

The goal of this part is to test the applicability of the DCMKF algorithm with different categories of inertial sensors. We investigate its navigation performance using experimental data collected during car navigation in the city of Siegen, NRW, Germany. We used two different IMUs: the first IMU is the LandmarkTM20 eXT MEMS-based IMU and the second one is Xsens MTi. The IMUs and Ublox GPS antennas are mounted on the car roof away from each other to avoid interference to the IMUs' magnetometers as shown in Fig. 7.9. The synchronized data from IMUs and GPS are recorded using a digital signal processing (DSP) based platform. We refer the reader to [77] for details of the complete hardware description and the adopted data synchronization solution. The specifications of both IMUs based on manufacturer datasheet are given in Table 7.2. We select a total of 160000 points of sensors'

measurements from the collected 30 minutes experimental data at 0.01 s sampling time. The GPS is updated at 1 Hz rate.

Table 7.2 Numerical values of specifications and parameters of the IMUs

Parameter (unit)	**Landmark**	**Xsens**
Accelerometer noise $(m/s^2/\sqrt{Hz})$	0.0007	0.002
Accelerometer bias (m/s^2)	In-run stability = 0.005 Over Temperature < 0.03	0.02
Gyro noise $(°/s/\sqrt{Hz})$	0.035	0.1
Gyro bias $(°/h)$	In-run stability = 30 Over Temperature < 360	18000
Operating Temperature (°C)	-40 …+85	-40 …+85

For the XSENS IMU, the bias stability is temperature compensated and it represents the deviation over operating temperature range.

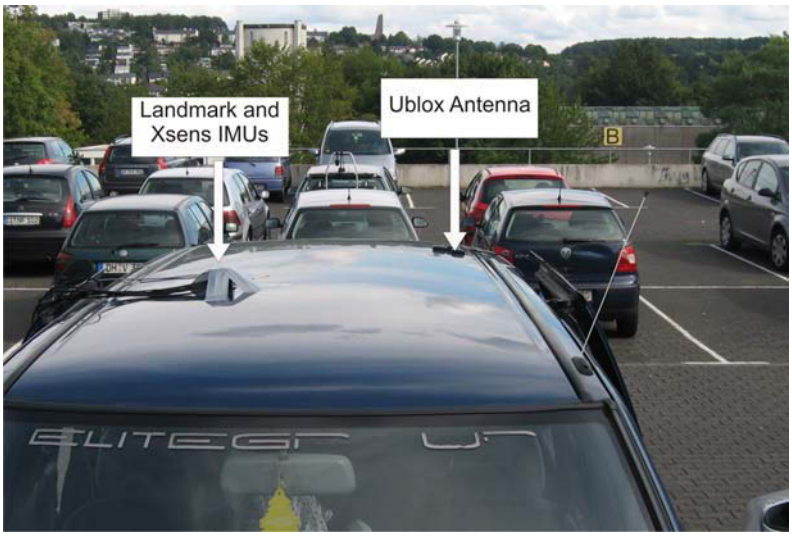

Fig. 7.9 Mounted IMUs and GPS antenna on car roof

The 3D Positional dilution of precision (PDOP) and number of observed satellites during the experiment are plotted in Fig. 7.10 which shows two short-time periods of GPS outage due to passing through a tunnel two times.

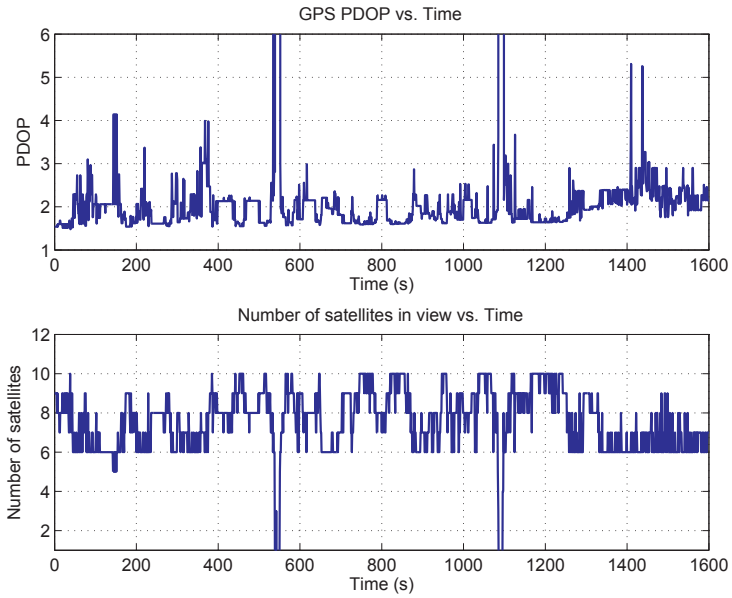

Fig. 7.10 PDOP of GPS solution and number of satellites in view

Plots of the outputs of gyro and accelerometer triads for both IMUs are shown in Fig. 7.11 and Fig. 7.12 respectively.

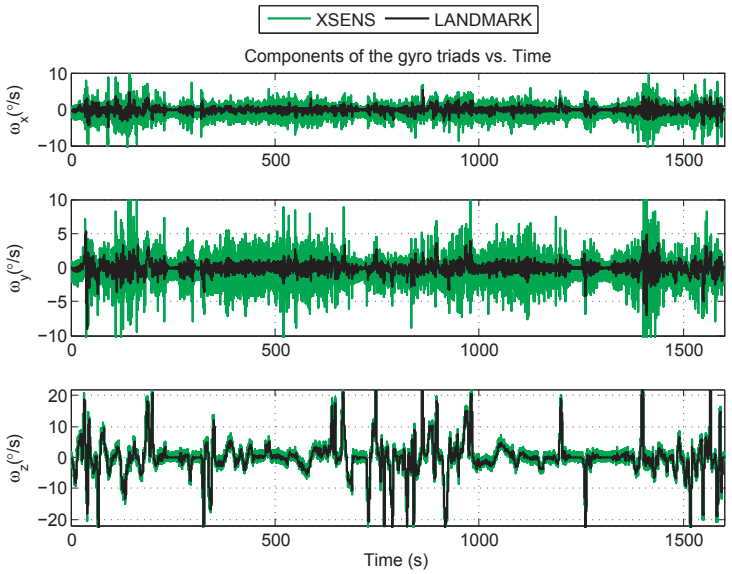

Fig. 7.11 Angular velocity profile measured by the gyro triads

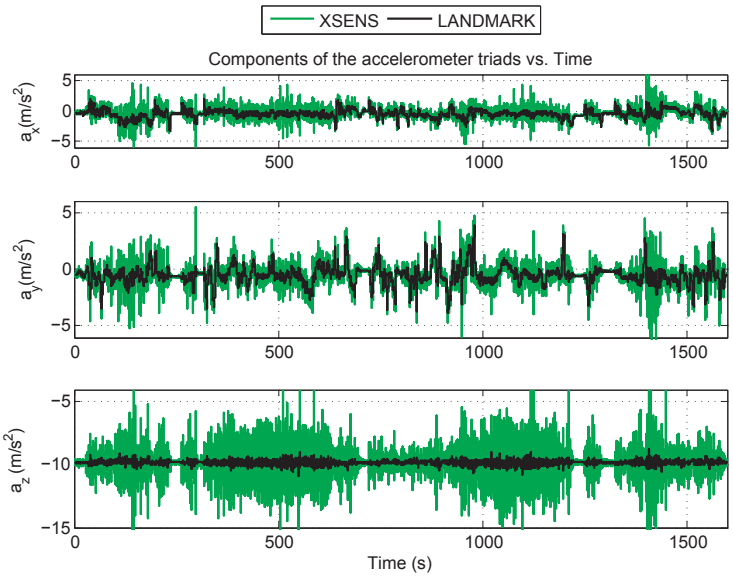

Fig. 7.12 Proper acceleration profile measured by the accelerometer triads

The inertial data of the landmark IMU is less noisy than that of the Xsens IMU. The car remained stationary at the beginning of the experiment to have accurate reference of the initial conditions and the gyro bias vector. Both gyro triads are not sensitive to Earth rotation. Within the route, the car experienced still moments which can be used to infer the gyro bias vector and to correct for tilt angles using the accelerometer triad measurements.

7.5.2 Integration Results and Analysis

We do not have a true reference so we show the results of both IMUs for comparison purpose. In this part, we initialized the filter with accurate values of the DCM and the gyro bias parameters for both IMUs. The initial gyro bias vector was found by averaging the gyro triad measurements when the car was at reset. The position and velocity vectors were initialized with the available measurements from the GPS. In Fig. 7.13, we plot the estimated Euler angles for both IMUs. It should be noted that we used the accelerometer triad to update the tilt angles of the DCM when the car experiences static moments for the Xsens IMU as described before. The estimated Euler angles in both IMUs are in agreement with each other. Better performance can be achieved using a tightly coupled filter.

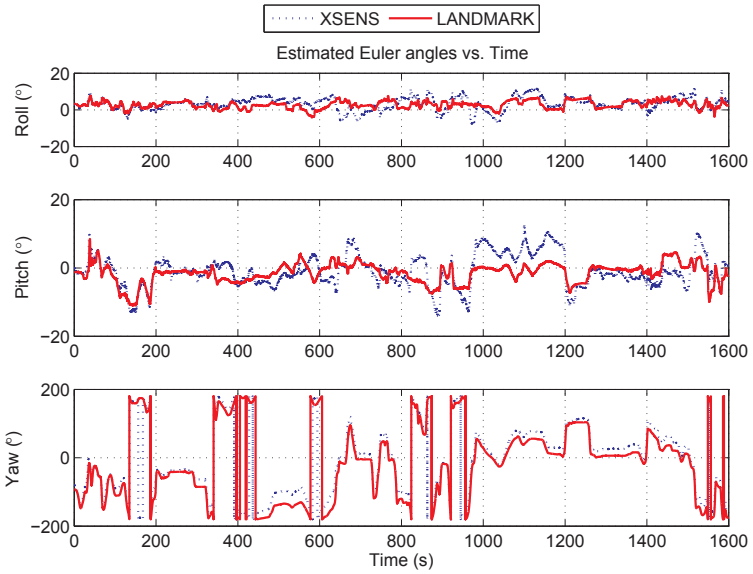

Fig. 7.13 Estimated Euler angles

In Fig. 7.14, we plot the estimated gyro bias vectors for both IMUs. Since we do not have exact references for the gyro bias vectors, we use the extracted values from the moments while the car is static as a reference. The filter is able to track the bias variation of the gyros of both IMUs as the estimated values are compatible with those recorded at the end of the experiment when the car stopped.

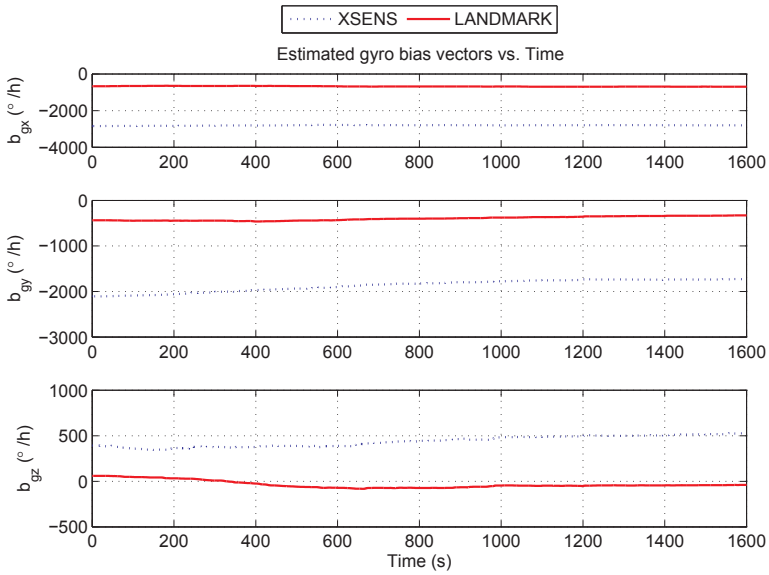

Fig. 7.14 Estimated gyro bias vectors

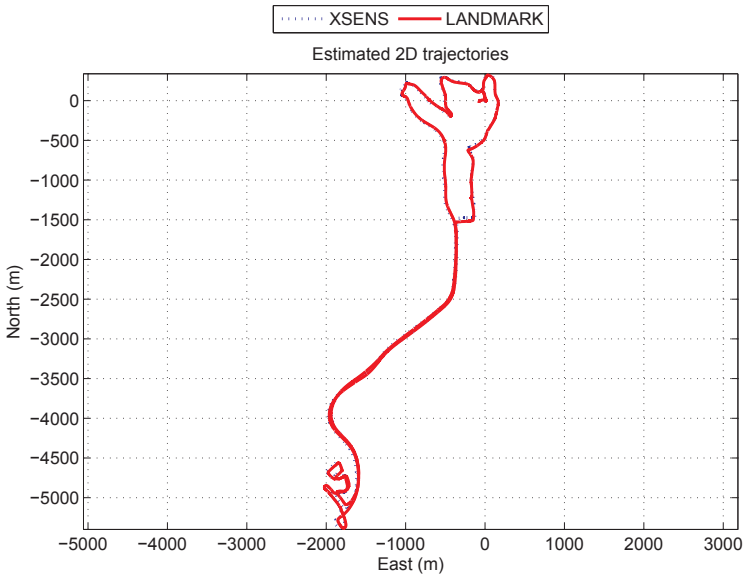

Fig. 7.15 Estimated trajectories

In Fig. 7.15, we plot the estimated 2D trajectories for both IMUs. We see that the estimated trajectories are following very close track. Moreover, the plot shows that the filter is capable of filling short-time gaps of GPS outages without experiencing divergence.

7.6 Special Forms of DCM Based GPS/INS Integration

The kinematics or dynamics of many moving vehicles can be modeled. Most of the current GPS/INS integration approaches do not consider the available information from dynamic models in the integration algorithm. Moreover, modernized GPS and the new European positioning system Galileo promise a better positioning accuracy. This presents new opportunities extending the use of dynamic models in GNSS and inertial sensors integration. Performance improvement can be increased by modeling of the dynamics if the model describes the dynamics sufficiently. This integration approach is based on the ground alignment method for attitude and heading determination. Attitude accuracy is an important issue for many applications including synthetic aperture RADAR (SAR) [78]. Most of the low-cost commercial MEMS based IMUs provide attitude solution based on ground alignment method. For static scenarios the low-cost tri-axial accelerometers operate effectively in determining tilt angles. Ground alignment relies on measuring the gravity vector in the body frame and on the knowledge of the gravity vector in the local navigation frame. As the body accelerates, the ground alignment method becomes improper because tri-axial accelerometers measure not only the gravity

vector but also the acceleration of the body. This promotes the idea that, if the acceleration of the body can be computed in the local navigation frame then the same procedure can be applied for the dynamic case. Proper dynamic models are important for an improved GPS/INS integration. A dynamic model is used to update the process part of position, velocity, and acceleration to get an accurate estimate of the acceleration expressed in the local navigation frame while the rotation vector is used to update the elements of the DCM in the state vector. The complexity of the dynamic model is chosen to fit the trajectory profile. The aid of the GPS for the dynamic model might be enough to have a solution for the position estimation for some applications. Using a simulation example, this approach has shown to be sufficient to keep filtered navigation position solution limited within one standard deviation of GPS measurements and the attitude solution limited by less than one degree standard deviation error when using low-cost inertial sensors. More results and details about this special case can be found in [79].

7.7 Summary

We presented a novel GPS/INS integration method based on the DCM attitude representation model. The filter is able to detect the gyro bias vector and follow its variation and hence it fits low-cost sensors as well as high grade sensor. Simulations were conducted to compare its performance with the performance of Euler angles based UKF. The DCMKF is showing comparable performance of the EAUKF for position and attitude estimation with much less computational time. Experimental validation of the filter is conducted using different categories of IMUs. Further research can be conducted to reduce the number of the DCM elements to be estimated and to find computationally efficient DCM orthogonalization approaches for improving the filter performance. The DCM based integration approach can be extended to sophisticated approaches of GPS/INS integration.

Chapter 8
Conclusion

8.1 Summary

In this dissertation we developed different novel approaches for improving the performance of inertial sensor systems and their fusion with external sensors. In the inertial sensors side, we focused on the use of distributed accelerometers for inferring the angular motion from the angular information contained in their measurements. We developed different fusion approaches for benefiting from the AIV to form a GF-IMU or to aid the GF-IMU by conventional gyros. We presented two novel solutions for estimating the angular motion from a multiple distributed tri-axial accelerometers measurements in a GF-IMU. The integration approach is performed using an EKF. Also, we presented another approach for AME utilizing dynamic models in 3D which is capable of estimating bias parameters in a GF-IMU. Also, we derived nonlinear equality constraints and presented a filter approach to benefit from the constraints in improving estimation performance. We also showed the benefits of using the hybrid IMU over the GF-IMU.

In the integrated navigation side, we presented different approaches to implement the GPS/INS integration filters and the AHRS algorithms based on DCM attitude representation. The attitude update of the DCM is performed using angle rotation vector. The experimental real-time implementations validated the efficiency of the algorithms and were in harmony with simulations. They also revealed their importance to the inertial sensors market.

The main contributions of this work, with emphasis on their novelty and where they have been published, are listed as follows:

- The development of a GF-IMU using a configuration of twelve fixed accelerometers and adopting a calibration procedure for the GF-IMU. This configuration benefits from the AIV with a simple calibration procedure. This contribution has been published in [80].
- Deriving two Kalman filters models for AME using the AIV. The first model is a direct model based on Euler integration. The second model is based on dynamic models and it is capable of estimating the bias vector in the AIV due to accelerometers' bias vector. This is a novel solution to have a bias-free IMU. Those contributions have been published in [36, 80].

- Using distributed accelerometers to aid conventional gyros to avoid the drawbacks of both types of sensors and to get the best of both. This contribution has been published in [41].
- The development of a GF-IMU using fixed and rotating accelerometers configurations and applying this principle to construct a north finding system.
- Developing a novel DCM based GPS/INS integration algorithm and a novel DCM based attitude estimation algorithm. Those contributions have been published in [81, 82].

8.2 Conclusion

After working and conducting research on improving inertial sensor systems and information fusion for long time we list the following concluding remarks:

1. Proper fusion of the AIV in the GF-IMU can solve the sign indeterminacy problem for dynamic motion as shown by experimental results. The more accurate sensors we use the higher chances for avoiding sign indeterminacy problems.
2. Euler integration based EKF model fits all scenarios of motion and has minimum computational load; however, largely biased accelerometers downgrade its performance.
3. The CAA dynamic model employed in GF-IMU works well for free-hand motion; however, it does not fit sharp rotations.
4. The hybrid IMU has many advantages over classical IMU and GF-IMU such as possessing increased range, bias-free and smoother convergence.
5. The rotating accelerometers are difficult to build mechanically; however, there is a special case for north finding system under static scenario. In this case, rotating accelerometers show efficient use without having vibrations problems because of digital filtering.
6. DCM based AHRS algorithm is either linear or pseudolinear and the computational load can be reduced by reducing the number of DCM elements to be estimated.
7. DCM based GPS/INS can be realized and used effectively with off-the-shelf low-cost sensors and processing boards.
8. Dynamic models can be deployed in DCM based GPS/INS integration for improving integration performance if the model describes the dynamics sufficiently.

8.3 Suggestions for Future Work

We managed to tackle many problems within this dissertation; however, there are many future steps which can be added in this field.

8.3.1 Estimation of Bias Parameters in a GF-IMU

We developed an algorithm capable of estimating the bias vector in the AIV. Further research can be done to estimate the remaining bias parameters in the accelerometers. We used dynamic models and specifically the CAA model. Complicated model with that combines the linear acceleration with angular motion can be investigated for finding the complete bias. For constrained angular motion estimation we used the SCKF; however, other less complex approaches should be investigated since the nonlinear constrained Kalman filtering topic itself is an open research topic.

8.3.2 Exploring More Complex Configurations

We focused on twelve distributed accelerometers configuration that requires distribution in distance. It is known that even small distribution distance might be a problem in certain applications. The relation between using more complex accelerometers configurations and reducing the distribution distance can be investigated to a chive smaller size system.

8.3.3 Improving the Acceleration Knowledge

The focus use of distributed accelerometers in this dissertation was to improve the angular rate knowledge. Redundancy of distributed accelerometers is used to improve the accelerometers knowledge by back projection of acceleration to the central position. More complex and optimum approaches can be investigated in the future to improve both angular rate and acceleration. One approach can be a Kalman filter that combines linear acceleration with angular velocity in the same filter.

8.3.4 Improving DCM Based Attitude Estimation and GPS/INS Integration

As a result of redundancy in the DCM elements we have orthogonality constraints which were nonlinear. Handling of the nonlinear constraints of the DCM in a computationally efficient approach could be a future research topic. Another direction for future work is to develop dynamic models that are suitable to be deployed for GPS/INS integration for different scenarios of motion.

Appendix A
Derivatives of Matrices and Vectors

A.1 The Gradient of a Scalar Function

Let $f(\underline{x})$ be a real valued scalar function of a *n*-vector $\underline{x}$, the gradient of $f(\underline{x})$ with respect to $\underline{x}$ is defined as

$$\nabla = \left[\frac{\partial f(\underline{x})}{\partial x_1} \quad \frac{\partial f(\underline{x})}{\partial x_2} \quad \cdots \quad \frac{\partial f(\underline{x})}{\partial x_n} \right]. \tag{A.1}$$

The derivative of $f(\underline{x})$ is defined as a row vector with dimension $1 \times n$.

A.2 The Partial Derivative of a Vector Function

Let $\underline{f}(\underline{x})$ be a *m*-dimensional vector-valued function of a *n*-vector *x*, the gradient of $\underline{f}(\underline{x})$ with respect to $\underline{x}$ is defined as

$$F = \frac{\partial \underline{f}(\underline{x})}{\partial \underline{x}} = \begin{bmatrix} \frac{\partial f_1(\underline{x})}{\partial x_1} & \frac{\partial f_1(\underline{x})}{\partial x_2} & \cdots & \frac{\partial f_1(\underline{x})}{\partial x_n} \\ \frac{\partial f_2(\underline{x})}{\partial x_1} & \frac{\partial f_2(\underline{x})}{\partial x_2} & \cdots & \frac{\partial f_2(\underline{x})}{\partial x_n} \\ . & . & \cdots & . \\ \frac{\partial f_m(\underline{x})}{\partial x_1} & \frac{\partial f_m(\underline{x})}{\partial x_2} & \cdots & \frac{\partial f_m(\underline{x})}{\partial x_n} \end{bmatrix}. \tag{A.2}$$

A.3 The Partial Derivative of Vector Dot Products

Suppose $\underline{x}$ and $\underline{y}$ are n-element column vectors. The scalar product is defined as

$$\underline{x}^T \underline{y} = x_1 y_1 + ... + x_n y_n . \tag{A.3}$$

The partial derivative is defined as

$$\begin{aligned} \frac{\partial \underline{x}^T \underline{y}}{\partial \underline{x}} &= \left[\frac{\partial \underline{x}^T \underline{y}}{\partial x_1} \quad \frac{\partial \underline{x}^T \underline{y}}{\partial x_2} \quad \cdots \quad \frac{\partial \underline{x}^T \underline{y}}{\partial x_n} \right] \\ &= \begin{bmatrix} y_1 & y_2 & \cdots & y_n \end{bmatrix} \\ &= \underline{y}^T \end{aligned} . \tag{A.4}$$

Likewise,

$$\frac{\partial \underline{x}^T \underline{y}}{\partial \underline{y}} = \underline{x}^T . \tag{A.5}$$

A.4 The Lie Derivatives

We compute *L*, which denotes the set of all finite linear combinations of Lie derivatives of the measurement vector with respect to $\underline{f}(\underline{x})$ for various values of constant input. For the *i*th row scalar measurement h_i of the measurement vector, the Lie derivative of a scalar measurement is defined as

$$L_f(h_i) = \frac{\partial h_i}{\partial \underline{x}} \cdot \underline{f}(\underline{x}) . \tag{A.6}$$

The zeroth-order Lie derivative of the measurement is the measurement itself, i.e.,

$$L_f^0(h_i) = h_i . \tag{A.7}$$

Higher order Lie derivatives are computed as

$$L_f^k(h_i) = h_i^k . \tag{A.8}$$

Appendix B
Special Matrices

B.1 Symmetric Matrix

A symmetric matrix has the property that the transpose of the matrix equal the matrix itself, i.e.,

$$A^T = A . \tag{B.1}$$

B.2 Diagonal Matrix

A matrix is diagonal if

$$a(i,j) = 0 \quad \text{if } i \neq j \ \forall (i,j) \in \{1,2,3,...,n\} . \tag{B.2}$$

Identity matrix is a special case of the diagonal matrix. The identity matrix , I, has

$$a(i,j) = \begin{cases} 0 & \text{if } i \neq j \\ 1 & \text{if } i = j \end{cases} \ \forall (i,j) \in \{1,2,3,...,n\} . \tag{B.3}$$

B.3 Skew Symmetric Matrix and Cross Product Properties

The cross product operation converts a vector to a squared matrix with skew symmetric form

$$\underline{a} = \begin{bmatrix} a_x \\ a_y \\ a_z \end{bmatrix} \quad , \quad \underline{a}\times = \begin{bmatrix} 0 & -a_z & a_y \\ a_z & 0 & -a_x \\ -a_y & a_x & 0 \end{bmatrix} . \tag{B.4}$$

A skew symmetric has the property that the transpose of the matrix equal its negative, i.e.,

$$A^T = -A . \tag{B.5}$$

The following identities are true for cross product operations

$$\begin{aligned} &A = \underline{a}\times \\ &B = \underline{b}\times \\ &C = \underline{c}\times \\ &a\times b = -b\times a \\ &BA\underline{c} + (Ab)\times \underline{c} = ABc \\ &BA\underline{c} - (Ba)\times \underline{c} = ABc \\ &(Ab)\times = AB - BA \\ &(a\times b)\times = AB - BA \end{aligned} . \tag{B.6}$$

B.4 Orthogonal Matrices

The orthogonal matrices are those square matrices which have columns and rows with unity magnitude. This implies

$$A^T A = I \tag{B.7}$$

where I is the identity matrix. Equivalently, a matrix is orthogonal if its transpose is equal to its inverse

$$A^{-1} = A^T . \tag{B.8}$$

References

[1] R. Hanson, "Optimal gyro-free IMU geometry," in *Proceedings of AIAA Guidance, Navigation, and Control Conference and Exhibit* San Francisco, CA, USA, 2005.

[2] S. Park, C.-W. Tan, and J. Park, "A scheme for improving the performance of a gyroscope-free inertial measurement unit," *Sensors and Actuators A: Physical,* vol. 121, pp. 410-420, 2005.

[3] J. H. Chen, S. C. Lee, and D. B. DeBra, "Gyroscope free strapdown inertial measurement unit by six linear accelerometers," *Journal of Guidance Control and Dynamics,* vol. 17, p. 286, 1994.

[4] Q. Wang, M. Ding, and P. Zhao, "A new scheme of non-gyro inertial measurement unit for estimating angular velocity," in *Proceedings of the 29th Annual Conference of the IEEE Industrial Electronics Society (IECON '03)*, 2003, pp. 1564-1567.

[5] S. J. Merhav, "A nongyroscopic inertial measurement unit," *Journal of Guidance, Control, and Dynamics* vol. vol.5, pp. 227-235, 1982.

[6] K. Parsa, T. A. Lasky, and B. Ravani, "Design and implementation of a mechatronic, all-accelerometer inertial measurement unit," *IEEE/ASME Transactions on Mechatronics,* vol. 12, pp. 640-650, 2007.

[7] A. Wei Tech, P. K. Khosla, and C. N. Riviere, "Kalman filtering for real-time orientation tracking of handheld microsurgical instrument," in *Proceedings of the IEEE/RSJ International Conference on Intelligent Robots and Systems, IROS*, 2004, pp. 2574-2580 vol.3.

[8] A. H. Zorn, "A merging of system technologies: all-accelerometer inertial navigation and gravity gradiometry," in *Proceedings of the IEEE Position Location and Navigation Symposium (PLANS 2002)*, 2002, pp. 66-73.

[9] M. Costello and C. Webb, "Angular rate estimation using fixed and vibrating triaxial acceleration measurements," *Journal of Spacecraft and Rockets,* vol. 42, pp. 1133-1137, 2005.

[10] G. Clark, "Angular and linear velocity estimation for a re-entry vehicle using six distributed accelerometers: theory, simulation and feasibility," UCRL-ID-153253; TRN: US200321, 2003, p. 69.

[11] T. Chin-Woo and P. Sungsu, "Design of accelerometer-based inertial navigation systems," *IEEE Transactions on Instrumentation and Measurement,* vol. 54, pp. 2520-2530, 2005.

[12] R. Hanson, "Using multiple MEMS IMUs to form a distributed inertial measurement unit," Master Thesis, Ft. Belvoir: Air Force Institute of Technology, Wright-Patterson Air Force Base, School of Engineering and Management, 2005.

[13] K. S. Mostov, A. A. Soloviev, and T. K. J. Koo, "Initial attitude determination and correction of gyro-free INS angular orientation on the basis of GPS linear navigation parameters," in *Proceedings of the IEEE Conference on Intelligent Transportation System (ITSC '97)*, 1997, pp. 1034-1039.

[14] P. Ying Kun and M. F. Golnaraghi, "A vector-based gyro-free inertial navigation system by integrating existing accelerometer network in a passenger vehicle," in *Proceedings of the IEEE Position Location and Navigation Symposium 2004 (PLANS 2004)*, 2004, pp. 234-242.

[15] R. Chow, "Evaluating inertial measurement units," in *Test and measurement world*. vol. 31, 2011, pp. 34-38.

[16] S. A. Hewitson , J. Wang, and A. H. W. Kearsley, "Performance evaluation of inertial navigation systems for surveying applications," in *Proceeding of the 6th International Symposium on Satellite Navigation Technology Including Mobile Positioning & Location Services* Melbourne, Australia, 2003.

[17] D. Gebre-Egziabher, "Design and performance analysis of a low-cost aided dead reckoning navigator," Stanford University, PhD Dissertation, 2004.
[18] S. Knedlik, "Introduction to satellite navigation, inertial navigation and GNSS/INS integration," habilitation thesis, 2011.
[19] L. Levy and A. Pue, "Integration of GPS with Inertial Navigation Systems," ION GPS-2001 Tutorial, Salt Lake City10 September 2001.
[20] K. P. Schwarz and N. El-Sheimy, "Future positioning and navigation technologies," Department of Geomatics Engineering, The University of Calgary, Calgary, Canada.1999.
[21] http://www51.honeywell.com/aero/common/documents/myaerospacecatalog-documents/Missiles-Munitions/HG1700_Inertial_Measurement_Unit.pdf.
[22] D. Roetenberg, "Inertial and magnetic sensing of human motion," S.l.: s.n.], 2006.
[23] H. Weinberg, "MEMS Sensors Are Driving the Automotive Industry," *SENSORS - PETERBOROUGH-,* vol. 19, pp. 36-41, 2002.
[24] H. Weinberg, "MEMS Inertial Sensors Move Beyond Airbags," in *WARD'S AUTO ELECTRONICS*, 2004, pp. 44-48.
[25] D. H. Titterton and J. L. Weston, "Strapdown inertial navigation technology," 2nd ed London, UK: The American Institute of Aeronautics and Astronautics and The Institution of Electrical Engineers, 2004.
[26] J. Bernstein, "An Overview of MEMS Inertial Sensing Technology," *SENSORS - PETERBOROUGH-,* vol. 20, pp. 14-21, 2003.
[27] S. Nassar, "Improving the inertial navigation system (INS) error model for INS and INS/DGPS applications," The University of Calgary, PhD Dissertation,2003.
[28] R. M. Rogers, *Applied mathematics in integrated navigation systems*. Reston, VA: American Institute of Aeronautics and Astronautics, 2003.
[29] T. Chin-Woo and P. Sungsu, "Design of accelerometer-based inertial navigation systems," *Instrumentation and Measurement, IEEE Transactions on,* vol. 54, pp. 2520-2530, 2005.
[30] B. Zappa, G. Legnani, A. J. van den Bogert, and R. Adamini, "On the number and placement of accelerometers for angular velocity and acceleration determination," *Journal of Dynamic Systems, Measurement, and Control,* vol. 123, pp. 552-554, 2001.
[31] C. Jekeli, *Inertial navigation systems with geodetic applications*. Berlin; New York: Walter de Gruyter, 2001.
[32] G. Clark, "Angular and linear velocity estimation for a re-entry vehicle using six distributed accelerometers: theory, simulation and feasibility," Lawrence Livermore National Lab., CA, USA, Report Number: UCRL-ID-153253, 2003.
[33] M. C. Algrain and J. Saniie, "Estimation of 3D angular motion using gyroscopes and linear accelerometers," *IEEE Transactions on Aerospace and Electronic Systems,* vol. 27, pp. 910-920, 1991.
[34] Z. F. Syed, P. Aggarwal, C. Goodall, X. Niu, and N. El-Sheimy, "A new multi-position calibration method for MEMS inertial navigation systems," *Measurement Science & Technology.,* vol. 18, pp. 1897-1907, 2007.
[35] T. Bragge, M. Hakkarainen, M. Tarvainen, T. Liikavainio, J. Arokoski, and P. Karjalainen, "Calibration of triaxial accelerometer by determining sensitivity matrix and offsets simultaneously," in *Proceedings of the 1st Joint ESMAC - GCMAS Meeting* Amsterdam, the Netherlands, 2006.
[36] E. Edwan, S. Knedlik, M. Zhang, and O. Loffeld, "Investigation of dynamic models for angular motion estimation in a Gyro-Free IMU," in *Proceedings of the 16th Saint Petersburg International Conference on Integrated Navigation Systems*, St. Petersburg; Russian Federation, 2009.
[37] D. Simon, *Optimal state estimation Kalman, H [infinity] and nonlinear approaches*. Hoboken, N.J.: Wiley-Interscience, 2006.

[38] P. Cardou and J. Angeles, "Estimating the angular velocity of a rigid body moving in the plane from tangential and centripetal acceleration measurements," *Multibody System Dynamics,* vol. 19, pp. 383-406, 2008.
[39] http://www.analog.com.
[40] M. Costello and T. Jitpraphai, "Determining angular velocity and angular acceleration of projectiles using triaxial acceleration measurements," *Journal of spacecraft and rockets* vol. 39, pp. 73-80, 2002.
[41] E. Edwan, S. Knedlik, and O. Loffeld, "An extended Kalman filter for improving angular motion knowledge in a multiple distributed IMU set," in *Proceedings of Symposium Gyro Technology*, Karlsruhe, Germany, 2008.
[42] J. Geen and D. Krakauer, "New iMEMS Angular-Rate-Sensing Gyroscope," in *Analog Dialogue* vol. 37, 2003.
[43] T. Williams, A. Pahadia, M. Petovello, and G. Lachapelle, "Using an Accelerometer Configuration to Improve the Performance of a MEMS IMU: Feasibility Study with a Pedestrian Navigation Application," in *Proceedings of the 22nd International Technical Meeting of The Satellite Division of the Institute of Navigation (ION GNSS 2009)*, Savannah, GA 2009, pp. 3049 - 3063.
[44] S. Guofu and G. Qitai, "Accelerometer based north finding system," in *Position Location and Navigation Symposium, IEEE 2000*, 2000, pp. 399-403.
[45] I. Y. Bar-Itzhack, "New Inertial Azimuth Finder Apparatus," *Journal of Guidance, Control, and Dynamics* vol. 24, pp. 206-213, 2001.
[46] T. Pöthig and G. Lappus, "Non-Gyroscopic North Finding System," in *Proceedings of Symposium Gyro Technology*, Karlsruhe, Germany, 2008.
[47] E. Edwan, J. Zhang, J. Zhou, and O. Loffeld, "Reduced DCM Based Attitude Estimation Using Low-cost IMU and Magnetometer Triad," in *Proceedings of the 8th Workshop on Positioning, Navigation and Communication (WPNC'11)* Dresden, Germany, 2011, pp. 1-6.
[48] X. Rong Li and V. P. Jilkov, "Survey of maneuvering target tracking. Part I. Dynamic models," *Aerospace and Electronic Systems, IEEE Transactions on,* vol. 39, pp. 1333-1364, 2003.
[49] Y. Oshman and F. L. Markley, "Spacecraft attitude/rate estimation using vector-aided GPS observations," *IEEE Transactions on Aerospace and Electronic Systems,* vol. 35, pp. 1019-1032, 1999.
[50] R. A. Singer and K. W. Behnke, "Real-Time Tracking Filter Evaluation and Selection for Tactical Applications," *Aerospace and Electronic Systems, IEEE Transactions on,* vol. AES-7, pp. 100-110, 1971.
[51] A. Isidori, *Nonlinear Control Systems*. Berlin: Springer, 1995.
[52] X. Rong Li and V. P. Jilkov, "Survey of maneuvering target tracking. Part I. Dynamic models," *IEEE Transactions on Aerospace and Electronic Systems,* vol. 39, pp. 1333-1364, 2003.
[53] A. T. Alouani and W. D. Blair, "Use of a kinematic constraint in tracking constant speed, maneuvering targets," *IEEE Transactions on Automatic Control,* vol. 38, pp. 1107-1111, 1993.
[54] D. Simon and C. Tien Li, "Kalman filtering with state equality constraints," *IEEE Transactions on Aerospace and Electronic Systems,* vol. 38, pp. 128-136, 2002.
[55] Y. Chun and E. Blasch, "Kalman Filtering with Nonlinear State Constraints," *IEEE Transactions on Aerospace and Electronic Systems,* vol. 45, pp. 70-84, 2009.
[56] S. J. Julier and J. J. LaViola, "On Kalman filtering with nonlinear equality constraints," *IEEE Transactions on Signal Processing,* vol. 55, pp. 2774-2784, 2007.
[57] J. De Geeter, H. Van Brussel, J. De Schutter, and M. Decreton, "A smoothly constrained Kalman filter," *IEEE Transactions on Pattern Analysis and Machine Intelligence,* vol. 19, pp. 1171-1177, 1997.

[58] J. L. Marins, Y. Xiaoping, E. R. Bachmann, R. B. McGhee, and M. J. Zyda, "An extended Kalman filter for quaternion-based orientation estimation using MARG sensors," in *Proceedings of the IEEE/RSJ International Conference on Intelligent Robots and Systems*, 2001, pp. 2003-2011.

[59] A. M. Sabatini, "Quaternion-based extended Kalman filter for determining orientation by inertial and magnetic sensing," *IEEE Transactions on Biomedical Engineering,* vol. 53, pp. 1346-1356, 2006.

[60] N. H. Q. Phuong, H.-J. Kang, Y.-S. Suh, and Y.-S. Ro, "A DCM Based Orientation Estimation Algorithm with an Inertial Measurement Unit and a Magnetic Compass," *Journal of Universal Computer Science,* vol. 15, pp. 859-876, 2009.

[61] D. Choukroun, "Novel methods for attitude determination using vector observations," The Technion, PhD Dissertation, 2003.

[62] L. Cheng, Z. Zhaoying, and F. Xu, "Attitude Determination for MAVs Using a Kalman Filter," *Tsinghua Science and Technology,* vol. 13, pp. 593-597, 2008.

[63] L. Wang, S. Xiong, Z. Zhou, Q. Wei, and J. Lan, "Constrained Filtering Method for MAV Attitude Determination," in *Proceedings of the IEEE Instrumentation and Measurement Technology Conference (IMTC 2005)* Ottawa, Canada, 2005, pp. 1480-1483.

[64] P. G. Savage, "Strapdown system computational elements," in *NATO RTO educational notes, SET-064*, Neuilly-sur-Seine Cedex, France, 2004.

[65] J. E. Bortz, "A new mathematical formulation for strapdown inertial navigation," *IEEE Transactions on Aerospace and Electronic Systems,* vol. AES-7, pp. 61-66, 1971.

[66] H. Rehbinder and H. Xiaoming, "Drift-free attitude estimation for accelerated rigid bodies," in *Proceedings of 2001 IEEE International Conference on Robotics and Automation (ICRA2001)*, 2001, pp. 4244-4249.

[67] E. Foxlin, "Inertial head-tracker sensor fusion by a complementary separate-bias Kalman filter," in *Proceedings of the IEEE Virtual Reality Annual International Symposium*, 1996, pp. 185-194, 267.

[68] J. S. Suh, S. Y. Park, H. J. Kang, and Y. S. Ro, "Attitude Estimation Adaptively Compensating External Acceleration," *JSME International Journal, Series C,* vol. 49, 2006.

[69] http://www.ngdc.noaa.gov/geomag/geomag.shtml.

[70] D. Roetenberg, H. J. Luinge, C. T. M. Baten, and M. Peter H. Veltink, "Compensation of Magnetic Disturbances Improves Inertial and Magnetic Sensing of Human Body Segment Orientation," *IEEE Transactions on Neural Systems and Rehabilitation Engineering,* vol. 13, pp. 395-405, 2005.

[71] T. Harada, H. Uchino, T. Mori, and T. Sato, "Portable absolute orientation estimation device with wireless network under accelerated situation," in *Proceedings of the 2004 IEEE International Conference on Robotics and Automation (ICRA '04)*, 2004, pp. 1412-1417.

[72] Q. Ladetto and B. Merminod, "Digital magnetic compass and gyroscope integration for pedestrian navigation " in *Proceedings of the 9th Saint Petersburg International Conference on Integrated Navigation Systems*, St. Petersburg; Russian Fedration, 2002, pp. 111-120.

[73] C. Jagadish and B.-C. Chang, "Diversified redundancy in the measurement of Euler angles using accelerometers and magnetometers," in *Proceedings of the 46th IEEE Conference on Decision and Control*, New Orleans, LA, USA, 2007, pp. 2669 - 2674

[74] D. Simon, "Kalman filtering with state constraints: a survey of linear and nonlinear algorithms," *Control Theory & Applications, IET,* vol. 4, pp. 1303-1318, 2010.

[75] H. Q. P. Nguyen, H. J. Kang, Y. S. Suh, and Y. S. Ro, "INS/GPS Integration System with DCM Based Orientation Measurement," in *Emerging Intelligent Computing Technology and Applications*. vol. 5754: Springer Berlin / Heidelberg, 2009, pp. 856-869.

[76] J. Zhou, S. Knedlik, E. Edwan, and O. Loffeld, "Low-cost INS/GPS with Nonlinear Filtering Methods," in *Proceedings of the13th International Conference on Information Fusion*, Edinburgh, UK, 2010.

[77] J. Zhang, E. Edwan, J. Zhou, and O. Loffeld, "Development and Investigation of Real-time Hybrid Navigation System Using a DCM Based Integration Method," in *ION GNSS 2010*, Portland, Oregon, USA, 2010.

[78] S. Knedlik, E. Edwan, J. Zhou, Z. Dai, P. Ubolkosold, and O. Loffeld, "GPS/INS integration for footprint chasing in bistatic SAR experiments," in *Proceedings of the IEEE Geoscience and Remote Sensing Symposium, IGARSS'08* Boston, USA, 2008.

[79] E. Edwan, S. Knedlik, J. Zhou, and O. Loffeld, "A constrained GPS/INS integration based on rotation angle for attitude update and dynamic models for position update," in *Proceedings of the International Technical Meeting (ITM)* Anaheim, CA: ION, 2009.

[80] E. Edwan, S. Knedlik, and O. Loffeld, "Constrained angular motion estimation in a gyro free IMU," *IEEE Transactions on Aerospace and Electronic Systems* vol. 47, 2011.

[81] E. Edwan, J. Zhou, J. Zhang, and O. Loffeld, "Derivation and Evaluation of a Loosely Coupled DCM Based GPS/INS Integration Method," in *Proceedings of the European Navigation Conference on Global Navigation Satellite Systems (ENC GNSS 2010)* Braunschweig, Germany, 2010.

[82] E. Edwan, J. Zhou, J. Zhang, and O. Loffeld, "A New Loosely Coupled DCM Based GPS/INS Integration Method," *NAVIGATION,* vol. 59, pp. 93-106, Summer 2012.